Next Materials 12 (2026) 102226

Contents lists available at ScienceDirect

Next Materials

journal homepage: www.sciencedirect.com/journal/next-materials

Review article

A comparative review of solid-state cold spray versus fusion-based additive manufacturing of Inconel 718: Microstructure and mechanical performance

Abhinav Anand [a,b,*], Ondřej Kovářík [c], Mario Guagliano [a], Jan Cizek [b,d]

[a] Department of Mechanical Engineering, Politecnico di Milano, Milano, Italy
[b] Institute of Plasma Physics of the Czech Academy of Sciences, Prague, Czechia
[c] Faculty of Nuclear Science and Physical Engineering, Czech Technical University, Prague, Czechia
[d] Faculty of Mechanical Engineering, Czech Technical University, Prague, Czechia

ARTICLE INFO

Keywords:
Cold spray
Metal additive manufacturing
Superalloy
Heat treatment
Fatigue
Microstructure

ABSTRACT

Inconel 718 (IN718) is a nickel-based, precipitation-strengthened superalloy widely used in the aerospace industry due to its high-temperature strength and exceptional creep resistance. Compared to traditional manufacturing, additive manufacturing (AM) offers shorter lead times, fabricates geometrically complex components, enables the consolidation of multiple components into a single integrated part, supports multi-material builds, allows for part customization, and facilitates the repair of high-value IN718 components. Over the past decade, fusion-based AM methods such as laser powder bed fusion, directed energy deposition, and wire-arc additive manufacturing have been widely studied and adopted for industrial applications. Meanwhile, solid-state cold spray AM (CSAM) has emerged as an alternative for IN718, depositing material without melting and thereby reducing fusion-related issues such as oxidation, hot cracking, and elemental segregation. CSAM has enabled high-deposition-rate fabrication of free-standing builds with simple geometries in addition to its established use in coatings and repair. This review provides an in-depth comparison of CSAM and fusion-based AM routes for IN718. It compares the as-built microstructures, their evolution under standard and tailored heat treatments, and the resulting mechanical properties for different AM routes. Fatigue behavior, including high-cycle fatigue strength and room-temperature fatigue crack growth rates, is also covered. Furthermore, the article highlights the limited fatigue data available for CSAM IN718 and the lack of systematic heat treatment studies, which currently restricts the definition of durability and damage-tolerance limits for CSAM repairs and freestanding parts in high-reliability applications such as aerospace.

1. Introduction

1.1. Inconel superalloys

Superalloys are high-temperature alloys developed after World War II for turbo-superchargers and gas-turbine engines [1]. They retain strength, ductility, and resistance to oxidation and corrosion after long exposure above ∼ 650 °C, enabling sustained service under high stress, cyclic loading, and aggressive environments [2]. Classified by base element (nickel, cobalt, or iron), nickel-based superalloy grades dominate due to their superior high-temperature strength. In modern aero-engines, they comprise roughly 40–50% of the mass, concentrated in the hot sections such as turbine blades, vanes, disks, and combustor hardware [3]. Among these superalloys, IN718 is the workhorse grade, balancing high strength, formability, weldability, and cost [4].

IN718 typically comprises 50–55 wt% nickel (Ni), 17–21 wt% chromium (Cr), 4.7–5.5 wt% niobium (Nb), 2.8–3.3 wt% molybdenum (Mo), 0.6–1.2 wt% titanium (Ti), 0.2–0.8 wt% aluminum (Al), with the balance primarily iron (Fe) [5]. As summarized in Table 1, IN718 consists of a γ (face-centered cubic) Ni matrix with γ'/γ'' precipitates and carbides. Solution treatment at about 980 °C for 1 h dissolves the prior nano-precipitates, and subsequent two-step aging at 720 °C and 620 °C for 8 h each, precipitates fine γ'' (with some γ'), resulting in precipitation strengthening [6]. Among the alloying elements, Cr provides oxidation and corrosion resistance and can form boundary carbides, Nb drives γ'' and MC formation, Mo adds solid-solution strength, Ti and Al form γ', and C enables MC and $M_{23}C_6$ formation [7]. IN718 also contains topologically close-packed phases, such as δ and Laves phases, which are

---

[*] Correspondence to: Via Privata Giuseppe La Masa, 1, Milano, MI 20156, Italy.
E-mail address: abhinavanand@polimi.it (A. Anand).

https://doi.org/10.1016/j.nxmate.2026.102226
Received 17 February 2026; Received in revised form 2 April 2026; Accepted 5 May 2026

Table 1
Different phases present in IN718 and their representative lattice structures, chemical formulae, solvus temperature ranges, and typical morphologies, compiled from references [7,11–13]. Here, FCC refers to a face-centered cubic lattice, while BCT refers to a body-centered tetragonal lattice.

Phases	Lattice structure	Chemical formula	Solvus temperature	Morphology
γ	FCC	-	1260–1364 °C	continuous matrix; typically equiaxed
γ'	FCC (ordered L_{12})	$Ni_3(Al,Ti)$	850–910 °C	coherent; fine spherical to cuboidal
γ''	BCT (ordered D_{022})	Ni_3Nb	910–940 °C	semi-coherent; thin disc or plate-shaped
MC	Cubic	(Nb,Ti)C	1260–1305 °C	blocky/globular primary carbides
$M_{23}C_6$	FCC	$(Cr,Fe,W,Mo)_{23}C_6$	1050–1100 °C	grain-boundary carbides
M_6C	FCC	$(Fe,Co)_3(Mo,W)_3C$	1080–1130 °C	coarse, irregular, block-shaped carbides
Undesired phases				
Laves	Hexagonal	$(Ni,Fe,Cr)_2(Nb,Mo,Ti)$	1163 °C	irregularly shaped, network-like pools
δ	Orthorhombic	$Ni_3(Nb,Ti)$	1005–1020 °C	needle or plate-shaped precipitates

considered detrimental to the performance of the alloy [8]. These phases tend to form plate-like structures during heat treatment or extended service conditions, and their presence can deplete key strengthening elements such as Nb and Ti from the matrix, which are crucial for the γ'/γ'' precipitation [9]. These brittle phases reduce ductility and serve as potential sites for crack initiation under cyclic loading [10].

1.2. Conventional manufacturing route

IN718 is conventionally produced either by casting or by wrought (thermomechanical) processing. Casting (commonly investment casting) involves pouring molten IN718 into ceramic molds to achieve near-net shape of intricate components such as turbine blades, vanes, or casings, and it permits highly alloyed compositions to be shaped into parts that offer excellent creep resistance at high temperatures [14]. By controlling solidification rates, cast IN718 can be made with equiaxed, directionally solidified, or even single-crystal grain structures, which improves high-temperature creep performance by reducing grain-boundary sliding [15]. However, casting often produces chemical segregation and porosity in the microstructure, so the manufactured parts must undergo post-solidification heat treatments to homogenize elemental distribution, optimize γ'/γ'' strengthening precipitates, and eliminate defects [16].

In contrast, the wrought route for IN718 begins with melting and remelting to produce high-purity ingots, followed by hot working (forging, rolling, or extrusion), and then solution annealing and aging. This thermomechanical processing refines the grain structure and yields a uniform, precipitate-strengthened microstructure, giving wrought IN718 significantly higher and more consistent mechanical properties than the cast material [17]. Wrought IN718 is thus preferred for critical high-load parts (e.g., compressor disks and rings in aero-engines) that demand superior yield strength, fatigue life, and toughness, enabling the tailoring of anisotropic mechanical properties to align with the primary load directions [18]. However, wrought processing is limited to simpler geometries, such as producing standard billets like plates or rings that require machining to the final shape.

In summary, casting enables complex shapes manufacturing but at the expense of microstructural nonhomogeneity, such as segregation, porosity, and coarse dendrites, while wrought IN718 provides excellent and reliable properties but is constrained in shape complexity and buy-to-fly ratio. These inherent limitations in conventional casting and wrought routes have prompted the pursuit of new manufacturing approaches to exploit the performance of IN718 in advanced aerospace components [19].

1.3. Additive manufacturing

To overcome the constraints of conventional manufacturing, additive manufacturing (AM) emerged in the late 1980s and has since matured into a production route for aerospace components [20]. AM manufactures parts directly from a 3D CAD model by adding material layer by layer, producing near-net-shape components with minimal waste and fewer geometric constraints than casting or forging. Originally developed for rapid prototyping and fast design iteration, AM is now used to produce qualified end-use parts, enabling optimized lightweight designs, functionally graded or multi-material sections, and repair of damaged components [21,22]. Blakey-Milner *et al.* have provided a comprehensive review of metal AM in aerospace, covering different processes, design benefits, cost and lead-time gains, certification challenges, and representative application case studies [23]. For IN718, AM can fabricate parts that are not feasible by conventional routes, such as conformal internal channels for thermal management, topology-optimized lattice infill for mass reduction, and part consolidation that removes joints and associated failure points, all while shortening lead times through rapid digital iteration without adding any tooling costs [24–27].

Metal AM techniques are classified into fusion-based and solid-state routes [28]. Fusion-based methods use thermal energy to completely melt metal feedstock, followed by rapid solidification of each layer. Solid-state methods, by contrast, bond materials below the melting point, avoiding many fusion-related issues caused by melting and resolidification [29]. As mapped in Fig. 1, our to-date literature survey on IN718 across AM routes shows that laser-based powder bed fusion of metals (PBF-LB) accounts for 50% of studies, directed energy deposition (DED) 32%, wire-arc additive manufacturing (WAAM) 7%, electron-based powder bed fusion (PBF-EB) 7%, cold spray additive manufacturing (CSAM) 3%, and other routes 1%. Therefore, in this

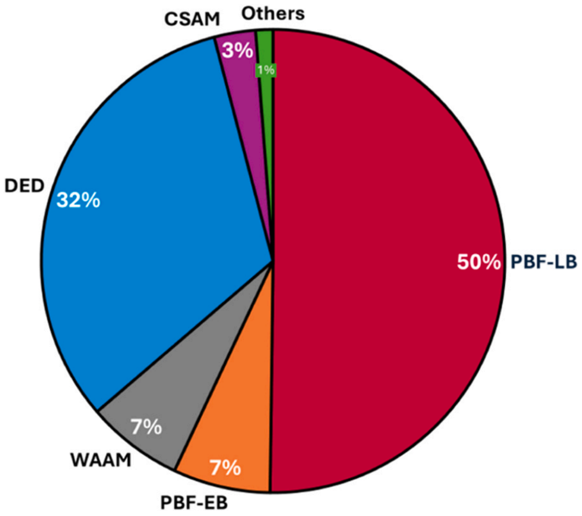

Fig. 1. Percentage distribution of Scopus-indexed peer-reviewed scientific articles (2018–2025) on the fabrication of IN718 via different AM routes, derived from a dataset of 2815 publications.

study, we focus on the fusion-based AM technique, such as PBF-LB, DED, and WAAM. Within PBF, we restrict the discussion to the laser-based route because PBF-EB runs under vacuum and employs substantial powder-bed preheating, which results in a different thermal history and thus different residual-stress and microstructural evolution conditions compared with other fusion-AM routes [30–32]. A rigorous comparison would therefore require a dedicated framework for PBF-EB and is outside the scope of the present process-to-process benchmarking. For the solid-state category, we include only CSAM because it offers the most studied IN718 literature among solid-state deposition routes, including datasets that can be directly compared with fusion-based AM. Other solid-state processes for IN718, such as ultrasonic AM, additive friction stir deposition, and diffusion bonding-based AM, currently have sparse, non-comparable property datasets.

1.4. *Scope of the review*

Existing reviews provide useful context on mechanical property trends in fusion-based AM and on CSAM process fundamentals, but they do not offer a process-based comparison of fusion-based and solid-state AM focused specifically on IN718. Hosseini and Popovich [19] reviewed the mechanical properties of additively manufactured IN718 with emphasis on fusion-based routes. Sample *et al.* [33] did a literature survey on quasi-static and fatigue-related behavior for CSAM components and repairs, with most of the discussion centered on aluminum alloys. More recently, Sudigdo *et al.* [34] reviewed CSAM Ni-based superalloys, describing particle bonding mechanism and interface formation, and relating these features to processing parameters and residual stress, while other articles provided broad overviews of recent advances in manufacturing routes for Ni-based superalloys [35,36].

In contrast, the present review focuses on IN718 and compares solid-state CSAM against fusion-based AM in terms of as-built microstructures, microstructural evolution under post-processing heat treatments, and reports mechanical performance, with discussions on fracture toughness, fatigue strength, and fatigue crack growth used in durability and damage-tolerance assessments. Although IN718 is commonly used at elevated temperatures, the scope of our paper is restricted to room-temperature mechanical performance because high-temperature mechanical datasets are not yet reported with sufficient consistency across fusion-based AM routes to enable a detailed process-to-process comparison. This limitation is even more pronounced for CSAM, where high-temperature mechanical property data remain scarce due to the relatively early stage of process adoption for IN718.

In the present review, the term 'durability' refers to resistance to crack initiation and cyclic degradation during service, whereas 'damage tolerance' refers to the ability of a component to sustain an initial flaw and continue to operate safely under defined loading and inspection conditions. For mechanical property benchmarking, the room-temperature bands of AMS 5662 [37] and AMS 5383 [38] are used as wrought-aged and cast precipitation-hardened reference states, to compare the additively manufactured IN718 data against conventional aerospace material baselines. Throughout this review, the term as-built is used as a general descriptor for the initial condition after fabrication; for the individual AM routes, this corresponds to the as-built state in PBF-LB, the as-deposited state in DED-LB and WAAM, and the as-sprayed state in CSAM.

In the next section, a brief overview of the AM routes considered in this review is provided, first for the fusion-based AM routes for IN718, followed by a detailed discussion of CSAM covering the process workflow, applications, and the key differences from fusion-based AM. The subsequent section discusses the effects of post-processing heat treatments on microstructure, tensile properties, and fracture toughness across the reviewed AM routes. Next, high-cycle fatigue strength and room-temperature fatigue crack growth trends are reviewed in relation to microstructure, surface condition, and build orientation. The review then concludes by summarizing the main findings and identifying key research gaps that should be prioritized in future studies.

2. Additive manufacturing routes

2.1. *Fusion-based additive manufacturing*

PBF-LB is a fusion-based AM process in which a laser scans and fully melts selected regions of a thin metallic powder layer (tens of micrometers). The scan strategy is defined by a build job that slices the CAD geometry (often exported as STL), converting it into layer-wise contours and scan vectors, which are executed by the machine. The build platform then lowers, and a fresh layer is recoated, repeating until the part is built under an inert atmosphere in the build chamber (Fig. 2 **(a)**) [39]. This process enables component fabrication with very fine feature resolution and complex internal geometries. Key advantages include excellent dimensional accuracy, low surface roughness, and fully dense metal parts that require minimal machining [40]. The main disadvantages are slow build speed, constrained part size due to the limited build envelope, and high capital cost [41]. PBF-LB often requires support structures for overhangs and can introduce residual stresses and anisotropy from rapid solidification [42]. Often, the IN718 process parameters window includes laser power of 200–400 W, scan speed of 600–1200 $\mathrm{mm \cdot s^{-1}}$, hatch spacing of 80–120 μm, layer thickness of 20–60 μm, and laser spot of 60–100 μm [43]. To manage thermal gradients and reduce warping or cracking in IN718, base-plate preheating (80–200 °C) is required, followed by stress-relief heat treatment of as-built samples and support removal [44].

As shown in Fig. 2 **(b)**, DED is a directed-feed AM process in which a localized heat source (laser, electron beam, or arc) forms a melt pool while wire or powder is delivered to that location through a nozzle under shielding gas, so material is deposited only where needed as the head moves in 3D to build the part layer by layer [46]. This multi-axis process can also deposit material onto existing parts or substrates (useful for repairs) and even combine different alloys in a single build, with no limits on part size. In this review article, only laser-based DED of metals, i.e., DED-LB, has been covered. For DED-LB IN718, in case of powder-fed, laser power 0.6–2.0 kW, transverse speed 5–15 $\mathrm{mm \cdot s^{-1}}$, spot size 0.6–1.8 mm, powder feed 5–20 $\mathrm{g \cdot min^{-1}}$, layer thickness 0.3–1.0 mm, and track spacing 0.6–1.5 mm is typically applied [47]. For wire-fed DED, laser power 1–6 kW, travel speed 5–20 $\mathrm{mm \cdot s^{-1}}$, spot size 1–3 mm, wire diameter 0.8–1.6 mm at 1–5 $\mathrm{m \cdot min^{-1}}$ feed rate, layer thickness 0.8–2.5 mm, and track spacing 1–3 mm are used [48]. In both cases, argon shielding is mandatory to avoid oxidation [49]. The advantages of DED-LB include very high deposition rates, scalability to large structures, flexibility of feedstock, and fabrication of multi-material components [46]. Drawbacks include a relatively coarse resolution, limited geometry complexity, and a poor surface finish, resulting from thicker layers and larger melt pools. The higher heat input in DED-LB also results in significant residual stress and distortion, and the as-built parts typically require machining and heat treatment after fabrication [50]. In aerospace, DED-LB is relevant for producing as well as refurbishing larger-sized IN718 components (e.g., turbine disk sections or rocket chamber inserts) where its high throughput and ability to fuse onto existing metal are valuable, at the expense of fine detailing [51].

Fig. 2 **(c)** depicts WAAM, a subtype of DED that uses an electric arc welding heat source, typically metal active/inert gas (MIG/MAG) or tungsten inert gas (TIG), to melt a continuously fed metal wire [52]. The process is an automated welding operation where an arc is struck between the wire electrode and substrate, melting the wire into beads, and a robot moves the torch to stack-weld the beads into layers. WAAM operates at very high deposition rates (roughly 1–10 $\mathrm{kg \cdot h^{-1}}$) but with low precision. IN718 parameter ranges in WAAM are current of 150–300 A, arc voltage 18–30 V, wire feed 3–10 $\mathrm{m \cdot min^{-1}}$, travel speed 5–15 $\mathrm{mm \cdot s^{-1}}$, bead width 4–10 mm, and layer height 1–3 mm, with Ar shielding, while MIG/MAG variants may also employ Ar-$\mathrm{CO_2}$ blends

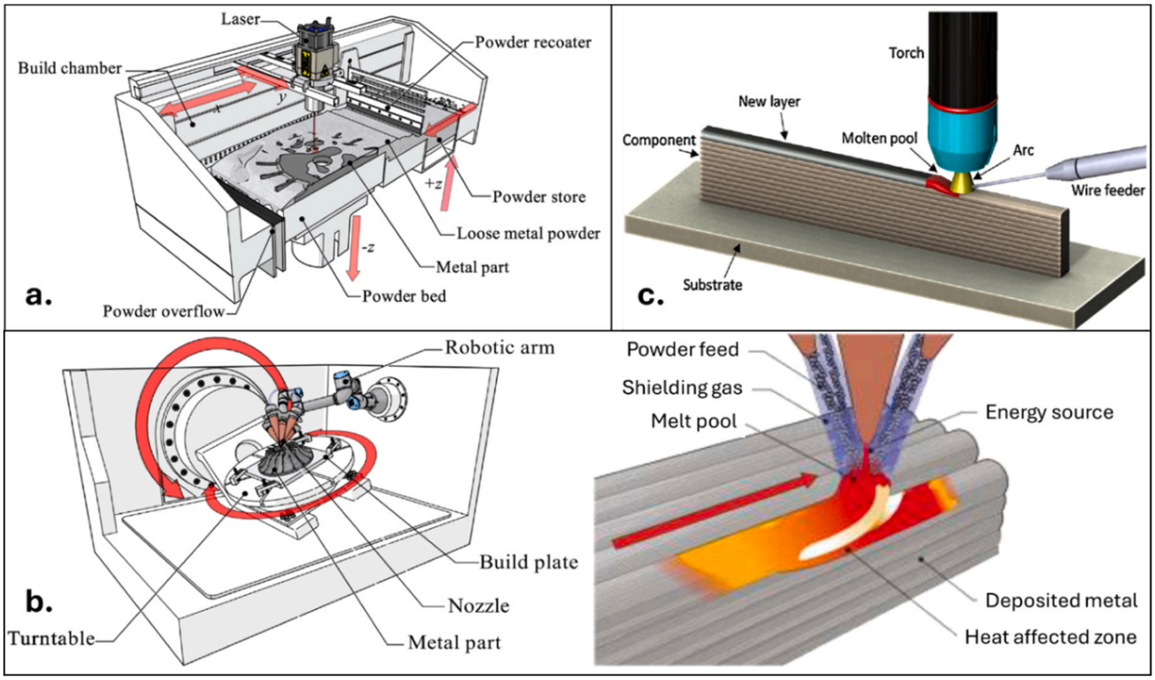

Fig. 2. Schematics of fusion-based metal AM routes: (a) PBF-LB, (b) DED, and (c) WAAM [39,45]. (Reproduced under the Creative Commons CC-BY license).

[53]. Its main advantages are low equipment cost and the ability to build very large structures quickly with layer resolutions in the order of millimeters [54]. Compared to laser-based AM, the throughput and material efficiency of WAAM are superior, and it uses readily available welding power supplies. WAAM also shows high energy efficiency (often ~ 80–90%), whereas reported laser-beam AM process efficiencies can be as low as ~ 2–5% [55]. However, WAAM sacrifices detail and quality, and the built parts have coarse microstructures, substantial thermal distortion, and a rough surface finish. The as-built components need to undergo thorough post-machining and heat treatment to meet aerospace standards. In practice, WAAM of IN718 is applied to large pressure vessels or rocket components where a near-net shape deposition of a high-performance superalloy is needed at a higher deposition rate, and subsequent machining to achieve tight tolerances is acceptable [56].

2.2. *Cold spray additive manufacturing*

CSAM is a solid-state process that deposits metal powders at supersonic velocities, causing severe plastic deformation upon impact and bonding the material without melting it [57]. Fig. 3 shows a high-pressure CSAM setup, in which process gas (usually nitrogen) is pressurized and preheated by an electric heater, then combined with metal powder feed and directed through a convergent-divergent (de Laval) nozzle, propelling particles to supersonic velocities. As the particles exit the nozzle and impact the substrate, their kinetic energy is converted into extreme plastic deformation, breaking surface oxides, and inducing adiabatic shear, which results in mechanical interlocking and localized metallurgical bonding between the particles and the substrate [58]. Since the powder remains below its melting point, layers form entirely in the solid state, i.e., without formation of a melt pool or resolidification, which helps avoid fusion-AM-related defects (hot cracking, segregation) and large thermal residual stresses [59]. CSAM

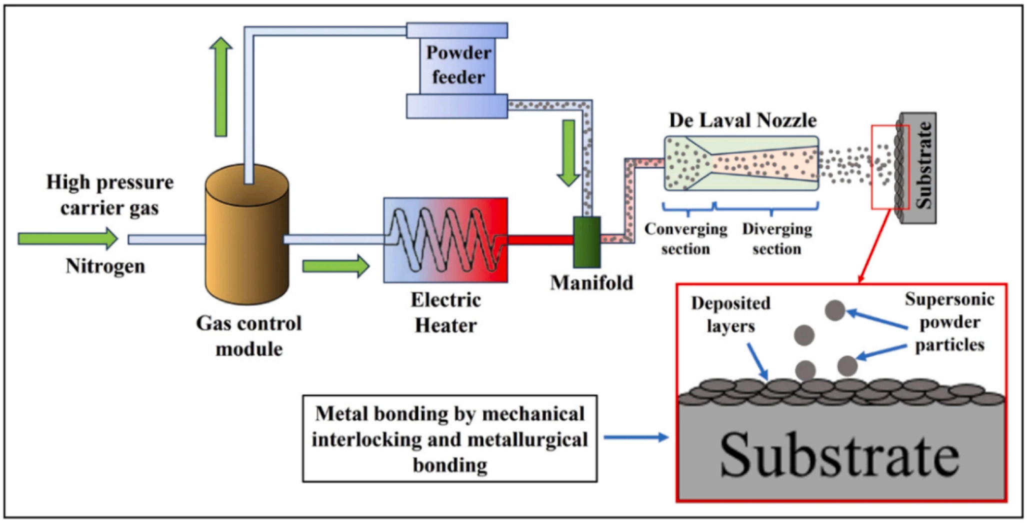

Fig. 3. Schematic depicting a high-pressure CSAM setup [61]. (Reproduced with permission from Springer Nature).

route yields dense, oxidation-free deposits and is a suitable route for IN718 coatings, repairs, and near-net shape builds where minimal thermal exposure is critical [60]. CSAM systems are classified as low-pressure or high-pressure, and the latter (gas pressure > 1.5 MPa) is most common for dense metal deposition and will be the focus of this review.

In high-pressure CSAM IN718, deposit quality is governed mainly by particle velocity and exit temperature, with spray angle, substrate condition, and nozzle design providing secondary control [62,63]. For depositing IN718 powders on hard substrates such as superalloys, a polished surface concentrates interfacial shear, promotes jetting, disrupts surface oxides, and enables metallurgical bonding [64]. In case of depositing IN718 powders on softer substrates such as aluminium alloys, controlled roughness ($R_a = 3–6$ μm) reduces particle rebound, increases local contact pressure, and anchors the first layers [65]. For both substrates, a practical spray-angle range is 60–90°. At a given angle, increasing particle exit velocity and gas temperature generally reduces porosity by raising impact energy and thermal softening, which increases the extent of plastic deformation (plastic strain) under high-strain-rate impact conditions, promotes localized adiabatic shear, breaks surface oxides, and enlarges the true contact area at particle-substrate and inter-particle interfaces, thereby strengthening metallurgical bonding [66].

CSAM IN718 uses gas-atomized powders similar to those widely used in fusion-based AM routes. It does not require a special powder chemistry or a uniquely narrow particle size range. In practice, CSAM uses spherical and free-flowing powders in the tens of micrometres regime, which overlaps with the size classes commonly used for PBF-LB and DED-LB. As shown in Fig. 4, the polished particle cross-section of IN718 powder reveals a dendritic solidification substructure formed during atomization, reflecting rapid solidification and microsegregation within each particle, with solute enrichment in interdendritic regions. The TEM image shows a γ matrix with low dislocation density in the as-received powder.

Using N_2 as the carrier gas, IN718 is usually sprayed at 4–6 MPa gas pressure and 950–1000 °C gas temperature. Gas-atomized powder of 10–45 μm is fed at the rate of 10–60 $g\cdot min^{-1}$ using a de Laval nozzle with 25–60 mm standoff distance, with a traverse speed of 100–300 $mm\cdot s^{-1}$ and 50–70% track overlap. Substrate preheating in the range 150–250 °C is sometimes applied to lower its flow stress and oxide strength at the interface and to facilitate fast diffusion and improve formation of adiabatic shearing instability between the powder and the substrate [67]. The literature studies compiled in Table 2 show that dense IN718 deposits have been fabricated under different combinations of powder size range, substrate material, and spray conditions. The reported values indicate that a quality deposit is achieved across a range of conditions, with the final porosity determined by the combined effects of feedstock characteristics, substrate type, nozzle/setup, and selected process parameters.

Table 2
Literature summary of CSAM Inconel 718 deposition using N_2 as the process gas, with the reported substrate material, powder size range, gas temperature, gas pressure, and porosity.

Substrate	Powder size (μm)	Process parameters		Porosity (%)	Reference
		Gas temperature (°C)	Gas pressure (bar)		
IN718	10–45	1000	45	1.7	[68]
	17–45	1000	50	1.3 ± 0.1	[69]
	8–50	1000	70	1.82 ± 0.46	[70]
	10–31	800	40	0.2–0.5	[71]
	9–20	950	40	0.4 ± 0.2	[72]
	25–45	1000	45	2.5	[73]
	16–30	1000	70	1.04 ± 0.85	[74]
	15–27	1000	70	1.7 ± 0.2	[75]
	15–45	950	50	3–4	[76]
Al	10–32	1000	55	1.2 ± 0.2	[77]
	5–25	840	35	4.0 ± 0.2	[78]
	7–36	950	50	2.49	[79]
316 L	7–37	1000	100	0.05	[80]

A recent study by Li *et al.* [81] has described an integrated modular CSAM setup that mirrors the workflow shown in Fig. 5**.** Flowchart detailing several steps involved in the CSAM process. The first stage in CSAM involves acquiring a digital model of the part or repair feature. If a CAD design is available, it is used directly. Otherwise, the existing geometry must be captured by 3D scanning, as in the case of repairing worn parts. In parallel, powder is sieved and often dried or degassed. The substrate preparation involves masking and fixing, followed by grit-blasting and cleaning. Before spraying, CSAM uses specialized deposition modeling to predict how powder will build up on each layer. A numerical model takes the part geometry and simulates the deposition footprint of the spray gun over the substrate. For example, a mesh-based simulation computes where the spray footprint intersects the build surface and accumulates triangular facets layer by layer, predicting edge loss and layer thickness as a function of CSAM parameters, such as standoff distance, spray angle, and robot speed. Such modeling is critical because CSAM must compute the growing deposit explicitly. In fusion AM, standard slicing and thermal models are well established, but in CSAM, custom deposit-shape simulations are often required to plan the scan paths and parameter set needed to achieve the target geometry and thickness before spraying.

The next stage is path planning, in which the build is sliced into layers, and the robot nozzle path is generated for each layer. Unlike PBF-LB, where the laser scan over the powder bed can be stopped locally, continuous material-feed processes (DED, WAAM, CSAM) have a finite on/off response due to feed and process dynamics. In CSAM, this can cause overspray at the start and end of each pass. Therefore, spray-

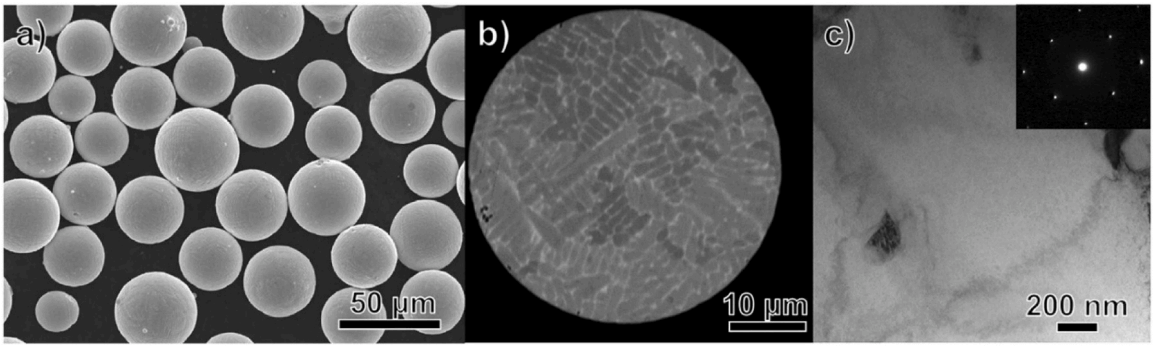

Fig. 4. a) SEM image of gas-atomized spherical IN718 powder, (b) cross-section of the particle showing dendritic solidification substructure formed during atomization, and (c) TEM bright-field image showing low dislocation density [68]. (Reproduced with permission from Elsevier).

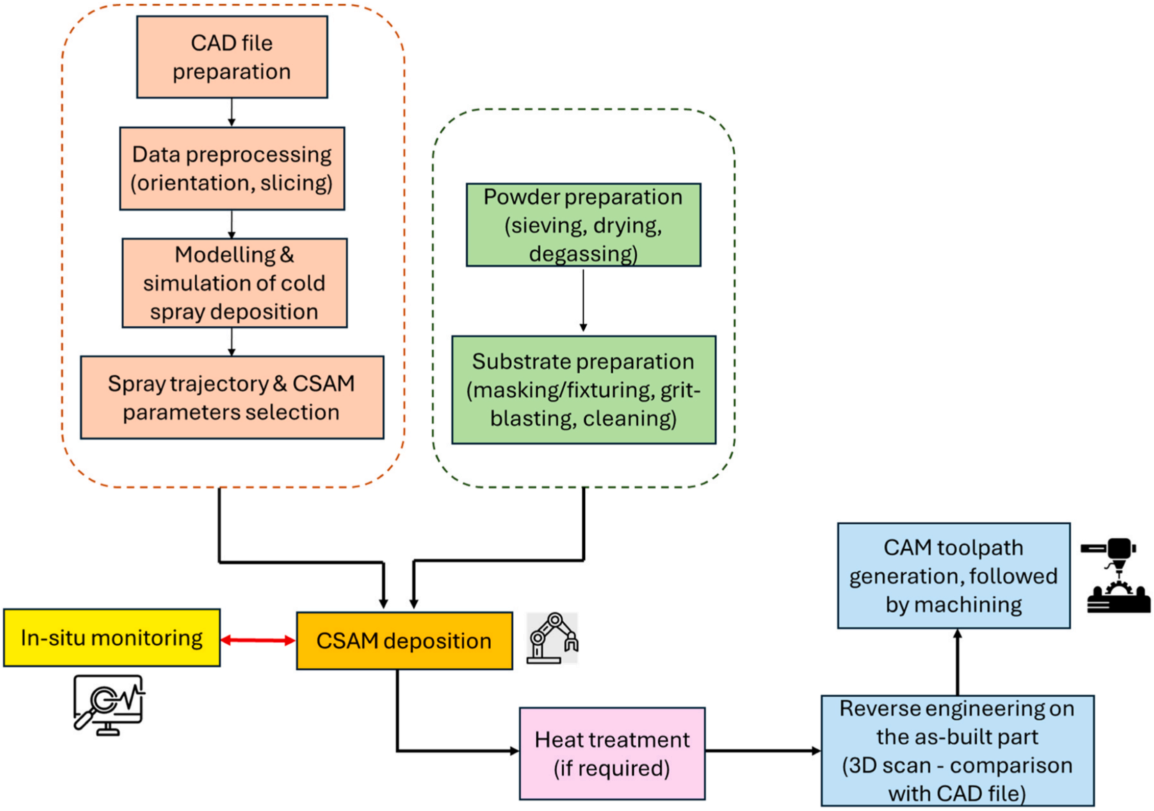

Fig. 5. Flowchart detailing several steps involved in the CSAM process.

trajectory planning must generate continuous robot paths and transfer moves that cover each slice uniformly while avoiding unintentional deposition. During the CSAM process, an industrial robot executes the planned paths while in-situ monitoring (e.g., laser profiling of layer height and bead shape, and thermal cameras for surface temperature) tracks the build surface and triggers on-the-fly process parameter adjustments [82]. Post-build, the as-deposited CSAM part is 3D-scanned and compared with the initial CAD file to generate CAM toolpaths for subtractive finish machining, which is needed because lower dimensional accuracy in CSAM can induce overbuild, waviness, and burrs. Excess material is then milled off to meet final dimensions and surface quality. Heat treatment, such as annealing, can be done to remove residual stress or to impart ductility for easier machining.

Fig. 6 compares the AM parts across different routes with PBF-LB delivering an as-built, fine-resolution IN718 nozzle with conformal channels, DED-LB producing an as-built, thin-walled IN718 nozzle, CSAM and WAAM generating high-throughput preforms that require CNC finishing to reach aerospace tolerances. The green arrow indicates that geometric complexity and build preparation time and cost increase toward PBF-LB, while the blue arrow shows a decrease in as-built dimensional accuracy, resolution, and surface finish from PBF-LB to DED-LB to CSAM and WAAM.

Fig. 7 maps technology readiness versus industrial adoption of different AM processes. PBF-based processes cluster in the broad industrial deployment/high-technological readiness region, while DED-LB and WAAM are placed at near-operational deployment. CSAM is at

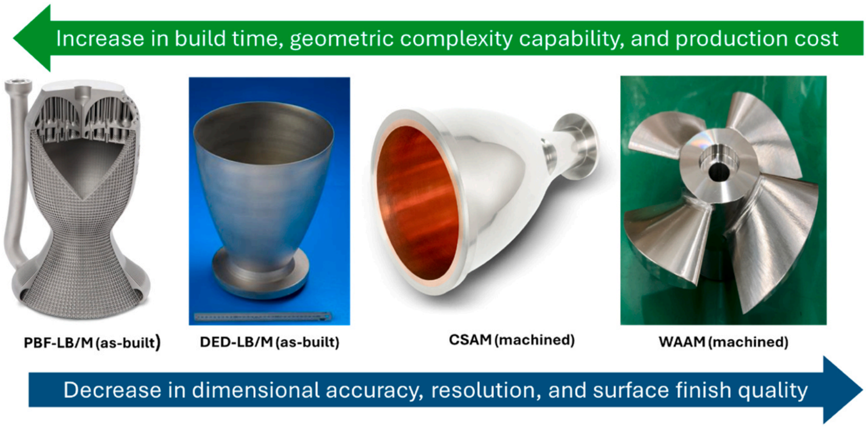

Fig. 6. As-built single-piece rocket propulsion engine with structural cooling design via PBF-LB IN718 [83] (Copyright:© SLM Solutions/ CellCore), as-built IN718 rocket nozzle manufactured via DED-LB [84] (Copyright:© TWI Ltd), a machined rocket nozzle fabricated with copper inside and nickel on the outside using CSAM [85] (Copyright:© Impact Innovations GmbH) and machined IN718 blade fabricated via WAAM [86]. (Reproduced under the Creative Commons CC-BY license).

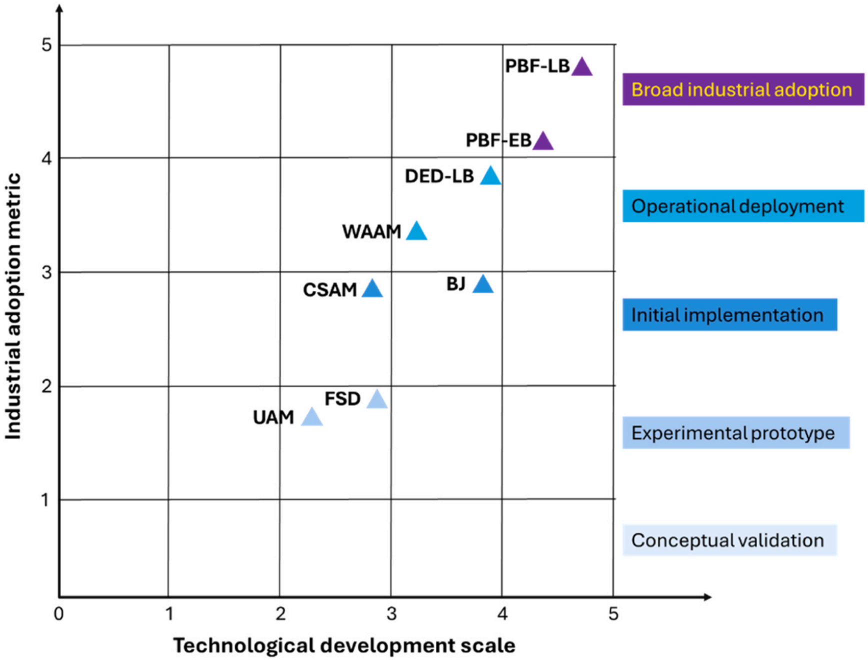

Fig. 7. Comparison of different AM technologies in terms of relative technology readiness and industrial adoption (from concept to broad deployment). BJ refers to binder jetting, FSD denotes friction stir deposition, and UAM represents ultrasonic additive manufacturing. Data has been referenced from [87].

initial implementation due to promising results for free-standing non-complex geometrical components and structural repairs via solid-state, low-heat input manufacturing, yet constrained by limited standardization and certification frameworks, smaller datasets for cyclic and high-temperature mechanical properties, and fewer fielded applications in industrial setups. However, recent market studies project the CSAM market to grow 6–7% per year from 2025 to 2030, suggesting an increasing demand for applications like component repair, even as CSAM currently lags behind fusion AM methods in maturity [88].

As illustrated in Fig. 8, Waugh *et al.* [85] have demonstrated multi-material deposition capability of CSAM for a regeneratively cooled chamber in which a CuCrZr liner is first cold-sprayed onto an Al mandrel, coolant channels are machined and filled with an Al-based sacrificial filler, and finally an IN625 structural jacket is sprayed over the liner. This multi-material build integrates the copper liner and Inconel jacket in a single assembly and avoids welding or brazing, since the removable filler can later be chemically dissolved to reveal smooth internal channels. Also, Schmitt *et al.* [89] (Fig. 9) have demonstrated that CSAM can repair a large IN718 cavity by depositing a uniform, smooth layer that fills the void volume. The repaired surface replicates the target profile without defects, with processing conditions yielding consistent microstructure, good adhesion, and uniform topography.

Table 3 compares PBF-LB, DED-LB, WAAM, and CSAM across build-size limit, dimensional accuracy, surface roughness, feature resolution, deposition rate, cost, support needs, multi-material capability, and use-case fit. PBF-LB offers the highest accuracy and finest finish at a high capital cost and limited volume. DED-LB provides moderate accuracy with 1–5 kg/h build rates and strong cladding and repair capability. WAAM enables large, high-throughput builds at low capital intensity but yields coarse features and rough as-built surfaces that need machining.

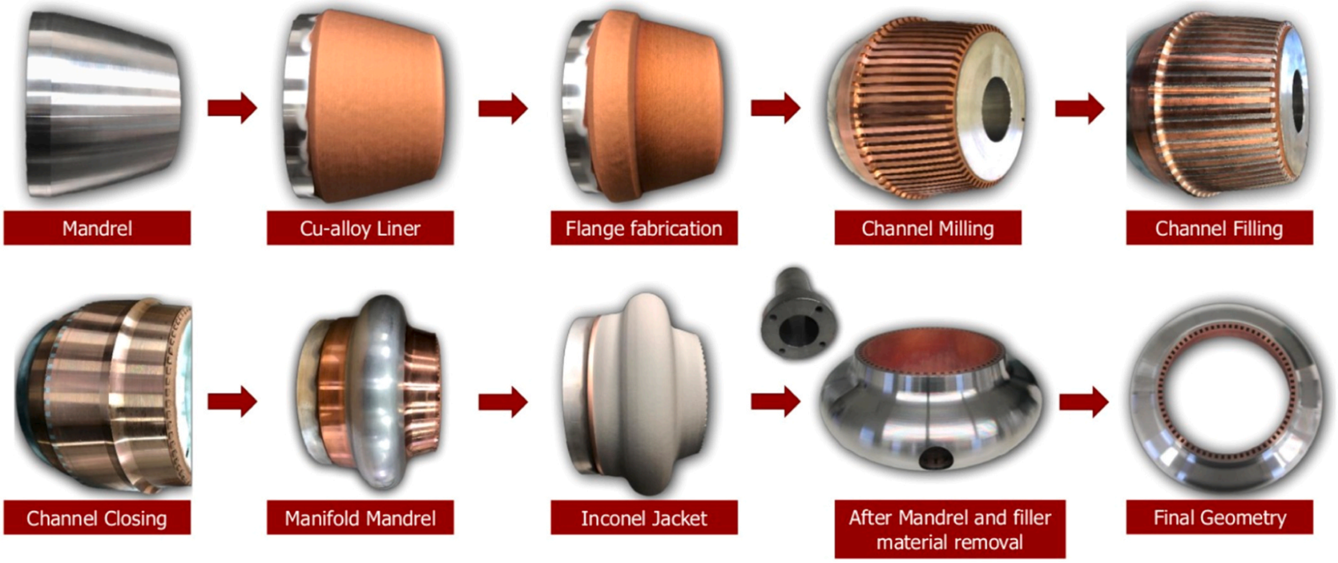

Fig. 8. Fabrication sequence for the CSAM multi-material manifold [85]. (Courtesy: Airborne Engineering Ltd. and Impact Innovations GmbH).

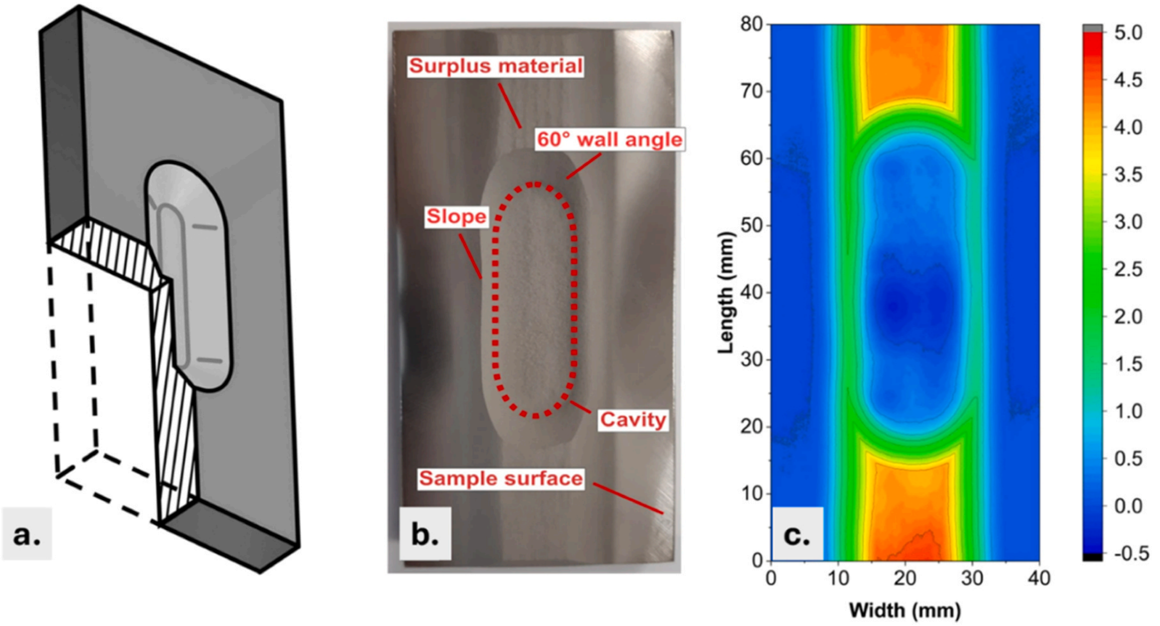

Fig. 9. IN718 machined-cavity repair by CSAM: (a) sample geometry with the machined cavity, (b) representative as-deposited cavity topography, and (c) 2D height-contour map of the CSAM-repaired cavity surface [89]. (Reproduced under the Creative Commons CC-BY license).

Table 3
Comparison table of fusion AM process versus solid-state CSAM across key metrics, compiled from references [53,55,59,67,87,90–101].

Metric	PBF-LB	DED-LB	WAAM	CSAM
Part dimensions	600 mm× 600 mm x 600 mm	Unlimited	Unlimited	Unlimited
Dimensional accuracy (as-built)	High: 0.08–0.10 mm	Medium: 0.3–1 mm	Low: 0.8–2 mm (machining required)	Low: 1–2 mm (machining required)
Surface finish (R_a, as-built)	~ 5–15 μm	~ 15–40 μm	~ 50–100 μm	~ 15–60 μm (depends on build height)
Feature resolution	Fine: ~ 0.1–0.4 mm	Moderate: ~ 0.5–1.0 mm	Coarse: ~ 2–4 mm	Coarse: ~ 3–10 mm (depends on nozzle)
Build rate	~ 0.1–0.2 kg/h	~ 1–5 kg/h	~ 4–10 kg/h	~ 5–10 kg/h
Cost effectiveness (€/kg deposited)	Low (best for small, complex)	Medium	High	High for repair, coatings, and free-standing samples
Setup cost	Very high	High	Low	High
Support structures needed	Often	Rarely	Rarely	Not needed
Ease of multi-material deposition	Limited - hopper change, cross-contamination risk	Excellent - multiple powder feeders, graded builds	Good - dual wire/tool change, composition steps	Excellent - multiple powder feeders and graded blends are routine
Repair on existing parts	Limited	Excellent (feature rebuilds)	Good (large build-ups)	Excellent (standard use case)
Coating/cladding suitability	Not possible	Excellent (laser cladding)	Fair (thick overlays)	Excellent (primary)
CO_2 release and energy intensity (per kg)	High	Medium	Low–Medium	Medium–high (gas compression; He cost↑)

CSAM supports unlimited size and graded multi-material deposition, excels in repair and coatings, and requires finish machining, while its operating cost depends on process gas.

3. Microstructure, tensile properties, and fracture toughness of additively manufactured IN718

3.1. Laser-based powder bed fusion

In PBF-LB IN718, the highly localized melt pool and rapid cooling introduce extremely steep thermal gradients, so that solidification is strongly directional [102]. Long, epitaxial columnar γ grains grow along the build direction and appear as fibre-like features that are best resolved on a longitudinal (parallel-to-build) cross-section, while the transverse (perpendicular-to-build) cross-section reveals the finer cellular or dendritic substructure (Fig. 10 **(a,b)**). The rapid solidification also drives a strong microsegregation, resulting in the partitioning of Nb and Mo into the interdendritic liquid, precipitating a continuous Nb-Mo-rich Laves phase at the grain boundaries (Fig. 10 **(e)**) while no γ'/γ'' precipitation is observed [103].

Table 4 lists the commonly used heat treatment routes in fusion-based AM: DA (double aging), SA (solutionizing followed by double aging), HSA (homogenization plus SA), and HA (homogenization plus double aging). The standard SA treatment, commonly used for wrought components, largely reduces this microsegregation. Most of the Laves phase dissolves into the γ matrix and reprecipitates as γ'/γ'' and δ, but Nb-rich regions and some residual Laves remain in interdendritic zones.

By contrast, HSA treatment, which includes homogenization followed by SA, fully dissolves the Laves phase, redistributes Nb uniformly, and yields complete recrystallization of the γ matrix (Fig. 10 **(c,d)**). After the as-built sample undergoes HSA, a fine dispersion of δ-Ni_3Nb reappears (Fig. 10 **(f)**) because the SA step lies below the δ solvus of 1020 °C [104]. Thus, the Nb released during homogenization is thermodynamically driven to reprecipitate as δ during the SA step. In summary, PBF-LB IN718 solidifies into columnar grains with Laves-rich segregation. Therefore, an initial homogenization step is needed to dissolve Laves and recrystallize the matrix. After HSA, γ'/γ'' precipitates form together with δ.

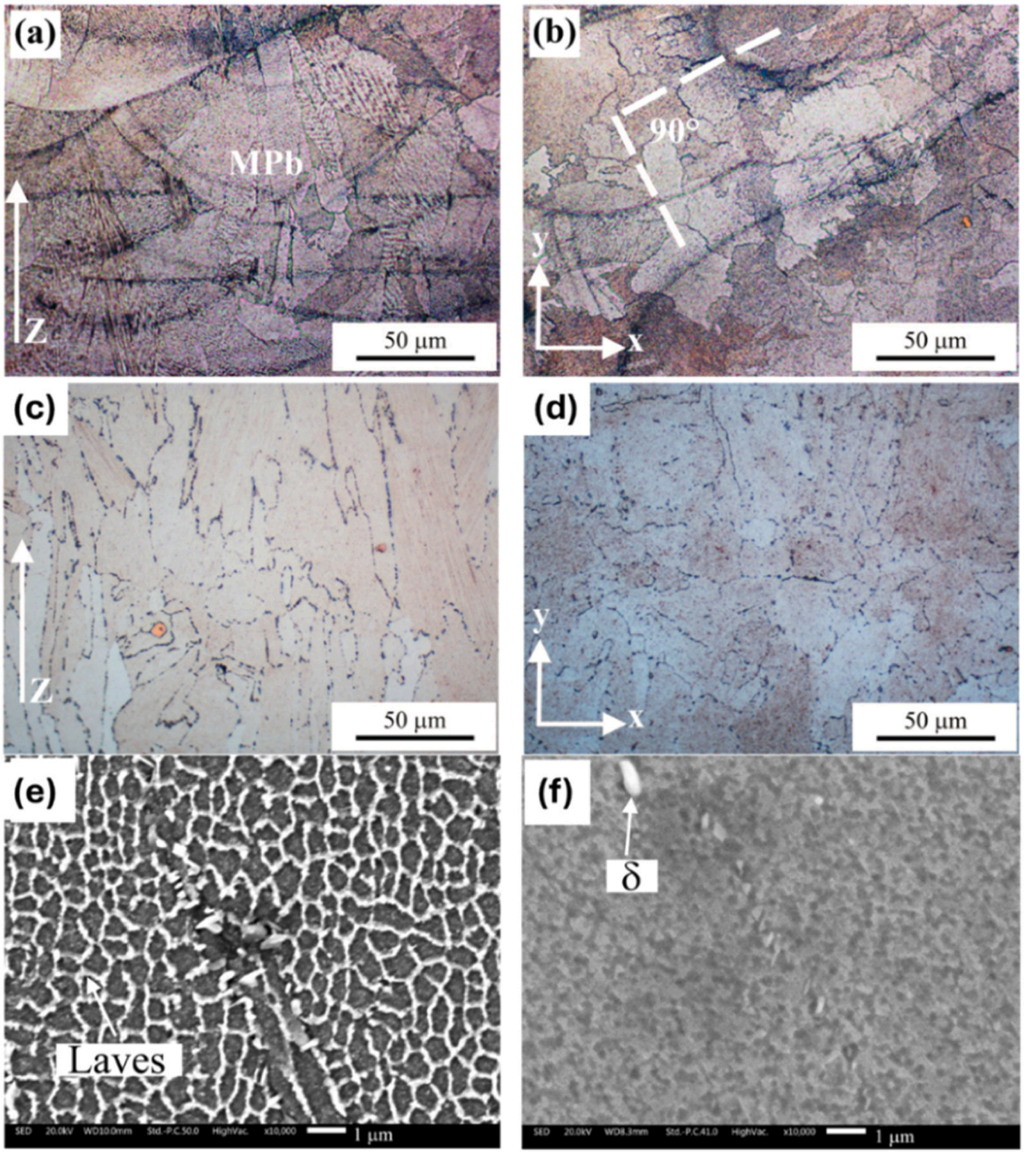

Fig. 10. PBF-LB IN718 microstructures: (a,b) as-built melt-pool boundaries and columnar growth along build direction (z), (c,d) HSA resulting in recrystallized γ with melt-pool no longer visible, (e) as-built SEM showing interdendritic Laves phase, and (f) SEM images after HSA showing grain-boundary δ phase [103]. (Reproduced under the Creative Commons CC-BY license).

Table 4
Details on different heat treatments employed for fusion-based AM specimens. Here, AC, FC, and WQ denote air cooling, furnace cooling, and water quenching, respectively.

Heat treatment	Processing route
DA	Aging at 720 °C for 8 h + FC to 620 °C and holding for 8 h, and then AC to room temperature
SA	Holding for 1 h at 930–1010 °C, followed by WQ + DA
HSA	Homogenization at 1080 °C for 1 h + FC to 930–1010 °C and holding for 1 h, followed by WQ + DA
HA	Homogenization at 1186 °C for 40 min, followed by WQ + DA

Fig. 11 **(a)** shows that as-built PBF-LB IN718 has intermediate strength with a yield strength (YS) of ~ 850 MPa and ultimate tensile strength (UTS) of ~ 1050 MPa, and high ductility (23% elongation) since there was no γ'/γ'' strengthening phase precipitation [104]. SA and HSA treatments progressively increase strength and hardness at the expense of ductility. SA dissolves much of the interdendritic Laves and precipitates fine γ'/γ'' plates and needle-like δ phase in a recrystallized γ matrix, increasing UTS and YS along with higher hardness due to the γ'/γ'' hardening, but roughly halves the elongation. In comparison, HSA completely removes the Laves phase and produces coarser δ needles and γ'' plates. Therefore, the HSA-treated sample attains the highest strengths (YS ~ 1126 MPa, UTS ~ 1415 MPa) while partially restoring ductility (~ 12% elongation), resulting in a strength-ductility balance. Moreover, HSA-treated PBF-LB IN718 exceeds AMS requirements for cast IN718 and achieves strengths, ductility, and hardness on par with wrought IN718 [105].

Fractography (Fig. 11 **(b–d)**) confirms ductile transgranular failure in all cases [104]. In the as-built state, the fracture surface is covered by a fine, equiaxed dimple field, consistent with void nucleation at numerous small Laves particles, carbides, micropores, and the fine cellular-dendritic substructure. After SA, the overall dimple size remains similar, but the dimples become slightly deeper. The higher density of γ'/γ'' precipitates and fine δ needles, together with residual Laves, increases dislocation storage and provides additional microvoid nucleation sites, so voids initiate readily, but their growth is more

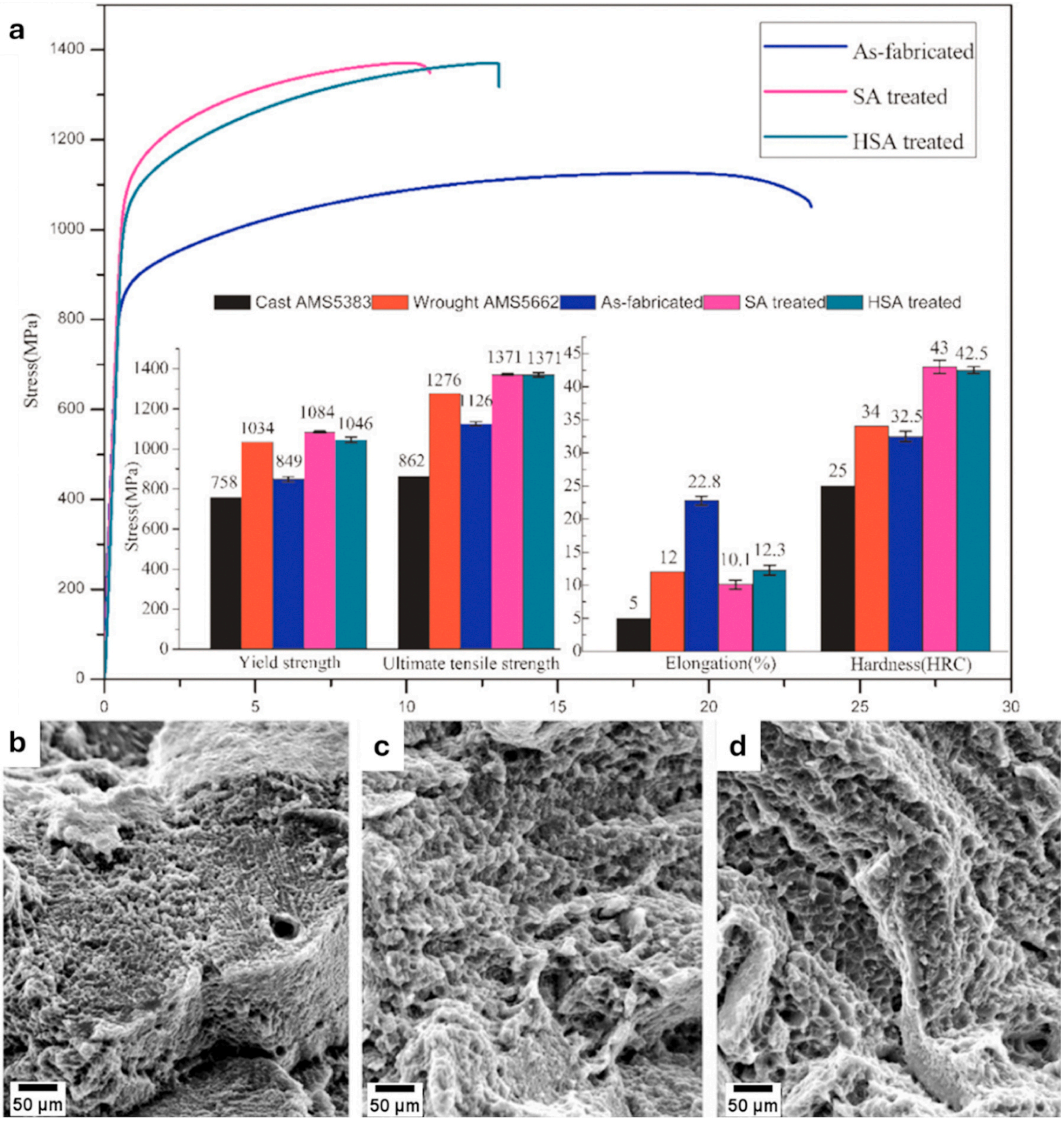

Fig. 11. (a) Mechanical properties comparison of PBF-LB IN718 in as-built, SA, and HSA conditions and fractography of (b) as-built, (c) SA-treated, and (d) HSA-treated PBF-LB IN718 specimens [104]. (Reproduced with permission from Elsevier).

constrained. With HSA, the prior homogenization step dissolves most of the Laves phase and reduces δ to coarser needles mainly at grain boundaries, while recrystallization produces locally larger grains. Consequently, fewer incoherent particles and longer slip lengths allow fewer voids to grow larger before coalescence, so the dimples appear coarser and ductility is partially restored.

Seifi *et al.* [106] reported build-orientation anisotropy in as-built PBF-LB IN718 (Fig. 12), which is expected due to elongated columnar γ grains along the build direction and the strong texture created by directional solidification. Loading parallel versus perpendicular to the build direction results in different grain alignment and dissimilar distributions of melt-pool features and defects, which appear in the tensile curves as orientation-dependent strength and ductility. After hot isostatic pressing (HIP) at 1120 °C and 100 MPa, followed by SA heat treatment, the YS and UTS increased, and the tensile anisotropy was reduced. This trend is consistent with defect closure during HIP, reduced texture effect due to recovery and recrystallization, and subsequent γ'/γ'' precipitation during aging.

Table 5 shows that the fracture toughness decreases after HIP+SA, with only a modest orientation effect. The authors reported the values in K_Q rather than K_{IC} because the plane-strain thickness requirement was not satisfied [106]. The decrease in K_Q after HIP + SA is consistent with the tensile response. The post-processed condition is precipitation-hardened and therefore has higher YS and lower elongation, which reduces crack-tip plastic deformation and limits stable crack growth before fracture. Although HIPing reduces the defect content through pore closure, the dominant effect on the reported toughness in this dataset appears to be the strength-ductility shift produced by the heat treatment, which lowers the K_Q value.

3.2. *Laser-based directed energy deposition*

In DED-LB IN718, the large melt pools and higher volumetric energy density (100–150 J·mm^{-3}) produce coarse epitaxial grains [51,107,108]. EBSD maps, in Fig. 13 **(a)**, show overlapping melt-pool tracks that remain continuous over long scan lengths, together with coarse

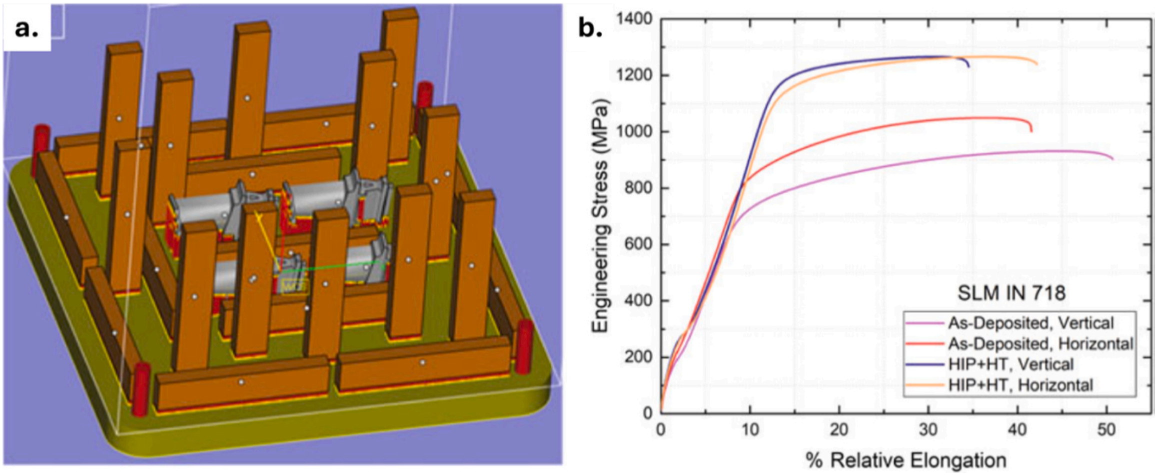

Fig. 12. (a) Schematic build layout of tensile specimens produced by PBF-LB in vertical and horizontal orientation relative to the build direction, and (b) stress-strain curves for IN718 in the as-deposited condition and after HIP+SA [106]. (Reproduced with permission from Springer Nature).

Table 5
Fracture toughness (K_Q) of PBF-LB IN718 in the as-deposited condition and after heat treatment [106].

Specimen orientation	Fracture toughness K_Q (MPa·m$^{0.5}$)
As-deposited (horizontal)	110
HIP+SA (horizontal)	82
As-deposited (vertical)	116
HIP+SA (vertical)	92

columnar γ grains growing along the build direction. By contrast, PBF-LB has a lower melt-pool volume, higher scan speeds, and reduced energy density (60–90 J·mm^{-3}), which increases solidification rates, resulting in the as-built microstructure more commonly exhibiting finer cellular/dendritic substructures within columnar grains [109]. Both DA and SA-treated DED-LB IN718 specimens preserve the columnar pattern (Fig. 13 **(b,c)**). Meanwhile, the HSA treatment cycle promotes static recrystallization, producing a bimodal grain structure with coarse and fine equiaxed grains along with randomized texture (Fig. 13 **(d,e)**) [110].

Similar to PBF-LB, as shown in Fig. 14 **(a,b)**, the as-deposited DED-LB IN718 contains interdendritic eutectic networks of γ and Laves, formed

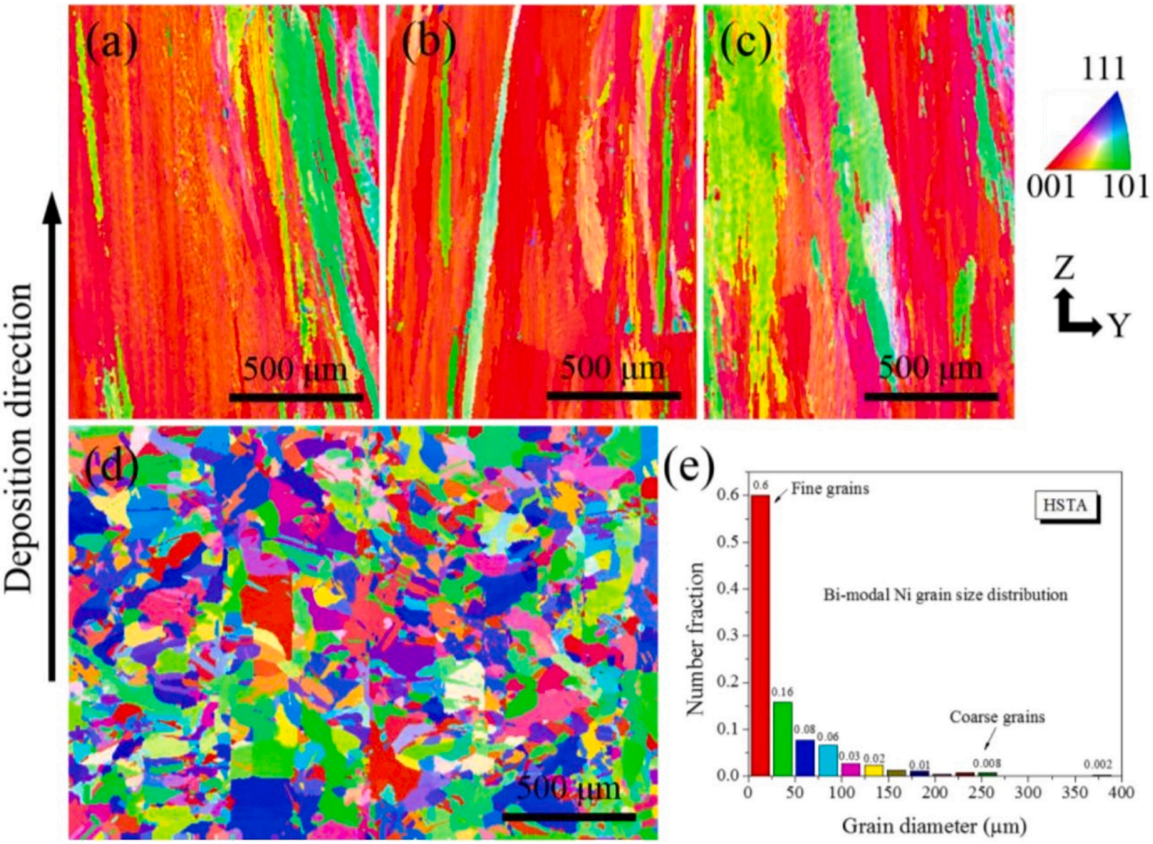

Fig. 13. EBSD IPF maps for DED-LB IN718 in (a) as-deposited, (b) DA-treated, (c) SA-treated, (d) HSA-recrystallized equiaxed, and (e) bimodal grain-size distribution after HSA [110]. (Reproduced with permission from Elsevier).

together with stable NbC carbides, while δ-Ni_3Nb and γ'/γ'' are not detected due to the rapid post-solidification cooling. DA precipitates γ'/γ'' mainly around retained Laves phase with uneven distribution and little precipitation in dendrite cores, while Nb segregation remains unchanged (Fig. 14 **(c,d)**). SA dissolves much of the Laves and, because the solutionizing temperature is below the δ solvus, short acicular δ are formed around the dissolving Laves, and subsequent aging gives a more homogeneous γ'/γ'' field (Fig. 14 **(e,f)**). Finally, HSA completely removes Laves, leaving only NbC, and precipitates γ'/γ'' uniformly in a recrystallized γ matrix while confining δ mainly to grain boundaries (Fig. 14 **(g,h)**). Annealing twins are also evident in HSA-treated samples, arising from static recrystallization during the homogenization step [111].

As shown in Fig. 15, the mechanical properties of DED-LB IN718 vary strongly with the heat treatment. As-deposited specimens show low YS but high ductility due to an unaged γ matrix. DA raises strength via γ'/γ'' precipitation but reduces elongation because the brittle Laves phase remains in the matrix. By dissolving more Laves and introducing δ, SA results in moderately higher strength with intermediate ductility. HSA delivers the best strength-ductility combination due to the removal of segregation, grain recrystallization, and a uniform γ'/γ'' dispersion. Also, the HSA tensile results exceed the minimum requirement of cast AMS 5383 and fall within the specification band for wrought AMS 5662

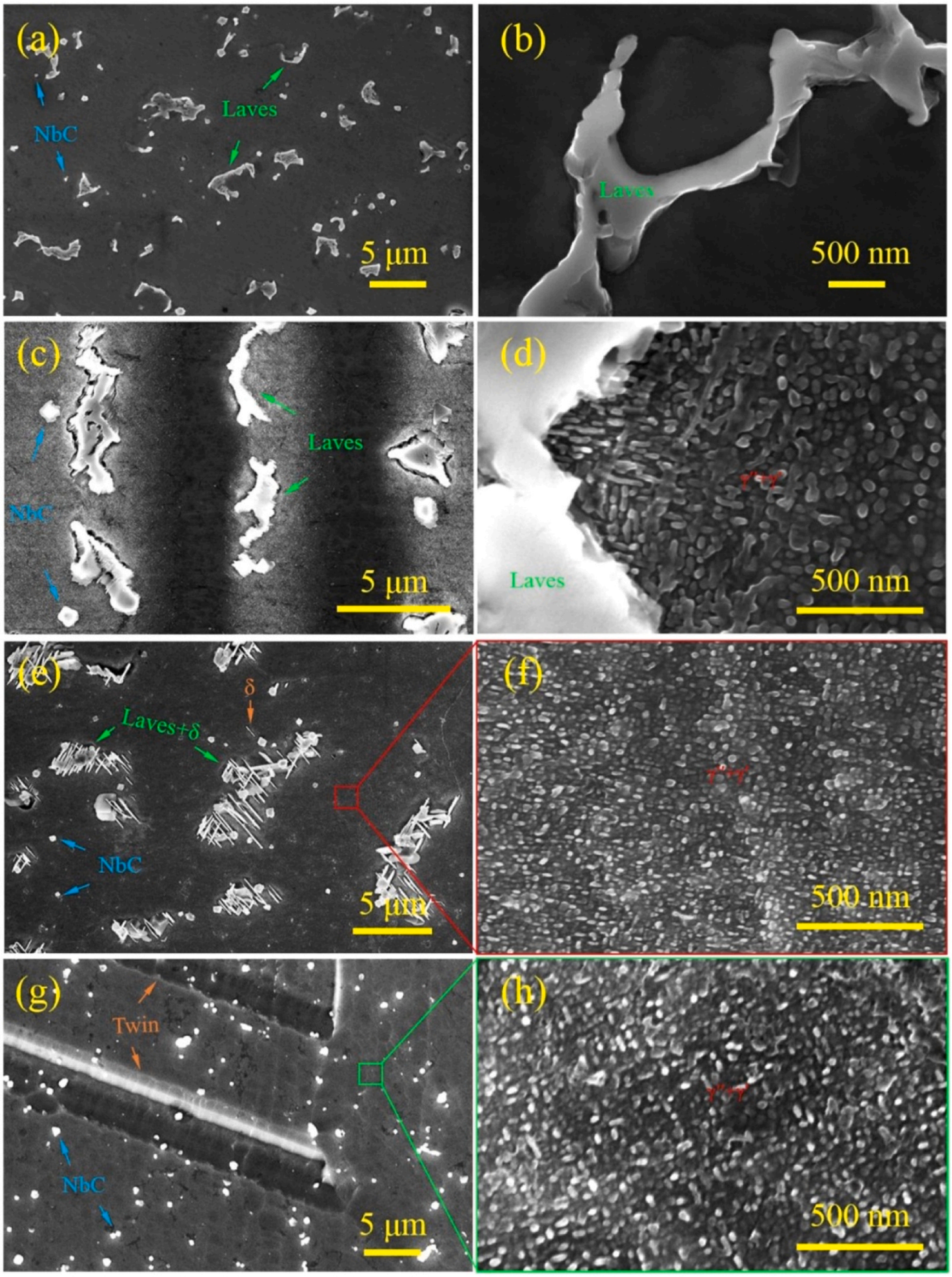

Fig. 14. SEM of DED-LB IN718 (a,b) as-deposited: interdendritic Laves eutectic with NbC, (c,d) DA: non-uniform γ'/γ'' around retained Laves, (e,f) SA: partial Laves dissolution with short acicular δ and denser γ'/γ'', (g,h) HSA: Laves largely removed, uniform γ'/γ'' in a recrystallized matrix and NbC retained [110]. (Reproduced with permission from Elsevier).

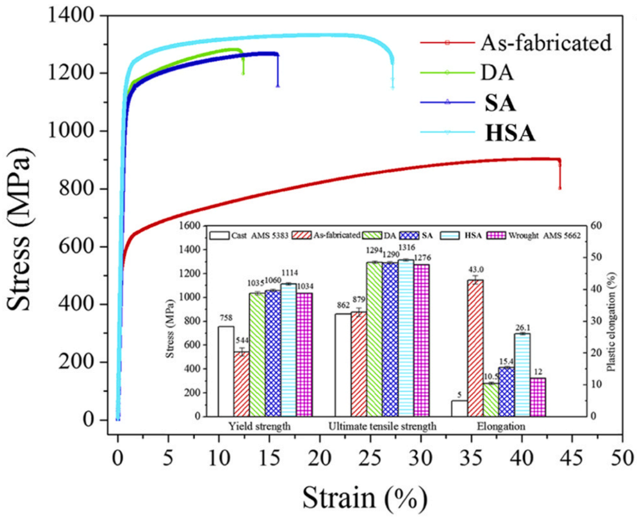

Fig. 15. Room-temperature tensile curves of DED-LB IN718 in as-fabricated, DA, SA, and HSA conditions; inset compares YS, UTS, and elongation with AMS 5383 and AMS 5662 standards [110]. (Reproduced with permission from Elsevier).

[110].

In a separate study on HSA-treated DED-LB IN718, Zhou *et al.* [112] reported a UTS of 1326 MPa with 22.5% elongation for specimens tested along the build direction, compared with 1351 MPa and 17.2% for specimens loaded along the transverse direction. As also observed for PBF-LB, post-processing heat treatment reduces build-orientation anisotropy relative to the as-built state. However, even after HSA, some ductility anisotropy can remain because heat treatment can not completely eliminate solidification texture, defects, elongated grain morphology, and the inherited layer-wise boundary networks. Consequently, the onset of damage can remain direction-dependent, with crack initiation occurring more easily when the tensile axis is unfavorably oriented relative to these microstructural features.

Table 6 shows that the plane strain fracture toughness (K_{IC}) increases progressively from the as-fabricated condition to DA, and then rises strongly after SA, and reaches the highest level after HSA. Notably, the SA-treated and HSA-treated conditions both exceed the wrought AMS 5662 benchmark. The limited change in K_{IC} after DA is consistent with aging, resulting in an increment of strength without fully removing the compositional heterogeneity and Laves phases, so crack initiation and early crack extension can still be governed by locally brittle regions and strain localization. In contrast, SA improves toughness because it reduces segregation and dissolves Laves phases, which promotes a more uniform precipitation response during subsequent aging and restores more stable crack tip plasticity. HSA further enhances this effect by more completely homogenizing the deposit and promoting recrystallization, resulting in a bimodal grain structure, which improves the crack tip strength-plasticity balance and delays unstable crack extension.

Table 6
Plane-strain fracture toughness (K_{IC}) of DED-LB IN718 in the as-fabricated condition and after post-processing [110,113].

Specimen	Fracture toughness K_{IC} (MPa·m$^{0.5}$)
As-fabricated	86.0
DA	89.8
SA	134.0
HSA	164.1
Wrought AMS 5662	96.3

3.3. Wire arc additive manufacturing

In WAAM IN718, the large melt pool and slow cooling produce millimeter-long columnar γ grains across successive layers, with clear interlayer boundaries and a distinct dendrite-core plus interdendritic-pool morphology, as shown in Fig. 16 **(a)** [56]. SEM and EDS analysis show an island-like interdendritic network of γ and Laves, along with other intermetallics such as (Ti,Nb)(C,N) and NbC/TiN (Fig. 16 **(b,c)**). The solidification length scale set by the thermal gradient and solidification rate controls Laves morphology [114]. So, WAAM results in a coarser primary spacing and a long-residence interdendritic liquid, so Nb and Mo segregate into discrete interdendritic pools that freeze as island-like Laves. In contrast, comparatively smaller melt pools and faster solidification in DED-LB shorten the primary spacing to a few micrometers and keep interdendritic liquid pathways connected at solidification, producing a continuous interdendritic eutectic [115]. In PBF-LB, the fastest cooling rates result in steep thermal gradients and rapid solidification, producing sub-micrometer cellular structures and partial solute trapping, which confines Nb and Mo to narrow cell walls where Laves appears as a fine, interconnected network along the grain boundaries [116].

The effect of different heat treatments on the microstructure of as-built WAAM IN718 specimens has been shown in Fig. 17. Standard HSA dissolves most Laves, but the 980 °C step is below the δ-solvus, so grain-boundary δ reprecipitates. Modified heat treatment, termed HA (refer to Table 4), removes Laves and suppresses δ, giving a γ matrix with only TiN/NbC. DA does not redistribute Nb, so the interdendritic Laves remains in the matrix. The orientation maps show the as-built specimen with strong columnar texture along the build direction, and after HA, a recrystallized, coarser-grain structure. The HA route is the best fit for WAAM specimens because homogenization at 1186 °C is above the δ-solvus and close to the Laves eutectic, maximizing Laves dissolution and driving Nb back into the γ matrix. It also omits the 980 °C sub-solvus step that would re-nucleate δ before aging. In WAAM, that sub-solvus step promotes δ more than in PBF-LB and DED-LB because the as-built structure has coarser segregation, a larger Laves fraction, longer time in the δ precipitation window, and more Laves interfaces that act as nucleation sites. After the modified homogenization, the double-aging step precipitates γ'/γ'' uniformly.

Fig. 18 **(a)** shows the WAAM fabricated deposit and the orientations of the tensile specimens along the build direction (BD) and the wall axis (WA). As-deposited WAAM IN718 (Fig. 18 **(b)**) shows high ductility ($\sim$ 21%) and low strength because the γ matrix is unaged, and slip is weakly impeded [117]. Island-like Laves regions act mainly as late void nucleants. Aging only forms γ'/γ'' on a segregated retained Laves, which raises strength but results in early void formation and drives elongation down to $\sim$ 2% [118]. Standard HSA removes much Laves, yet the 980 °C sub-solvus step precipitates grain-boundary δ and depletes Nb for γ''. These boundaries become easy crack-initiation sites, so strength peaks while ductility decreases ($\sim$ 0.9%). HA homogenizes above the δ-solvus and omits the 980 °C step. Laves dissolves, δ is suppressed, and double aging produces a uniform γ'/γ'' dispersion in a recrystallized matrix, giving the best balance of strength and ductility. This condition meets AMS 5383 minima for YS, UTS, and elongation, but remains below AMS 5662 in YS and UTS while meeting the elongation requirement. This shortfall is mainly due to the very coarse grains produced by high-temperature homogenization, which limit the achievable YS and UTS despite effective γ'/γ'' precipitation. Fractography after HA shows uniform deep dimples, consistent with Laves removal, δ suppression, and homogeneous precipitation [56].

Fig. 18 **(c)** compares BD and WA tensile responses for the as-deposited and HA conditions. In the as-deposited state, the direction dependence appears mainly in the UTS, which is higher in BD than in WA due to coarse columnar grains and the strong $< 100 >$ fibre texture aligned with BD, resulting in plastic flow and work hardening differences. After HA, the UTS values in BD and WA become similar, whereas

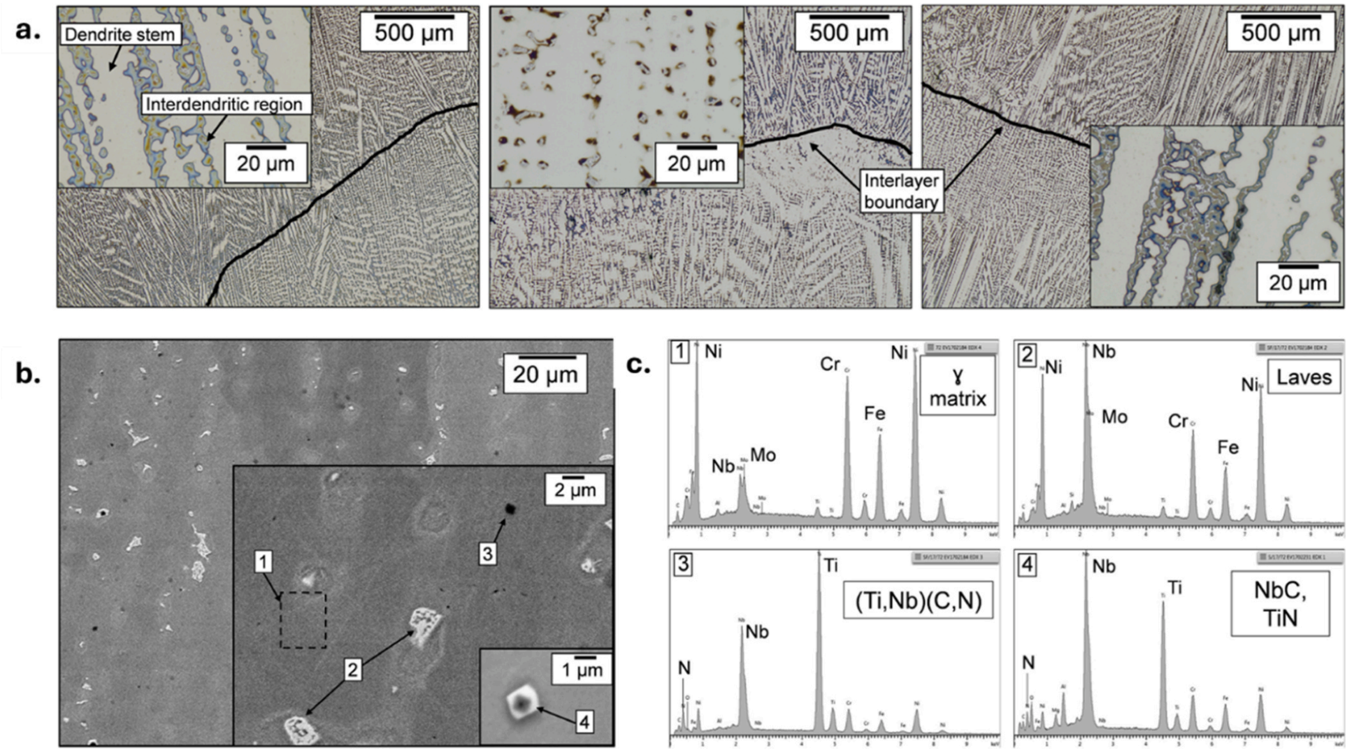

Fig. 16. WAAM IN718 as-built: (a) optical microscopic images showing columnar γ with interlayer boundary along build direction; (b,c) SEM and EDS images highlighting interdendritic network consisting of Laves and γ phase, along with carbides and nitrides phases in the matrix [56]. (Reproduced under the Creative Commons CC-BY license).

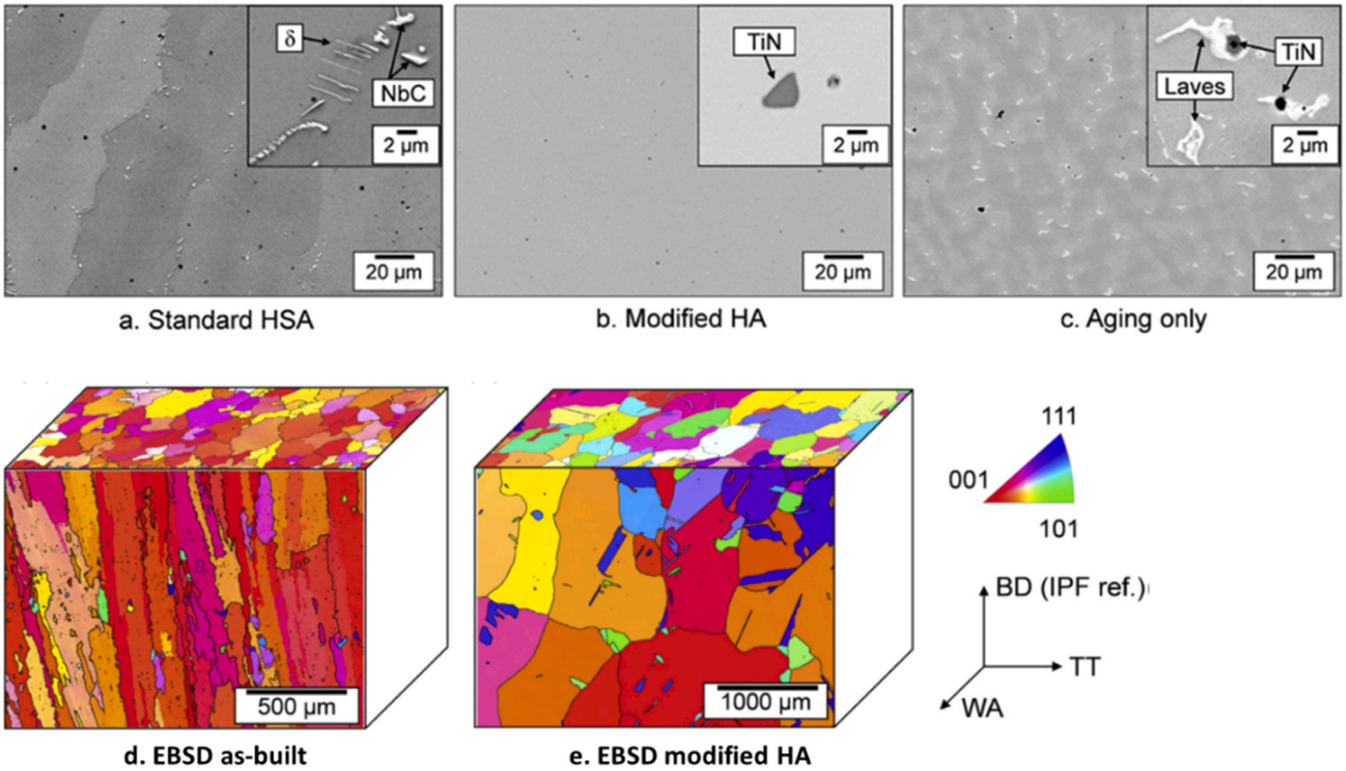

Fig. 17. SEM images of heat-treated WAAM IN718: (a) HSA with Laves dissolved, grain-boundary δ present; (b) modified HA showing Laves absent, δ suppressed, TiN/NbC retained; (c) aging-only with Laves retained; (d) EBSD inverse pole figure of as-deposited WAAM, showing strong columnar texture, and (e) after modified HA showing recrystallized grains [56]. (Reproduced under the Creative Commons CC-BY license).

a small offset remains in YS, indicating that heat treatment weakens the texture-driven anisotropy but does not fully remove microstructural

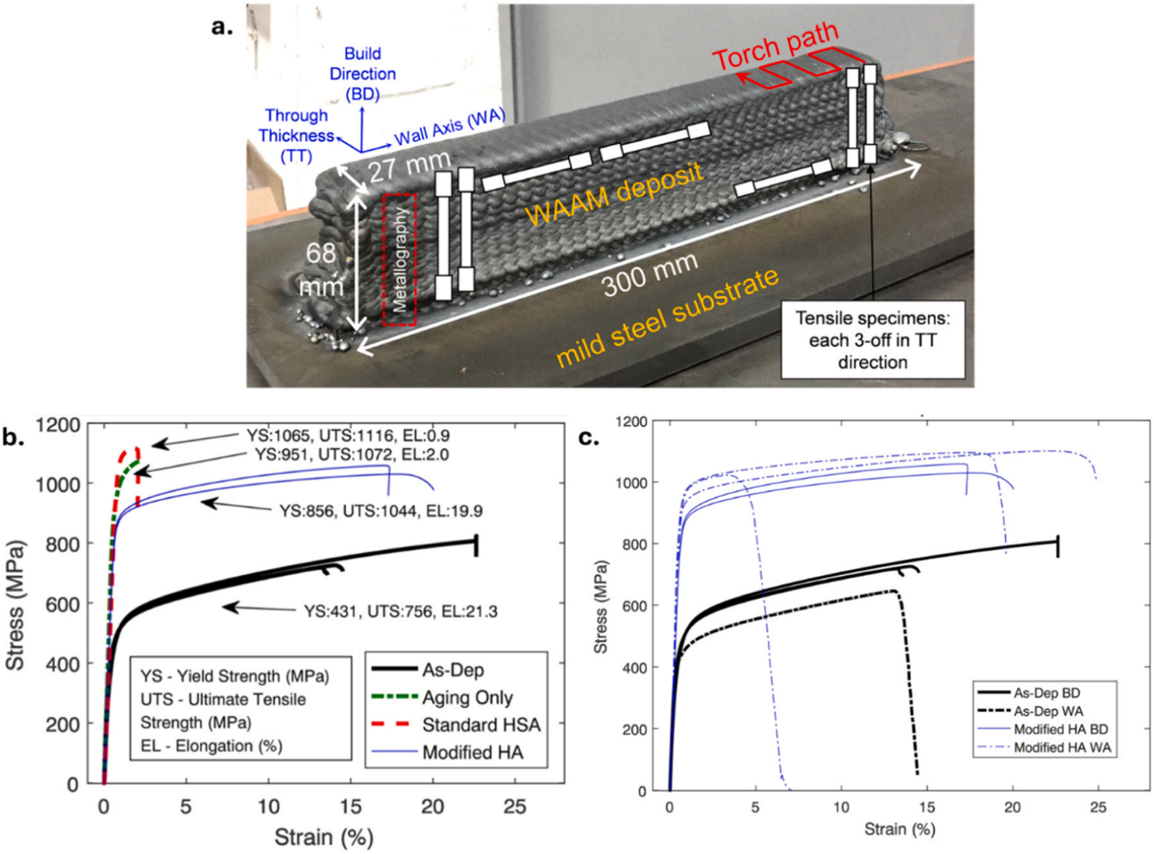

Fig. 18. (a) As-fabricated WAAM IN718 deposit highlighting the tensile specimen orientations, (b) stress-strain behavior in as-built, HSA, and HA states, and (c) effect of loading direction on the tensile response in the as-deposited and HA conditions [56]. (Reproduced under the Creative Commons CC-BY license).

directionality (e.g., non-equiaxed elliptical grain morphology and inherited build features) that can still affect yielding.

Fracture toughness of WAAM IN718 subjected to HA heat treatment was evaluated in [119] using compact-tension specimens, and the results were compared with wrought data. As shown in Fig. 19 **(a)**, samples were machined from the WAAM deposit in two notch configurations so that the crack plane was oriented either parallel or perpendicular to the build-related defect planes. The EBSD map in Fig. 19 **(b)** highlights the notch orientation relative to the build orientation and the coarse-grain structure of the HA-treated deposit. The J-Δa resistance curves in Fig. 19 **(c,d)** show a strong notch-orientation effect, with Notch ∥ (crack plane parallel to BD) giving a lower resistance curve than Notch ⊥ (crack plane perpendicular to BD). This difference arises due to crack-like defects, described as intergranular hot-crack features that create locally unbonded planar regions. These defect planes are oriented normal to the wall-axis direction, so they become coplanar with the main crack in the Notch ∥ configuration and can link with the crack front, effectively extending the crack without requiring additional tearing. In the Notch ⊥ configuration, the same defects are oriented across the crack plane, which promotes crack deflection and raises the resistance to crack advance. Therefore, the Notch ⊥ toughness is comparable to wrought data, whereas Notch ∥ remains substantially lower, demonstrating that fracture-toughness anisotropy can persist after heat treatment when crack growth interacts with directionally aligned crack-like defects.

3.4. Cold spray additive manufacturing

CSAM IN718 differs fundamentally from fusion-based AM, as gas-atomized particles are accelerated in a hot, high-pressure gas stream and impact in the solid state, so there is no melt pool or solidification texture, and the dendritic substructure of the feedstock powder is largely retained [34]. Using N_2 gas at about 950–1000 °C and 4–6 MPa drives particle velocities above the critical velocity, enabling dense deposits with strong inter-particle bonding and porosity below 0.1% when process parameters are optimized [80,120]. As shown in Fig. 20 **(a,b)**, the as-deposited sample shows pull-outs and inter-splat gaps on polished sections, and an etched microstructure with deformed splats and a preserved dendrite pattern that mirrors the feedstock, including interdendritic Nb-Mo segregation. The high-strain rate impact produces intense plastic shear at particle perimeters, severe work-hardening, and very high dislocation densities [121]. In a study by Shahana *et al.* [122], transmission Kikuchi diffraction reveals heterogeneous misorientation, dislocation-cell (subgrain-like) regions, abundant high-angle boundaries, and ultrafine dynamically recrystallized grains concentrated along particle interfaces, consistent with interfacial jetting and adiabatic-shear-assisted bonding. The net result is a bimodal grain structure with sub-micrometer recrystallized grains encircling more coarsely deformed interiors [123]. These features, such as mechanical interlocking plus metallurgical bonding, preserved powder dendrites with strain gradients and ultra-fine grain networks at splat boundaries, define the as-built state for CSAM IN718.

Heat treatment is mandatory for CSAM IN718 because the as-built deposit is heavily work-hardened and poorly bonded across splats, which limits ductility to well below 1% [77]. A high-temperature solutionizing at 1200 °C for 2 h is needed to activate diffusion across inter-splat contacts, promote neck growth, relieve the very high dislocation density, and drive recrystallization of the deformed γ matrix [79]. DA densifies interfaces but retains the deformed dendrite framework and promotes δ in interdendritic regions with a non-uniform γ'/γ'' field (Fig. 20 **(c,d)**). In contrast, solutionizing at 1200 °C for 2 h, followed by DA, produces a homogenized, recrystallized γ matrix with annealing

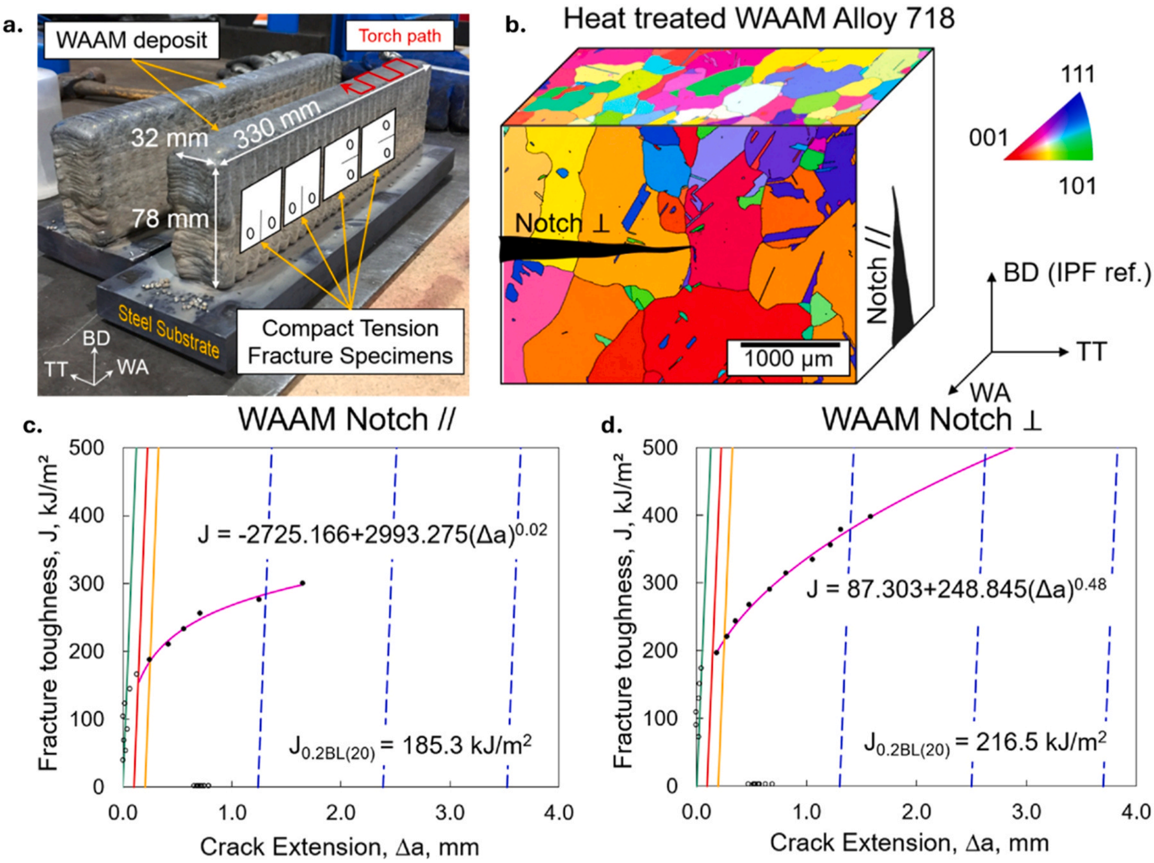

Fig. 19. Fracture-toughness anisotropy of HA-treated WAAM IN718: (a) Orientation of compact-tension specimens, (b) EBSD IPF map showing notch orientation relative to build direction, and (c,d) J–Δa resistance curves for notches parallel and perpendicular to the build direction, highlighting orientation-dependent crack-growth resistance [119]. (Reproduced under the Creative Commons CC-BY license).

twins [74]. Also, δ is suppressed, and a uniform γ'/γ'' phase precipitates (Fig. 20 **(e,f)**). The role of solutionizing in CSAM differs from fusion-based AM as it primarily enhances inter-splat interfaces bonding and removes impact-induced strain gradients rather than dissolving solidification-derived Laves and δ networks, which are the major concern in fusion-based AM.

In a study done by Karakas *et al.* [79], porosity fell from 2.49% in the as-deposited state to 2.14% after solutionizing at 968 °C, 2.02% at 1066 °C, and 1.59% at 1200 °C for 2 h. As shown in Fig. 21, after solutionizing, the tensile strength is modest, and ductility increases with solutionizing temperature, reaching ~ 16% at 1200 °C while UTS remains near ~ 800 MPa. After solutionizing followed by DA, the curves cluster at high strength with the 1200 °C heat-treated sample, giving the best results in both strength and elongation. Relative to specifications, the heat-treated CSAM meets the cast AMS 5383 minima but remains below the wrought AMS 5662 ductility range.

Su *et al.* [80] proposed a shortened post-heat treatment named HST-2h that pairs a high-temperature solutionizing at 1100 °C for 2 h with reduced aging time of 720 °C for 2 h and 620 °C for 2 h to meet AMS specifications. As shown in Fig. 22 **(a)**, EBSD shows the as-built sample contains a bimodal, ultrafine microstructure with random texture, then after HST-2h, it recrystallizes into equiaxed ~ 3 μm grains with annealing twins (Fig. 22 **(b)**), and since the grain size remains much finer than wrought material, it enables rapid γ'/γ'' precipitation during the shorter aging. The EBSD kernel average misorientation (KAM) maps further indicate high local lattice distortion in the as-built state (Fig. 22 **(c)**) that is strongly reduced after HST-2h (Fig. 22 **(d)**), consistent with recovery and recrystallization. The tensile curves (Fig. 22 **(e)**) confirm that the HST-2h condition achieves about 1085 MPa YS, 1350 MPa UTS, and ~ 15% elongation, while extending the aging to 4 h or 8 h at 720 °C and 620 °C adds strength but reduces ductility because denser precipitates limit void growth. Placing these data against prior AM studies shows HST-2h falls within the AMS 5662 wrought range (Fig. 22 **(f)**) for strength and ductility, establishing that CSAM IN718 can satisfy the standard with N_2 as the propellant and without long aging times. Upon fractography, ductile failure is displayed with deep dimples after HST-2h, with dimples becoming smaller and less numerous as aging extends, consistent with the tensile response.

Table 7 summarizes the recommended heat-treatment routes for IN718 across PBF-LB, DED-LB, WAAM, and CSAM. For each process, the as-built state, the post-treatment microstructure (Laves dissolution, δ control, and uniform γ'/γ'' precipitation in the γ matrix), and the resulting static tensile performance versus wrought AMS 5662 and cast AMS 5383 have been compiled. Regarding fulfilling the AMS criteria, it has been assumed that the as-built specimens have porosity below 0.1%. The mechanistic role of post-build heat treatment differs across the reviewed AM routes because the starting microstructures are fundamentally different. In the fusion-based routes, solutionizing and homogenization are primarily used to dissolve Laves phases and reduce Nb segregation, while controlling δ reprecipitation before ageing. As the segregation length scale and Laves phases fraction increase from PBF-LB/M to DED-LB/M and then to WAAM, progressively stronger homogenization temperature is required. In WAAM, the conventional 980 °C sub-solvus step is particularly unfavorable because it promotes grain-boundary δ reprecipitation from the coarse segregated structure. In contrast, for CSAM, the main role of high-temperature solutionizing is not the dissolution of solidification-derived Laves phase networks, but the promotion of inter-splat diffusion bonding, relaxation of impact-induced strain gradients, recrystallization of the severely deformed γ matrix, and reduction of residual porosity. Subsequent ageing then

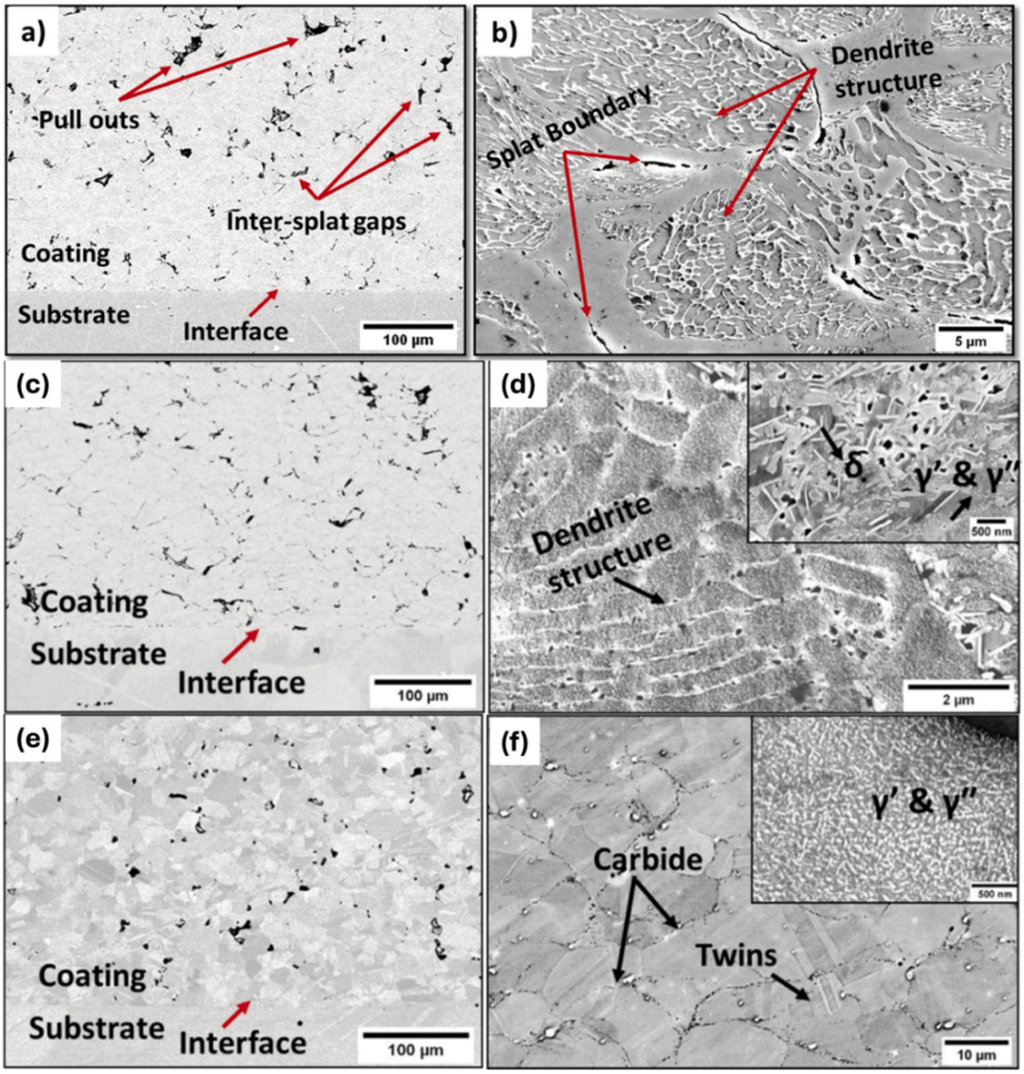

Fig. 20. CSAM IN718 microstructures in (a) as-built state with pull-outs and inter-splat gaps, (b) etched as-built revealing splat boundaries and a dendritic substructure, (c) DA giving densified inter-splat interfaces, (d) δ in interdendritic regions and γ′/γ″ in the γ matrix (inset) in DA-treated specimen, (e) solutionized at 1200 °C for 2 h then subjected to DA, yielding a homogenized γ matrix and reduced porosity, and (f) annealing twins, carbides, and a uniform γ′/γ″ precipitation in solutionized + DA-treated sample [74]. (Reproduced with permission from Springer Nature).

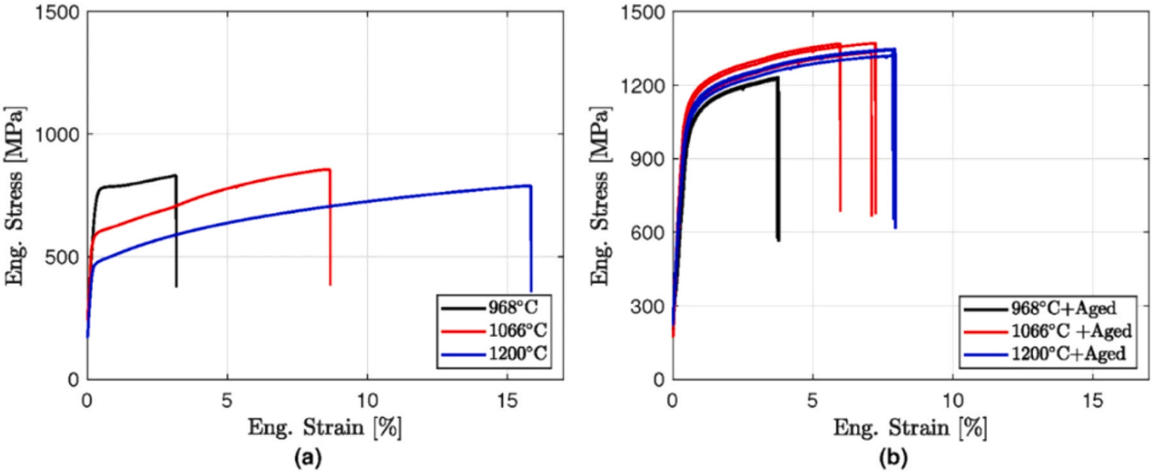

Fig. 21. CSAM IN718 stress-strain response for (a) solutionized at 968 °C, 1066 °C, and 1200 °C for 2 h without aging, and (b) solutionizing followed by double aging [79]. (Reproduced with permission from Springer Nature).

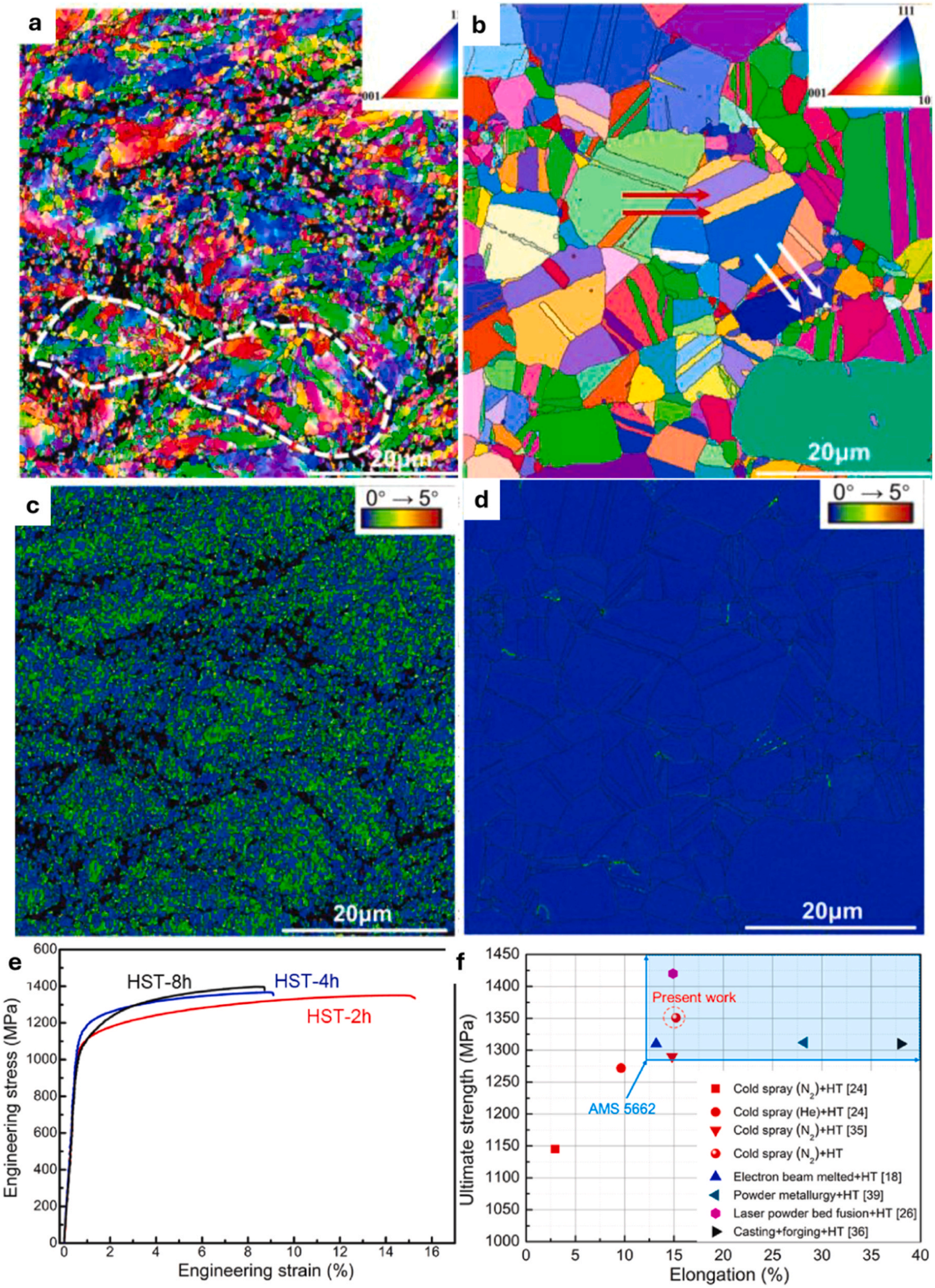

Fig. 22. CSAM IN718 with N_2 at 10 MPa: (a) EBSD IPF map in the as-deposited state, (b) IPF map after HST-2h (solutionizing at 1100 °C × 2 h + 720 °C × 2 h + 620 °C × 2 h) with equiaxed grains and annealing twins, EBSD kernel average misorientation (KAM) map in the (c) as-sprayed state and (d) after HST-2h, (e) stress-strain curves for HST-2/4/8 h, (f) UTS-elongation plot showing HST-2h within the AMS 5662 band and compared with previously reported data [80]. (Reproduced with permission from Elsevier).

Table 7
Summary of recommended heat-treatment routes for IN718 across AM processes (PBF-LB, DED-LB, WAAM, CSAM) to meet wrought AMS 5662 and cast AMS 5383 requirements.

AM route	As-built microstructure	Recommended heat treatment	Microstructure after heat treatment	Static mechanical properties post-heat treatment
PBF-LB/M	Fine cellular γ with Nb segregation; interdendritic Laves; columnar grains along build direction; high dislocation density	HSA: Homogenization ~ 1080 (1 h) → 980 °C (1 h) → 720 °C (8 h) → 620 °C (8 h)	Laves dissolved, and Nb redistributed; recrystallized/equiaxed γ; δ mainly at GBs; uniform γ'/γ''	Meets all criteria of wrought and cast standards with ≥ 12% elongation
DED-LB/M	Coarse columnar γ; interdendritic (γ+Laves) eutectic networks; strong segregation bands	HSA: Homogenization 1080 °C (1 h) → 980 °C (1 h) → 720 °C (8 h) → 620 °C (8 h)	Laves removed; δ confined to grain boundaries; recrystallized/bimodal γ and randomized texture; uniform γ'/γ'' precipitation	Meets all criteria of wrought and cast standards with ≥ 26% elongation
WAAM	Very coarse columnar γ with large dendrite spacing; Laves pools; strong texture; rough surfaces	HA: High temperature homogenization near δ-solvus (~ 1185–1190 °C, short hold for < 1 h) → 720 °C (8 h) → 620 °C (8 h)	Laves dissolution; partial recrystallization to coarser equiaxed γ; δ suppressed; uniform γ'/γ'' though coarser than PBF-LB/DED-LB	Fulfills cast AMS standard but below wrought YS & UTS requirements
CSAM	Work-hardened splat stacks; inter-splat porosity; fragmented dendrites from feedstock; near-surface compressive state	HST: High-temperature solutionizing with reduced ageing time, e.g., 1100–1200 °C (1–2 h) → 720 °C (2 h) → 620 °C (2 h)	Interfaces bonded by diffusion; recrystallized γ with twins; δ minimized; uniform γ'/γ''; porosity lowered	Meets all criteria of wrought and cast standards with 15% elongation. Post-treatment isotropy remains to be verified.

enables a more uniform precipitation of γ'/γ'' strengthening phases.

In practice, CSAM generally uses as-received powders with only basic handling steps. A common precaution is low-temperature drying (usually below about 100 °C for 1–2 h) to remove adsorbed moisture. Heat treating the powder at high temperature before spraying is not standard, because it adds cost and can also change flowability and surface condition. Sudigdo *et al.* [124] carried out the first systematic study on heat-treated IN718 powder to test whether modifying the intra-particle microstructure before CSAM can alter strain accumulation during impact and thereby improve inter-particle bonding and reduce porosity. As shown in Fig. 23 for the as-received powder, the particles retain a dendritic solidification substructure, and the initial plasticity generated on impact preferentially develops along these internal features. During particle-substrate contact and subsequent inter-particle impingement, dislocations accumulate rapidly at contact regions, and the local strain can be sufficient to form subgrains and ultrafine grains near the interface region. The EBSD-KAM map indicates a relatively broad distribution of local misorientation within the particles, showing that deformation is not confined to a very thin interfacial band. However, because the strain is not distributed uniformly along every contact, some interfaces remain

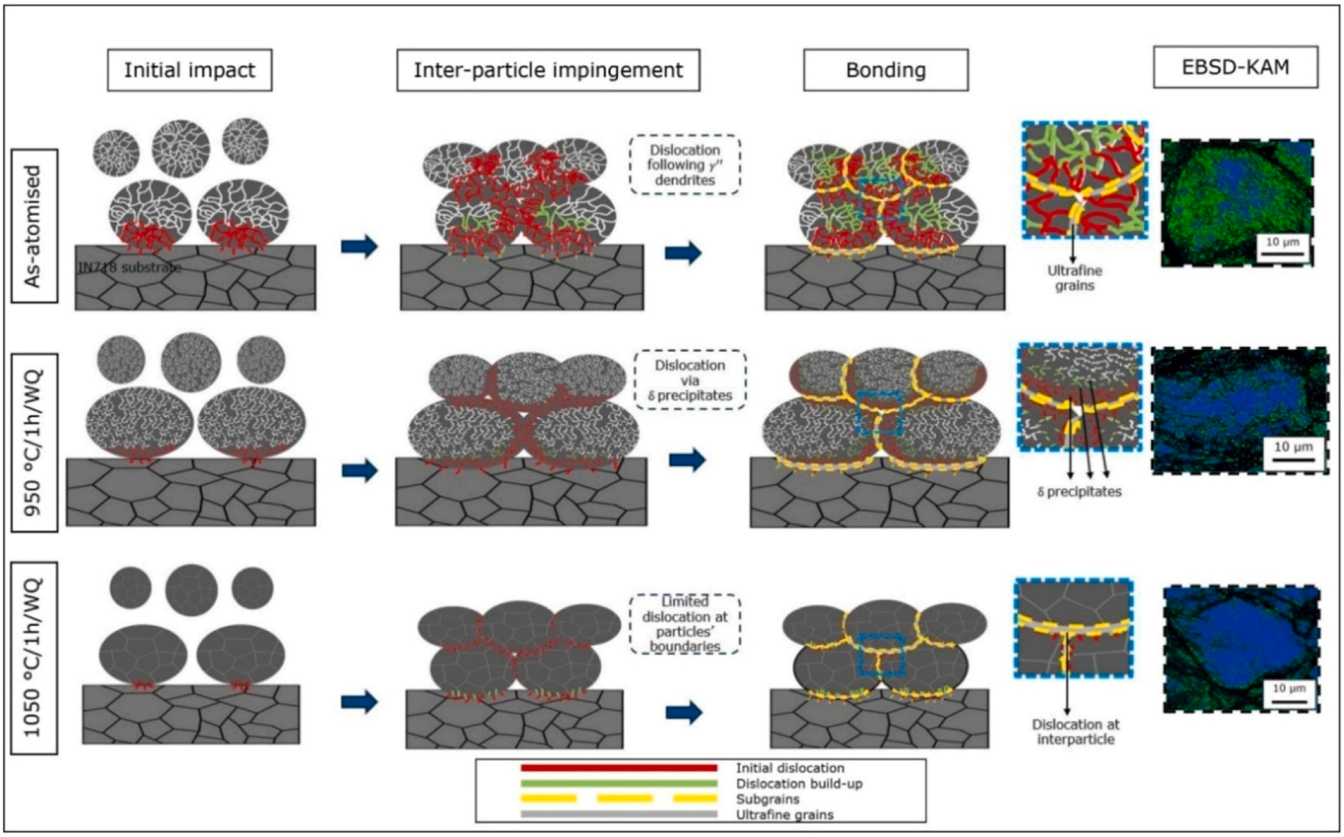

Fig. 23. Schematic explanation of the effect of pre-heat treatment of gas atomized IN718 powder on deformation and bonding during CSAM. The stages of initial impact, inter-particle impingement, and interfacial bonding are compared for as-atomized powder and for powders solution treated at 950 °C for 1 h, followed by water quenching (WQ), and at 1050 °C for 1 h, followed by WQ. The right-hand EBSD maps show KAM, where blue indicates low local lattice distortion and green indicates higher distortion, highlighting regions of strain localization after CSAM [124]. (Reproduced under the Creative Commons CC-BY license).

only partially consolidated, which contributes to retained inter-particle porosity.

For powder heat-treated at 950 °C for 1 h followed by water quenching, solutionization reduces interdendritic segregation and results in δ precipitate formation. During impact, these precipitates promote more uniformly distributed dislocation storage and a more consistent development of subgrain structure along particle-particle contacts. This results in better bonding and reduces porosity by about 50% relative to the as-received condition. At 1050 °C for 1 h followed by water quenching, the powder is fully solutionised, and the internal microstructure coarsens. In this case, limited dislocation develops within particle interiors, and plasticity is concentrated mainly near particle boundaries, which reduces the extent of interfacial grain refinement and makes bonding more sensitive to local impact. As a result, partially bonded interfaces persist more readily, and the deposit retains higher porosity than at 950 °C. Overall, powder pretreatment via solutionisation at 950 °C improves bonding by promoting more distributed deformation during impact due to δ precipitates, whereas the higher-temperature treatment at 1050 °C reduces the ability of particles to store deformation internally and therefore does not enhance the metallurgical bonding during CSAM.

Vadani *et al.* [76] quantified tensile anisotropy in CSAM IN718 by machining micro-tensile specimens along three orthogonal directions relative to the nozzle scanning path in the plane of the deposit (X and Y

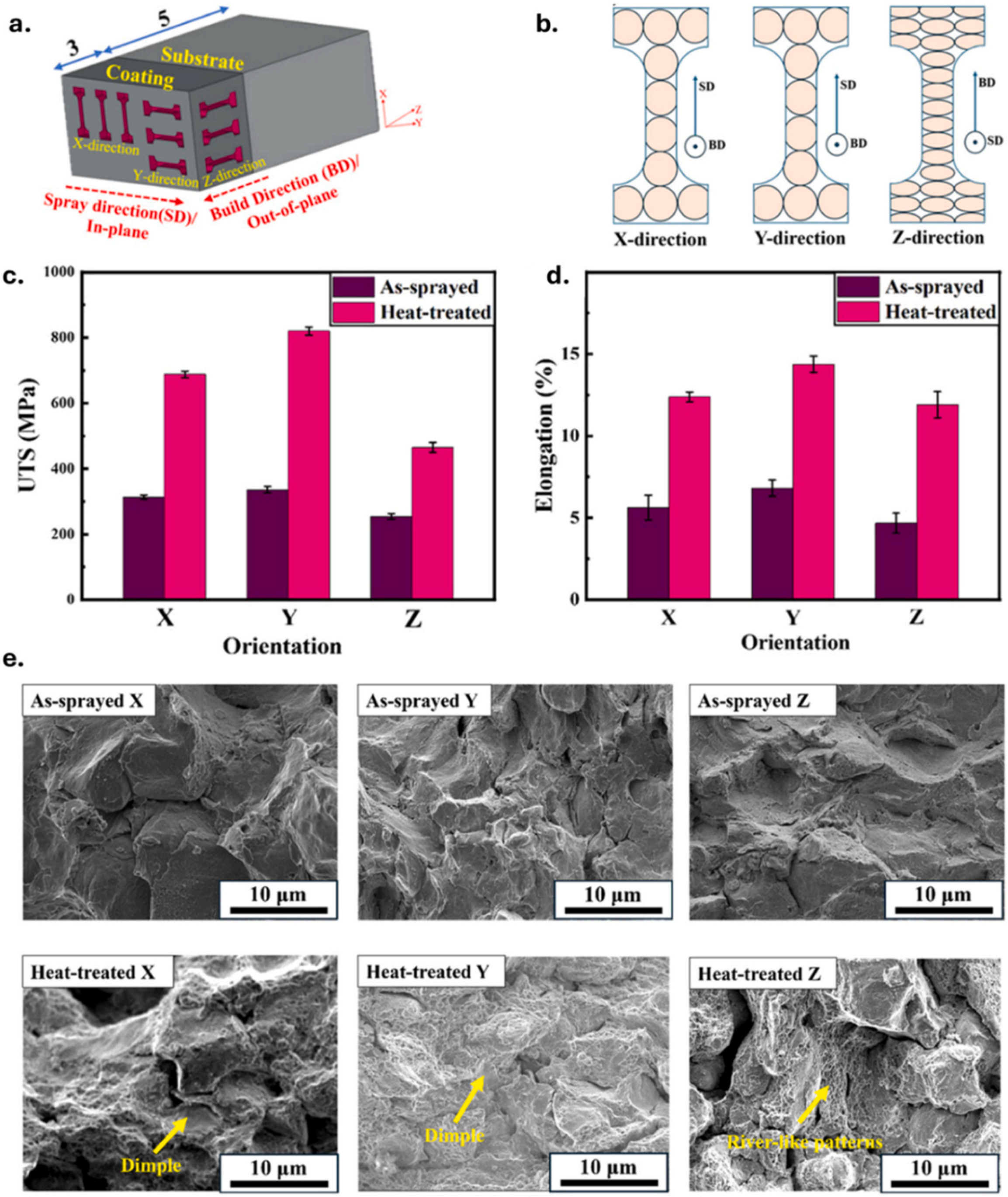

Fig. 24. (a) Schematic of CSAM IN718 deposit and specimen extraction orientations, (b) micro-tensile specimen geometries for X, Y, and Z loading directions, (c,d) UTS and elongation in the as-deposited and heat-treated states as a function of orientation, and (e) fractography of the as-built and heat-treated conditions [76]. (Reproduced with permission from John Wiley and Sons).

orientations) and the thickness build-up (Z orientation), as shown in Fig. 24 **(a,b)**. In CSAM, anisotropy originates from the layered stacking of particles that plastically deform on impact and from the alignment of particle-particle interfaces, rather than from directional solidification microstructures as in fusion-based AM. This is reflected in the tensile data in Fig. 24 **(c,d)**, where the in-plane directions show higher UTS and elongation than the Z direction in the as-built state, because Z loading more easily opens particle-particle interfaces and any interface-aligned porosity. The long-term ageing treatment (750 °C for 168 h) used in that study increases both UTS and elongation in all directions by strengthening the matrix via γ'/γ'' precipitation and improving inter-particle bonding. However, the anisotropy remains, showing that ageing alone does not remove the interface-controlled directionality that governs damage initiation under out-of-plane loading. The fractography images (Fig. 24 **(e)**) show inter-particle decohesion across orientations in the as-built state, while the heat-treated condition specimens have more ductile tearing with dimples and fewer clear interface separations, consistent with improved bonding.

From an application viewpoint, the persistence of anisotropy after ageing highlights the need to establish safe design allowables for CSAM IN718 under multi-axial loading, since an unfavorable load axis along the build direction can be limiting for aerospace components. At the same time, the available literature is limited to the previously mentioned long-term ageing condition, so further work should assess whether higher-temperature solutionizing followed by conventional or shortened ageing schedules (for example, HST-2h) can reduce interface-controlled anisotropy in CSAM IN718, similar to the way post-processing heat treatment has been used to improve isotropy in fusion-based AM.

Julien *et al.* [125] investigated fracture-toughness anisotropy in CSAM by testing machined compact-tension samples in orientations defined using the L-T-S convention, where L denotes the nozzle long-scan direction, T the nozzle pass-spacing direction, and S the robot-axis build-up direction, and the two-letter code reports the loading direction, followed by the crack-propagation direction. Using the as-built CSAM Al 6061 deposit, they found that the effect of orientation on fracture toughness is moderate, as shown in Fig. 25. The measured K_{IC} values are similar for in-plane crack growth orientations (L-T, T-L, S-T, and S-L), whereas they are slightly higher when crack growth is normal to the deposit plane (L-S and T-S). This difference is interface-controlled because crack advance is easier when the crack can follow particle interfaces, which typically contain locally weak metallurgical bonding and porosities, and it is more resistant when the crack is forced to cut across these interfaces. Additionally, the CSAM deposit exhibits poor fracture toughness compared to the wrought specimen, as particle-particle interfaces remain the dominant weak links and provide preferential paths for crack advancement [126]. This mechanism differs from fusion-based AM, where fracture toughness trends are more commonly governed by directional solidification texture and melt-pool-related heterogeneity. Moreover, for CSAM IN718, orientation-based K_{IC} datasets remain unavailable, and the influence of post-processing heat treatments is still unexplored, which currently limits damage-tolerance assessments.

Fig. 26 summarizes the tensile and fracture-toughness trends discussed in Section 3. After heat treatment, the reported tensile response of PBF-LB, DED-LB, and CSAM meets the minimum AMS requirements for wrought-aged and cast IN718, whereas the available WAAM data remain outside the wrought band. The fracture-toughness dataset is still incomplete, as K_{IC} has not yet been reported for the HSA-treated PBF-LB condition or for the HST-2h CSAM condition, even though both satisfy the AMS tensile requirements. Future studies should therefore include K_{IC} measurements for these two conditions.

4. Fatigue strength and crack-growth characteristics in additively manufactured IN718

4.1. Laser-based powder bed fusion

At room temperature, fatigue crack growth in PBF-LB IN718 is transgranular [127]. The growth rate and threshold are governed by the defects such as lack-of-fusion and gas pores, the ultrafine

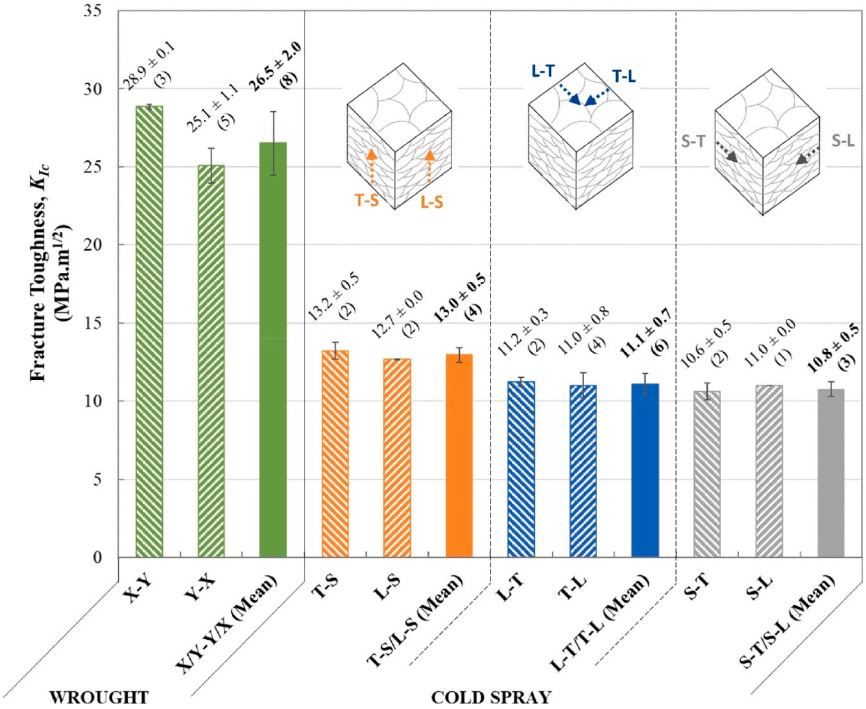

Fig. 25. Fracture-toughness anisotropy in CSAM Al 6061 compared with wrought reference material. Here, L, T, and S represent nozzle long-scan, nozzle pass spacing, and build directions, respectively. The first letter represents the loading direction, and the second gives the crack-growth direction [125]. (Reproduced with permission from Elsevier).

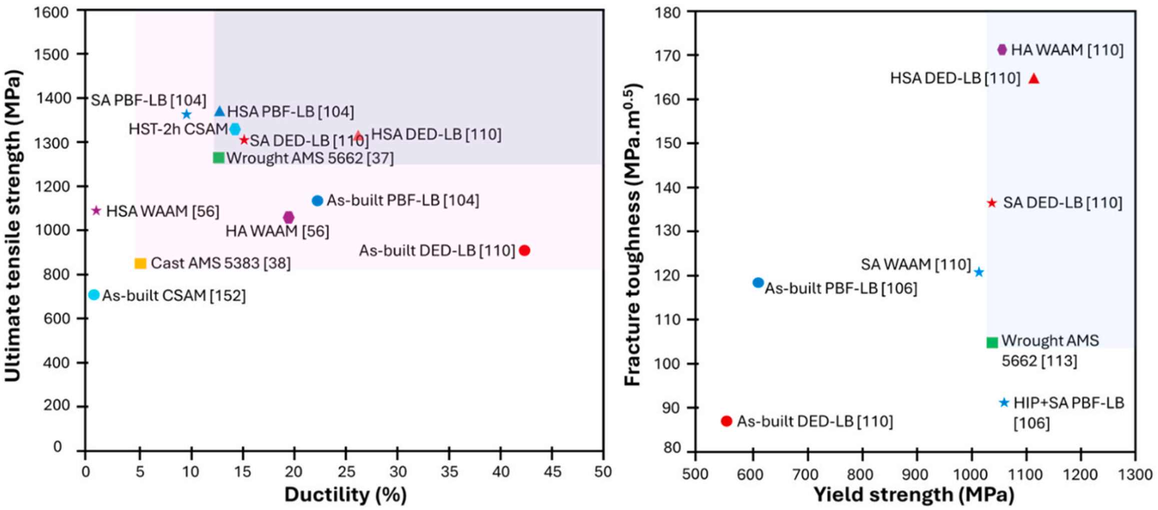

Fig. 26. Compilation of mechanical properties of additively manufactured IN718 discussed in Section 4. Shaded regions indicate the wrought AMS 5662 and cast AMS 5383 property bands.

cellular-columnar grain morphology and texture, the precipitation state (γ′/γ″ fraction and presence of δ at grain boundaries), and the tensile residual-stress field, with other test variables such as build orientation, surface finish, and load ratio also influencing [12].

As shown in Fig. 27 **(a)**, for as-built PBF-LB IN718, long-crack growth at $R = 0.1$ shows a much lower near-threshold resistance than the referenced wrought counterparts [128]. In the case of PBF-LB, $\Delta K_{th} \sim 3$ MPa·m$^{0.5}$ was calculated, whereas wrought samples have $\Delta K_{th} \sim 8$–12 MPa·m$^{0.5}$. Above about $\Delta K \sim 20$ MPa·m$^{0.5}$, in the Paris region, the curves are coincident. Similar to wrought samples, fractography is transgranular in all regimes. In the near threshold region (Fig. 27 **(b)**), the surface contains parallel secondary cracks with ~ 0.5 μm spacing and fine slip markings. These features are consistent with planar cyclic slip localizing on parallel slip planes ahead of the crack tip, which progressively damages slip bands into microcracks. The crack tip then advances by linking these microcracks [129]. In the early Paris regime, the secondary cracks lengthen and open, and at higher ΔK (Fig. 27 **(c)**), well-defined striations appear with spacing related to da/dN. The lower threshold in the as-built state is explained by tensile residual stresses that suppress crack-closure and by the directional solidification texture and aligned dendritic-columnar substructure, which promote a more planar crack path and limit roughness-induced shielding, with fine grain size giving an additional reduction [130].

Two different heat treatment routes for as-built PBF-LB parts were analyzed in [131] with variant A (stress-relief 1065 °C × 1.5 h plus SA) and variant H, which inserts HIP at 1150 °C × 4 h and 100 MPa between stress-relief and the same SA treatment. At $R = 0.1$, the da/dN vs ΔK curves for A and H are nearly identical and have a higher threshold than as-built samples, as shown in Fig. 28 **(a),** and overlap with wrought IN718 in the mid-ΔK Paris regime (Fig. 28 **(b)**). Fractography is transgranular in all cases for both A and H samples. At low ΔK (~ 15–20 MPa·m$^{0.5}$) facets consistent with crystallographic slip are observed (Fig. 28 **(c-d)**), while at higher ΔK (~ 50 MPa·m$^{0.5}$), well-defined fatigue striations (Fig. 28 **(e-f)**) appear with spacing related to the measured fatigue crack growth rate (FCGR). Relative to the as-built PBF-LB study reported by Konečná *et al.* [128], the heat treated states resolved the lower near-threshold through residual-stress relief and microstructural homogenization, while Paris-regime crack growth remained unchanged. Also, HIP does not measurably change FCGR at $R = 0.1$ beyond the effects already achieved by high-temperature stress relief followed by SA.

The build-orientation effects on near-threshold FCGR in PBF-LB IN718 after SA heat treatment and after HIP (1120 °C for 4 h at 100 MPa), followed by the SA, at $R = 0.1$, were analyzed in [130]. Fig. 29 **(a)** defines the two compact-tension orientations with Z-X specimen having the crack plane parallel to the build plane, while X-Z has the crack plane perpendicular to the build plane. As shown in Fig. 29 **(b)**, in the higher ΔK regime, the curves converge largely, but the near-threshold region exhibits a clear separation. SA shows the highest FCGR and the strongest orientation effect, with the X-Z condition being less resistant because the crack can advance more steadily along the elongated build-direction grain morphology and solidification substructure, producing a smoother fracture surface and therefore less roughness-induced crack closure. By contrast, Z-X forces the crack to cut

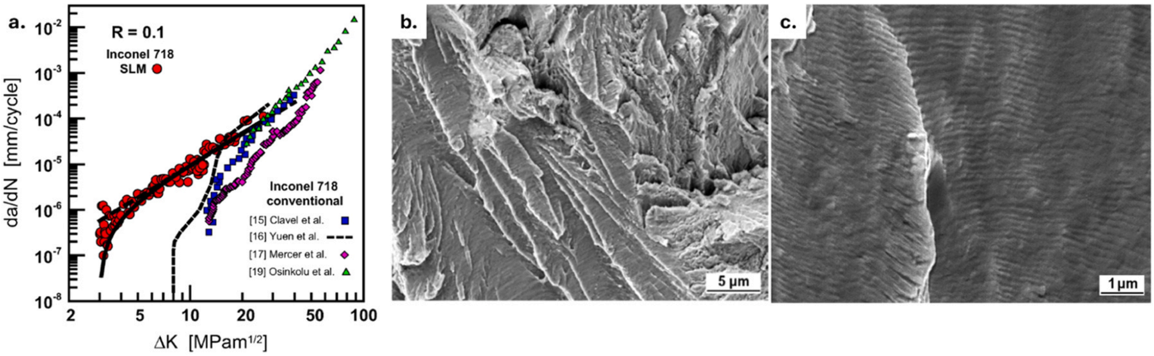

Fig. 27. (a) Fatigue crack growth rate (FCGR) of as-built PBF-LB IN718 at R = 0.1 as compared to wrought references, fracture surfaces (b) near threshold, and (c) at higher ΔK in the Paris regime [128]. (Reproduced with permission from Elsevier).

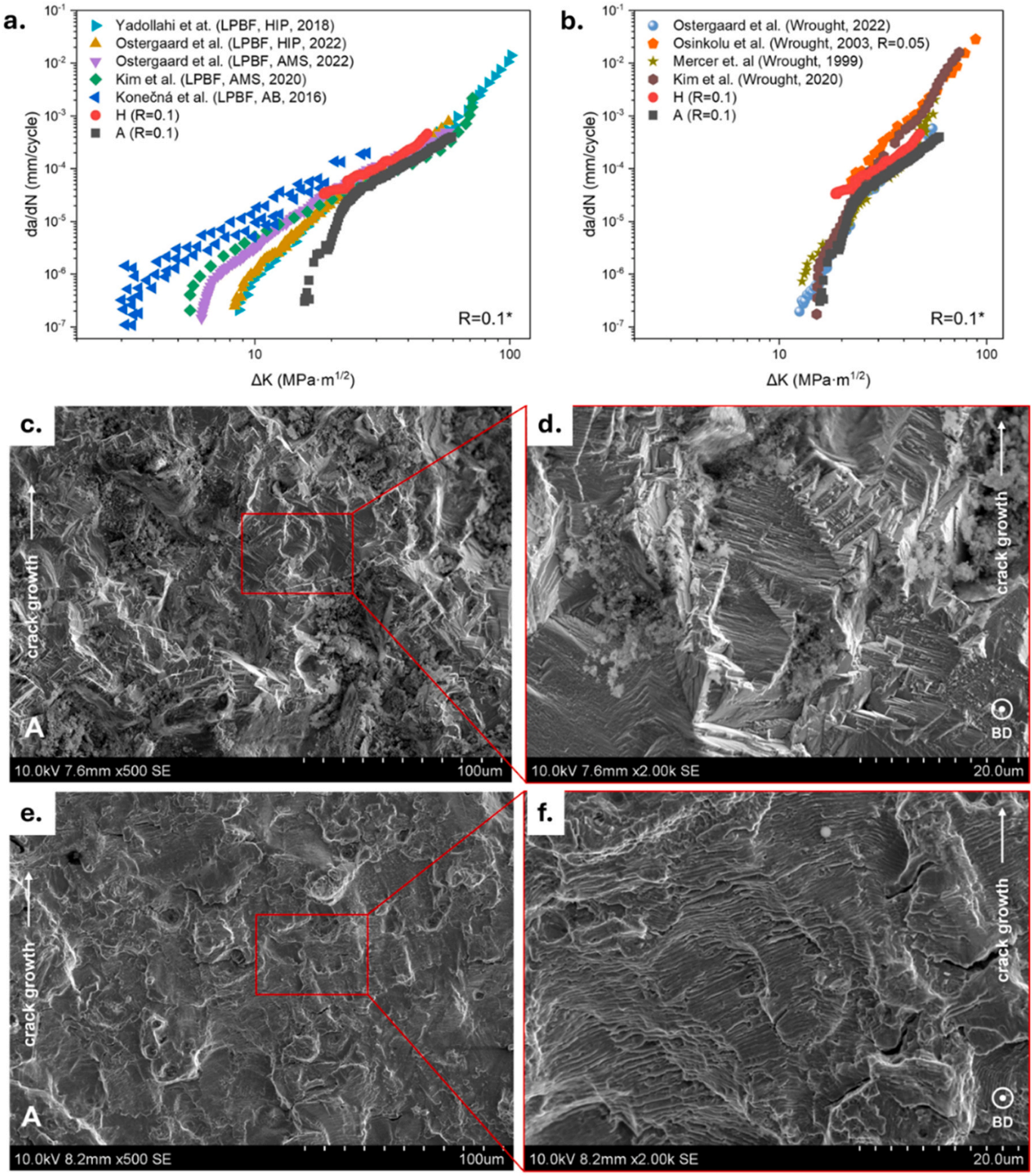

Fig. 28. (a,b) Comparison of FCGR at R = 0.1 of PBF-LB IN718 after two heat treatments: A = stress-relief 1065 °C 1.5 h, followed by SA, H = HIP 1150 °C 4 h at 100 MPa, followed by the same A heat treatment; fractography images of A specimens showing (c,d) facets near threshold and (e-f) striations at higher ΔK [131]. (Reproduced under the Creative Commons CC-BY license).

across the columnar morphology more frequently, which increases deflection and promotes roughness closure, resulting in a higher apparent threshold. HIP + SA increases the near-threshold resistance and removes the orientation dependence because during the HIPing stage, lack-of-fusion pores are closed and residual stresses are relaxed, while recrystallization weakens the build-direction texture, and the δ network reported for SA-treated specimens is not retained. With fewer aligned weak links and a less guided crack path, both orientations after HIP + SA show similar near-threshold behavior. However, even after HIP + SA, the near-threshold resistance remains lower than the wrought counterpart, which is consistent with wrought IN718 providing stronger crack-path shielding and crack-surface contact during unloading and therefore a higher apparent threshold at the same R ratio.

Fatigue strength is controlled by the most severe stress-raiser that triggers a crack and by its very early growth. In the as-built PBF-LB, this is usually the surface, where roughness and near-surface defects elevate local stresses and trigger crack initiation [132].

Fig. 30 **(a,b)** shows the build-orientation dependence of SA-treated PBF-LB IN718 on the high-cycle fatigue life (HCF). The unnotched S-N curves at $R = 0$ shift with specimen build orientation, with Type C giving the highest fatigue strength and Type A the lowest. Since the bulk microstructure is comparable after heat treatment, the differences in fatigue lives can be explained by orientation-dependent surface conditions in PBF-LB, relative to the build direction, including stair-stepping, partially fused particles, and local contour or hatch features, leading to variation in the features of the surface subjected to the fatigue test [133]. Fig. 30 **(c)** explains the effect of surface roughness of as-built samples on fatigue strength. For Renishaw AM250, the higher

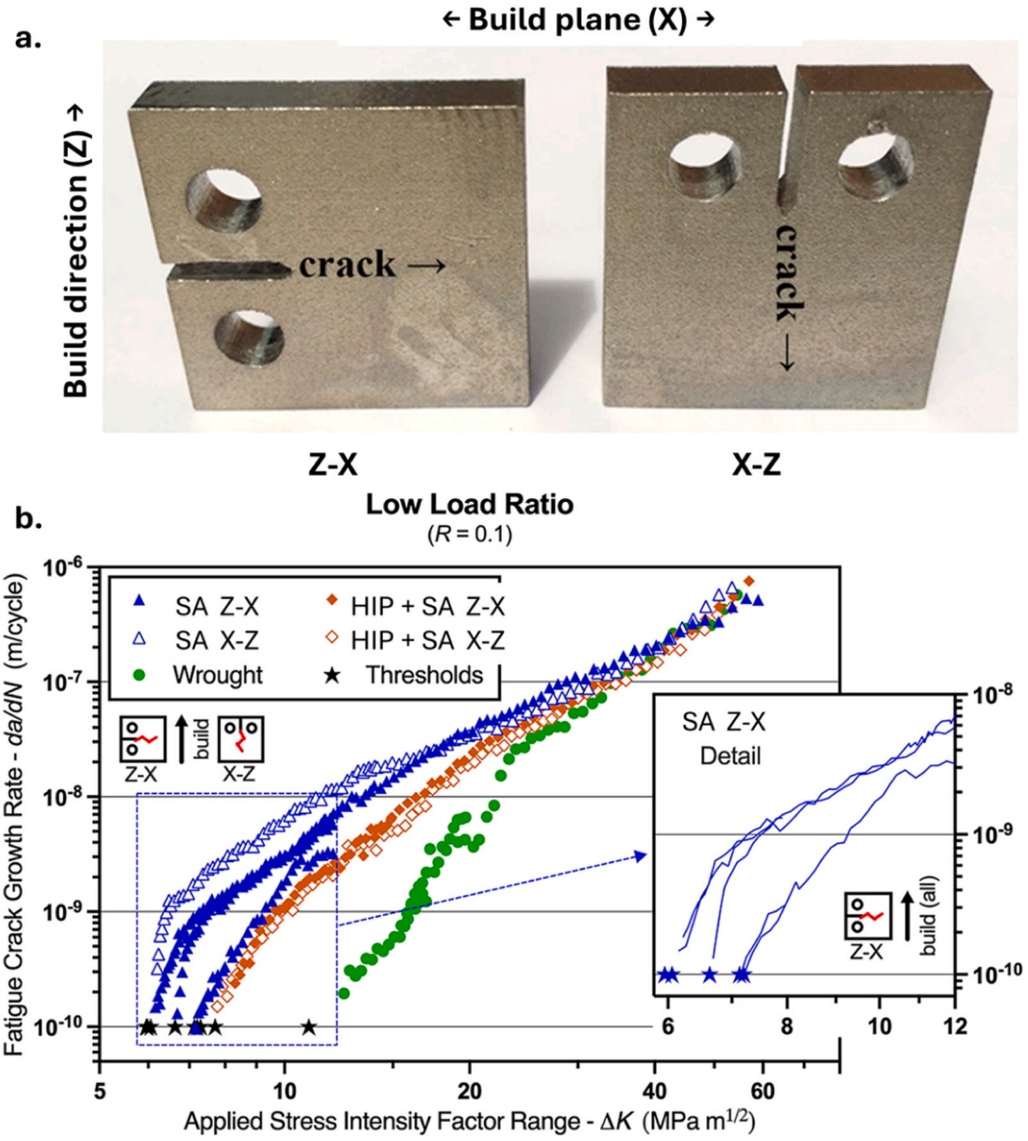

Fig. 29. (a) Compact-tension specimen orientations (Z-X and X-Z) for PBF-LB IN718 relative to the build direction (Z) and build plane (X). (b) FCGR curves at R= 0.1 comparing SA and HIP + SA treated specimens, with wrought IN718 as a reference [130]. (Reproduced with permission from Elsevier).

roughness levels (R_a = 10.67 μm for Type B; 15.56 μm for Type C) coincide with lower fatigue strengths than for SLM 280HL, where the surfaces are much smoother (R_a = 4.41 μm for Type B; 4.10 μm for Type C). In this as-built condition, surface roughness is therefore a decisive variable for the fatigue strength [134]. Fig. 30 **(d)** highlights the effect of machining on fatigue behavior. Machining shifts the controlling surface initiation sites from roughness valleys and near-surface flaws to near-surface or internal pores, which generally increases high-cycle fatigue life by reducing the dominant surface stress concentration. [135] At lower applied stresses, however, life and scatter can still be governed by the exposed subsurface defect population and the residual-stress state [136,137]. Defect size and location remain the primary sources of scatter, and a uniform dispersion of γ'/γ'' improves fatigue resistance, while δ at grain boundaries or retained Laves increases notch sensitivity [138,139].

Fig. 31 **(a)** compares the effect of heat treatment on the HCF of PBF-LB IN718 [140]. Three heat treatment routes are compared, including SA, HA, and HSA (refer to Table 4). The S-N data show the as-built state with the lowest fatigue strength, SA and HSA raising the strength by roughly one-third, and HA giving an additional rise of about ten percent over SA and HSA. The mechanism controlling the fatigue strength is captured by the fracture-strength versus brittle-phase width map, shown in Fig. 31 **(b)**. SA retains Laves with a mean width near 149 nm, HSA forms δ needles near 70 nm, and HA refines δ to about 30 nm. According to the carbide fracture model, the stress amplitude is inversely proportional to the square root of the width of undesired phases [141]. Therefore, the finest δ in HA gives the highest resistance to void-assisted cracking, while a coarse Laves network in SA is most detrimental. The as-built samples have a continuous network of Laves phase in the interdendritic region, resulting in poor fatigue resistance. Fractography shows transgranular facets and striations and confirms void-origin failure in all conditions, with pores acting as initiation sites (Fig. 31 **(c-f)**). Local cracking of Laves was observed near the void in SA at ~ 270 MPa (Fig. 31 **(g)**), and acicular δ intersected and pinned slip bands in HA and HSA at ~ 360 MPa (Fig. 31 **(h-j)**). So, the improvement in fatigue strength in the case of HA samples results from dissolution of Laves, uniform γ'/γ'' strengthening, and formation of ultrafine non-shearable δ that is less prone to fracture and reduces microcrack nucleation and linkage from nearby pores.

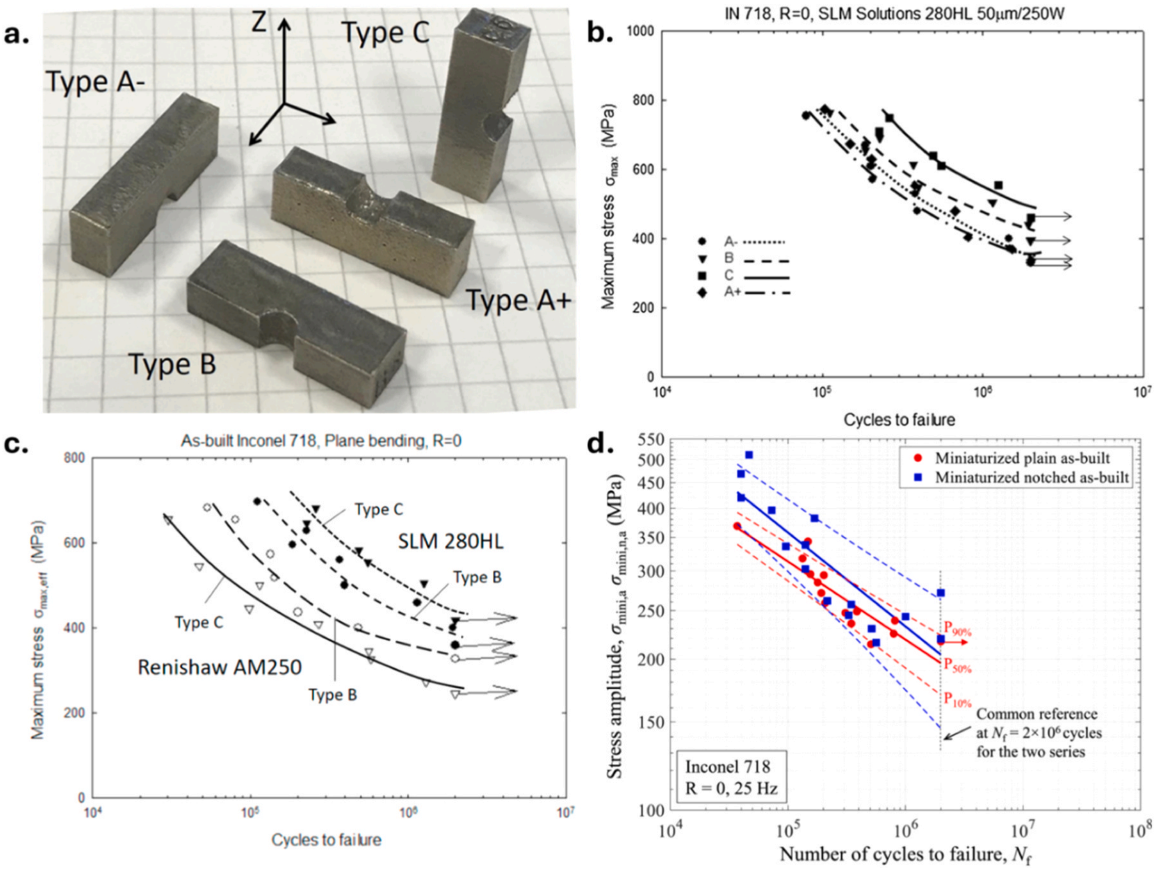

Fig. 30. (a) Miniature fatigue specimen geometries and build orientations relative to the build direction (Z) (Reproduced with permission from Elsevier), (b) unnotched S-N curves at R= 0 for SA-treated PBF-LB IN718 samples [133] (Reproduced with permission from Elsevier), (c) S-N curves of as-built IN718 samples manufactured from Renishaw AM250 and SLM 280HL, highlighting the influence of surface roughness differences on fatigue strength [134] (Reproduced with permission from Elsevier), (d) effect of machining on the fatigue response of as-built PBF-LB IN718 samples [135]. (Reproduced under the Creative Commons CC-BY license).

4.2. Laser-based directed energy deposition

Yu *et al.* [142] conducted a systematic study of FCGR in DED-LB IN718 across as-built, DA, SA, and HSA states at $R = 0.1$. As shown in Fig. 32 **(a)**, the near-threshold values are 3 MPa·m$^{0.5}$ for as-deposited, 3.5 MPa·m$^{0.5}$ for DA, 5 MPa·m$^{0.5}$ for SA, and 10.8 MPa·m$^{0.5}$ for HSA. The HSA threshold reaches the wrought band of about 8–12 MPa·m$^{0.5}$, and the Paris-regime curves of SA and HSA align with wrought IN718 in the mid-ΔK range. In the as-deposited state (Fig. 32 **(b)**), continuous Laves at interdendritic regions crack and debond under cyclic slip, and since there is no precipitate-hardened matrix, it provides a straight path, giving the lowest ΔK_{th}. DA precipitates γ'/γ'' mainly around Nb-rich Laves rather than uniformly through the matrix, so strength mismatch and interfacial stress concentrate at cracked Laves and at voided interfaces. The path remains relatively straight with secondary cracking (Fig. 32 **(c)**) and only a small rise in ΔK_{th}. SA dissolves much of the Laves and precipitates a finer, more even γ'/γ'' dispersion in the matrix together with short acicular δ around Laves sites. The crack now deflects and bifurcates along dense slip bands (Fig. 32 **(d)**) and around δ, which may lie perpendicular to the crack path, resulting in increased ΔK_{th}. HSA removes Laves segregation, redistributes Nb, and produces a uniform fine γ'/γ'' precipitate in a recrystallized matrix with δ largely confined to grain boundaries. The crack path shows frequent branching and local debonding (Fig. 32 **(e)**), giving higher roughness-induced shielding and a threshold that reaches the wrought band [143].

Fractography images in Fig. 33 show transgranular crack propagation in all samples at $\Delta K = 53.5$ MPa·m$^{0.5}$. The as-deposited specimen has wide striations near 1.12 μm per cycle with frequent tearing ridges and secondary cracks, indicating higher FCGR. DA remains rough with many secondary cracks and striations around 0.64 μm per cycle, so growth slows but is still elevated. After SA, the path becomes more tortuous with pores and fine secondary microcracks, and the striation spacing drops to about 0.35 μm per cycle. The HSA condition shows the finest, most uniform striations near 0.27 μm per cycle with frequent deflection at twin boundaries, consistent with the slowest growth at a given ΔK.

Fig. 34 **(a)** shows the room-temperature fatigue response of HSA-treated DED-LB IN718 when subjected to fully reversed loading [144]. The S-N curve gives a fatigue limit near 385 MPa at 10^7 cycles, lower than wrought references (~ 500 MPa) [145,146]. The lower fatigue resistance is attributed to the bimodal grain structure retained after HSA, comprising coarse grains and annealing twins that favor surface-slip initiation, as well as small pores that serve as microvoid nuclei. Fractography confirms a surface-initiated, transgranular crack propagation mechanism. At 400 MPa (Fig. 34 **(b,c)**), the fracture surface shows a clear fatigue crack initiation zone at the specimen surface, followed by an extended propagation zone and a final rupture zone. The initiation region contains slip-related features and occasional small micropores, consistent with surface or near-surface crack initiation. Across the propagation zone, the surface exhibits fatigue crack advance markings and local secondary cracking, while the final zone is dominated by ductile microvoid coalescence. Similar zone partitioning is observed at 500 MPa (Fig. 34 **(d,e)**) and 700 MPa (Fig. 34 **(f,g)**), with surface-controlled initiation and ductile final rupture in all cases.

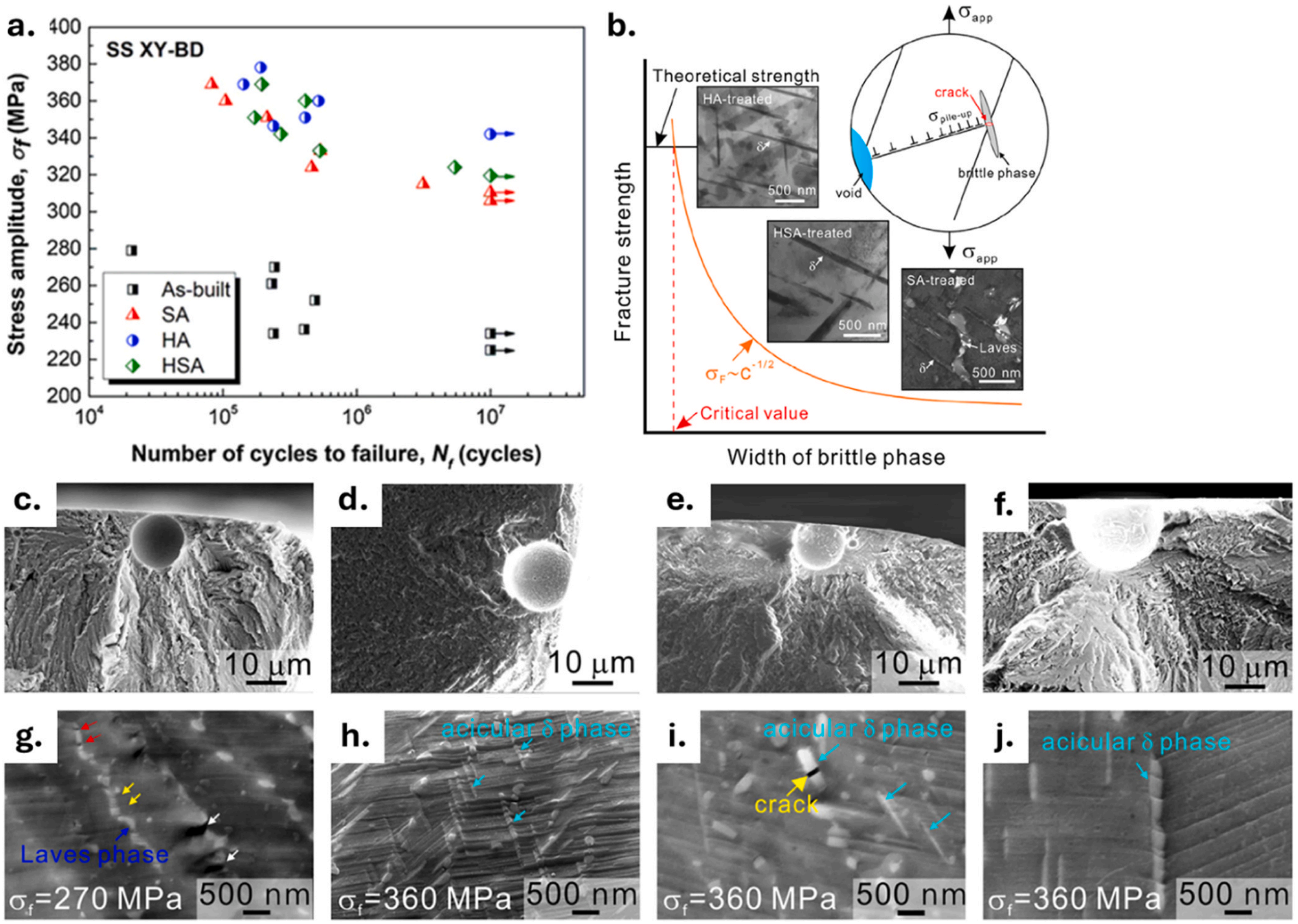

Fig. 31. (a) S-N curves for as-built, SA, HA, and HSA-treated PBF-LB IN718, (b) curve showing the relationship between fracture strength vs brittle-phase width with coarse Laves most harmful, finer δ in HSA, and ultrafine δ in HA less detrimental, (c-f) crack initiation at pores for as-built, SA, HA, and HSA, respectively, (g-j) Side surfaces near the origin for as-built, SA, HA, HSA respectively, with cracked Laves in as-built and acicular δ in SA, HA, and HAS [140]. (Reproduced with permission from John Wiley and Sons).

4.3. Wire arc additive manufacturing

In as-built WAAM IN718, FCGR is anisotropic because the crack interacts with millimeter-scale columnar grains, interdendritic Nb-rich regions, and a directional residual-stress field [117]. As shown in Fig. 35, FCGR curves at $R = 0.5$ show slightly faster growth when the crack path is aligned with the WD and slightly slower when aligned with the build direction BD. Fractography confirms transgranular growth with striations, with WD surfaces showing more secondary micro-cracks and a smoother overall path, whereas BD contains greater roughness and local deflection. The directional response is attributed to columnar texture and the alignment of interdendritic features with the deposition direction, while no changes in crack growth mechanism are observed. However, unlike PBF-LB and DED-LB, systematic FCGR datasets and in-depth evaluation of specimens subjected to heat treatment are still unavailable for WAAM IN718.

The S-N curves for fatigue strength evaluation of as-built WAAM samples also exhibit anisotropy (Fig. 36 **(a)**). Specimens aligned along WD achieve longer lives at a given stress range, while BD fails earlier due to easier surface-slip initiation along elongated grains and occasional lack-of-fusion defects. Fractography (Fig. 36 **(b)**) shows surface or near-surface initiation, striation-controlled propagation across the section, and a ductile final rupture by microvoid coalescence. Similar to FCGR, there is no literature available on the effect of post-heat treatment on the fatigue strength of WAAM specimens.

4.4. Cold spray additive manufacturing

CSAM deposits have a deformed splat stacking with inter-particle and inter-layer interfaces that control crack growth, so the FCGR is governed by orientation relative to the particle [33]. In FCGR studies of CSAM, L, T, and S denote the scan, transverse (pass-to-pass), and build directions, respectively; specimen orientations are reported using a two-letter code in which the first letter gives the specimen long axis and the second gives the crack-growth direction. In the case of CSAM Al-6061, in-plane crack growth shows little difference between orientations within the deposition plane [147]. For CSAM pure iron, the two in-plane orientations (L-T and T-L) are similarly close, whereas crack growth along the build direction (L-S and T-S) is more resistant near threshold (lower da/dN and higher threshold) because the crack is forced to cut through the stacked, plastically deformed particles rather than advancing along interface-aligned boundaries and porosity; with higher driving force, fracture transitions toward more interface-assisted growth via particle decohesion, and the orientation dependence correspondingly diminishes [148]. This behaviour is consistent with broader observations in freestanding deposits, where cracks that grow perpendicular to the BD (S-L/S-T) can more readily follow weak inter-particle boundaries, whereas cracks that grow parallel to BD (L-S/T-S) must repeatedly cut across splats and interfaces, increasing crack deflection and resistance [149].

For freestanding CSAM 316 L (Fig. 37), the as-built deposit shows

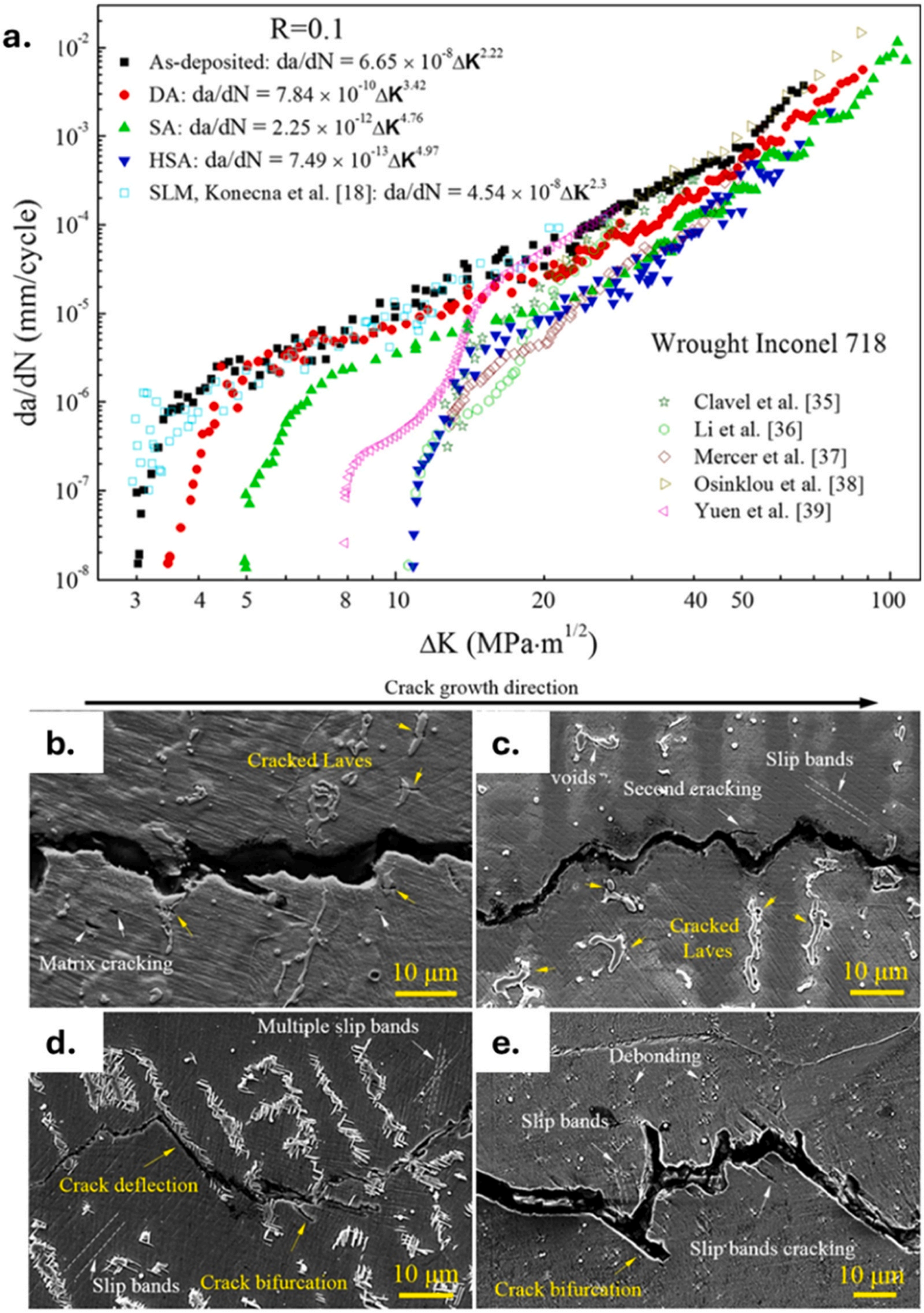

Fig. 32. (a) FCGR of DED-LB IN718 at R = 0.1 in as-deposited, DA, SA, and HSA with wrought references; crack path images near the threshold region for (b) as-deposited state showing straight path with cracked Laves, (c) DA with cracked Laves with void-assisted secondary cracking, (d) SA with crack deflection and bifurcation along with presence of acicular delta phase, and (e) HSA having tortuous path with frequent branching and interfacial debonding [142]. (Reproduced with permission from Elsevier).

clear anisotropy in FCGR. The crack grows more slowly and shows a higher threshold when it propagates in the L-S orientation because it repeatedly intersects interfaces created by particle flattening [150]. The crack grows faster when it propagates in the L-T orientation since it can more easily follow those weakly bonded interfacial regions. After annealing for 1 h at 1000 °C, the anisotropy effect was reduced, and FCGR in both orientations converged toward the cold-rolled sheet reference, indicating that annealing reduces interface-controlled cracking by improving inter-particle bonding through diffusion and partial recrystallization, so crack growth becomes more governed by the matrix rather than by weak interfaces. The fracture appearance follows the same trend, shifting from interface decohesion in the as-built condition to a more ductile, transparticle fracture mode after annealing in the higher ΔK regime. Similar behavior has been reported in other CSAM metals, where post-heat treatment reduces interface-driven crack paths and promotes a more matrix-controlled crack growth response

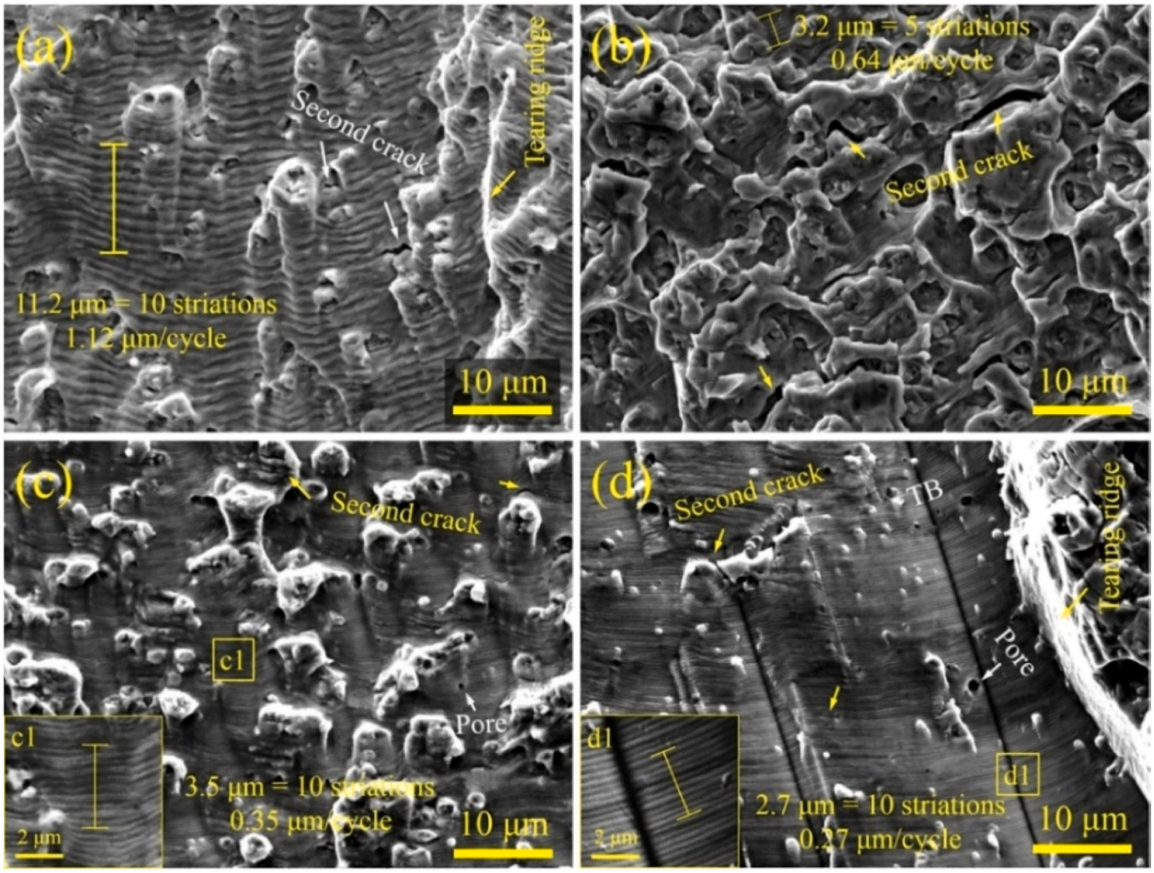

Fig. 33. SEM fractographs of DED-LB IN718 in high Paris regime for (a) as-deposited, (b) DA, (c) SA, and (d) HAS [142]. (Reproduced with permission from Elsevier).

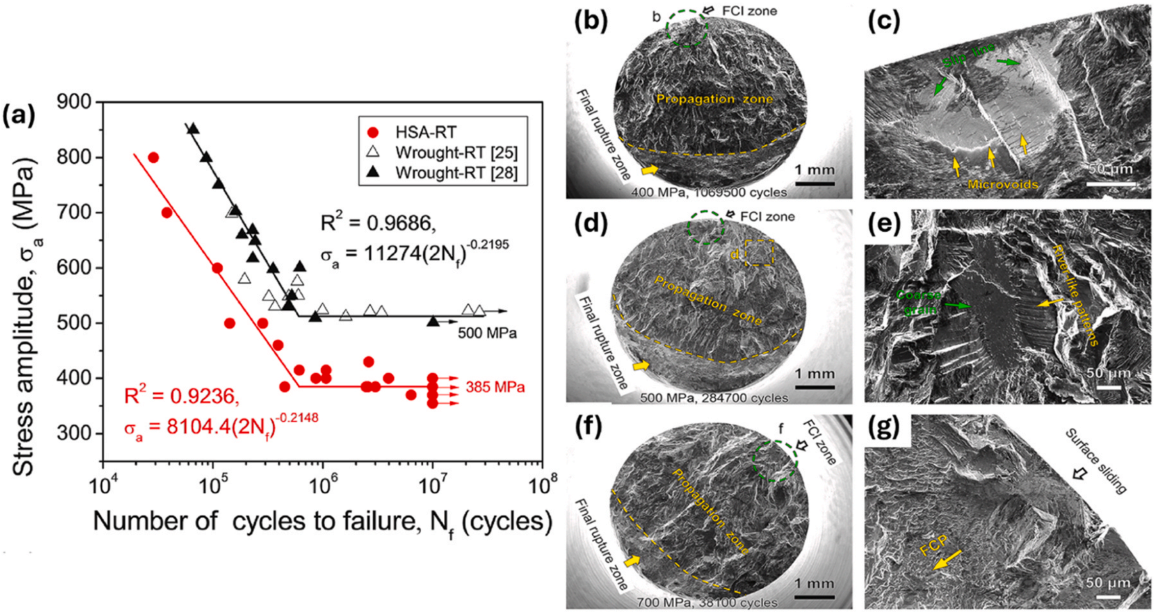

Fig. 34. (a) Room-temperature (RT) fatigue limit of HSA-treated DED-LB IN718 as compared to wrought data; SEM fractography images marking initiation, propagation, and final rupture at (b,c) 400, (d,e) 500, and (f,g) 700 MPa [144]. (Reproduced with permission from Elsevier).

[151].

For IN718 specifically, to the authors' knowledge, no FCGR dataset has yet been reported for freestanding CSAM specimens, and the effects of heat treatment on crack growth have not been systematically studied. Orientation-based FCGR data are also unavailable, so the magnitude of as-built anisotropy and the extent to which post-processing heat treatment could reduce it remain unknown for CSAM IN718. As a result, direct benchmarking against wrought IN718 in FCGR is not currently

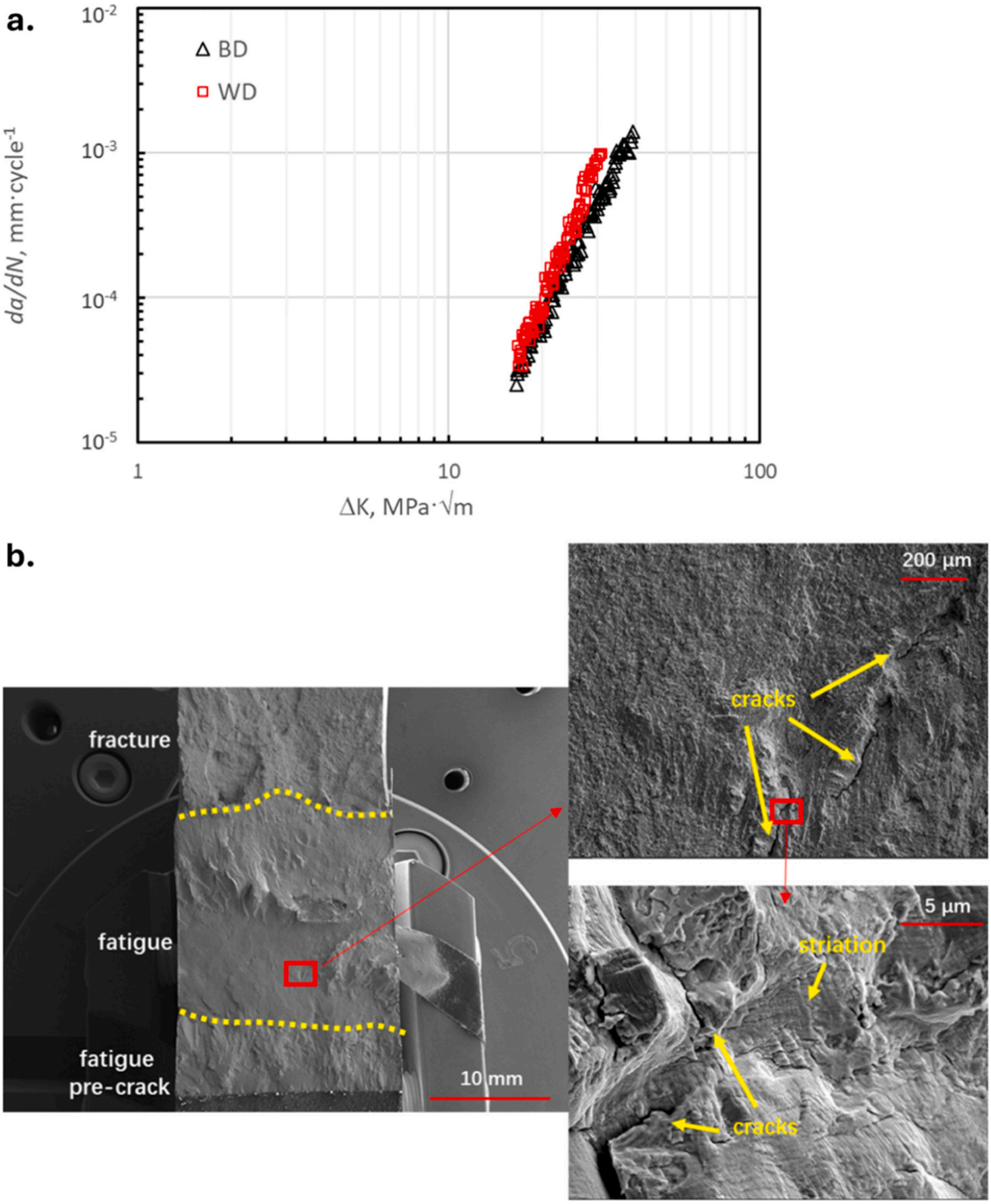

Fig. 35. (a) FCGR of as-built WAAM IN718 at R = 0.5 for samples with crack propagation direction along the build direction (BD) and wall direction (WD), and (b) fractography images of BD samples with transgranular striations and secondary micro-cracks along slip bands [117]. (Reproduced under the Creative Commons CC-BY license).

possible, unlike PBF-LB and DED-LB, where such comparisons have been established, resulting in a key barrier to qualifying CSAM IN718 for aerospace-critical cyclic loading and for applications requiring airworthiness certification.

Bagherifard *et al.* [152] report the only fatigue strength study on CSAM IN718 to date. Freestanding CSAM deposits have been subjected to two different annealing heat treatments: HTA at 1050 °C for 3 h and HTB at 1200 °C for 1 h. These are compared with PBF-LB (referred to as SLM in that study) coupons treated via the HTB route and a traditional SA heating cycle, labelled as HTC. The fatigue-limit plot (Fig. 38 **(a)**) shows CS-HTA reaching 363 ± 35 MPa, CS-HTB 435 ± 26 MPa, PBF-LB-HTB 481 ± 9 MPa, and PBF-LB-HTC 373 ± 62 MPa, values derived with ISO 12107 at 2 million cycles and benchmarked against bulk data of 275 MPa. Fractography of CS-HTA and HTB samples (Fig. 38 **(b)**) indicates mixed inter-splat decohesion and ductile dimples in CSAM, with a larger dimple fraction after HTB. Since these CSAM heat treatments are annealing-based, aimed at inter-particle bonding and stress relief, the conventional IN718 solutionizing-plus-aging sequence or HST-2h is not assessed, and there is no fatigue strength dataset for CSAM IN718 to benchmark against wrought samples.

Fig. 39 summarizes the cyclic property benchmarking discussed in this section. In Fig. 39 **(a)**, the post-processed PBF-LB and DED-LB

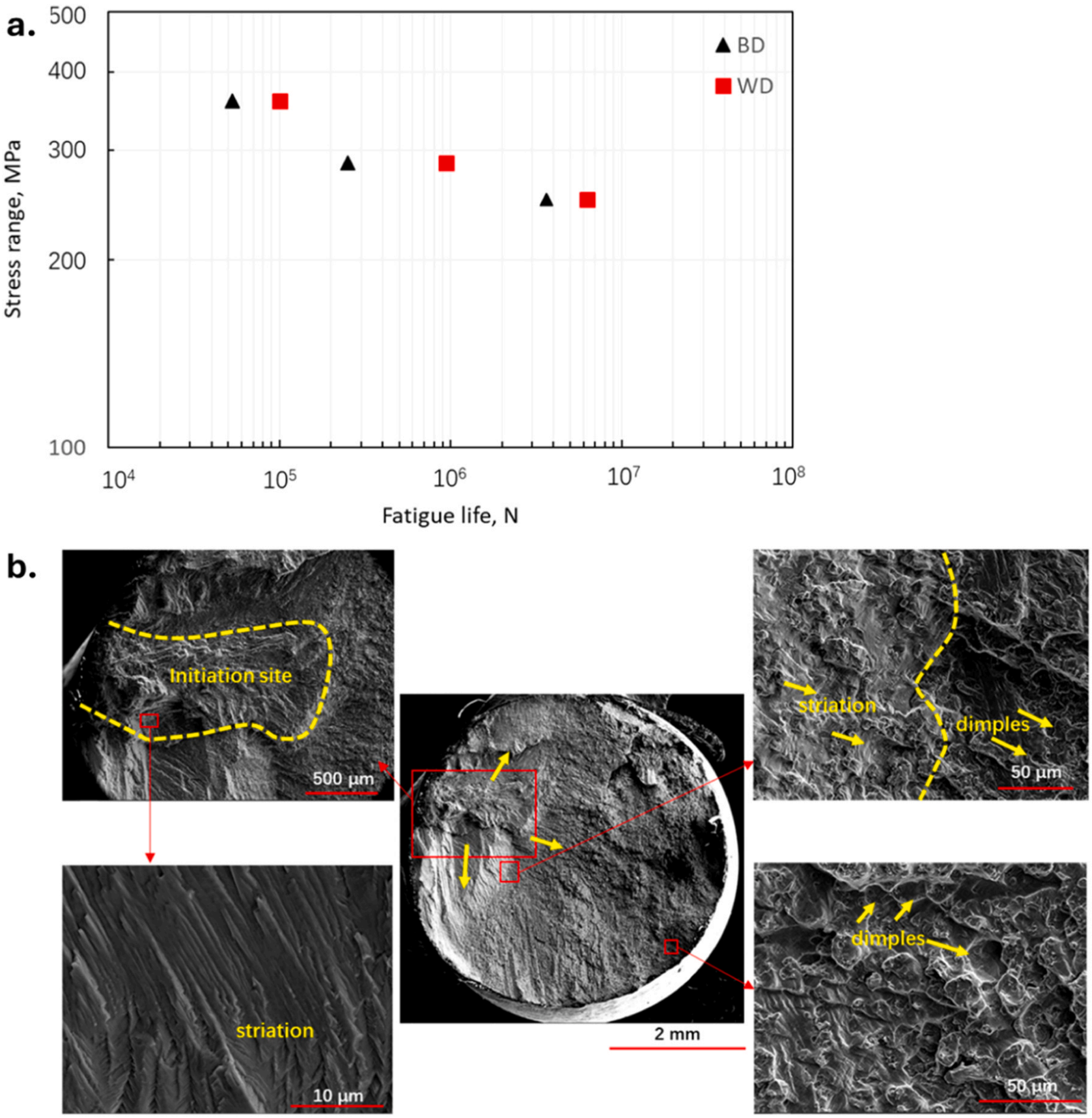

Fig. 36. (a) S-N curve for samples along the build direction (BD) and wall direction (WD), (b) fracture surface of BD samples showing surface crack initiation, striation-controlled propagation, and a ductile final zone with dimples [117]. (Reproduced under the Creative Commons CC-BY license).

datasets, particularly the HSA conditions, lie close to the wrought reference trend over the overlapping ΔK range. Comparable post-heat-treatment FCGR datasets are not yet available for WAAM, and free-standing CSAM IN718 FCGR data remain unreported. Fig. 39 **(b)** compiles the available high-cycle fatigue strength datasets by converting the reported stress amplitudes from their original stress ratios to a common fully reversed equivalent stress amplitude ($R = -1$) using the Goodman relation, based on the reported stress ratio, stress amplitude, and UTS [153,154]. The HA-treated PBF-LB dataset falls close to the wrought reference, whereas the HSA-treated DED-LB data remain lower over the stress range. High-cycle S-N curves for heat-treated WAAM and for CSAM are still unavailable.

5. Conclusions and future directions

This review compares fusion-based AM routes (PBF-LB, DED-LB, WAAM) with solid-state CSAM for IN718, linking processing to microstructure and mechanical properties. In fusion-based AM, the melted powders or wires solidify into columnar grains with dendritic, segregated microstructures with Laves phase, while CSAM bonds powder in the solid state and retains a deformed, powder-derived substructure. These fundamental differences explain the need for different post-heat treatment across AM processes.

PBF-LB requires an initial homogenization to dissolve Laves and recrystallize the matrix, followed by subsequent solutionizing and aging to precipitate γ'/γ'' uniformly with limited δ near the grain boundaries. After heat treatment, tensile strength and ductility surpass the wrought/cast counterparts. Collectively, the reported studies show PBF-LB can meet wrought standards in mechanical properties as well as fatigue behavior with appropriate post-heat treatment and surface finishing. However, build-orientation effects can persist in fatigue strength because the as-built surface condition changes with orientation, and in the near-threshold fatigue crack growth regime, where crack path roughness, crack closure, and defect alignment remain influential. HIP reduces this anisotropy by closing lack-of-fusion pores and weakening orientation-sensitive crack path guidance.

DED-LB forms coarser columnar grains and interdendritic Laves. Homogenization, followed by solutionizing plus aging, removes Laves,

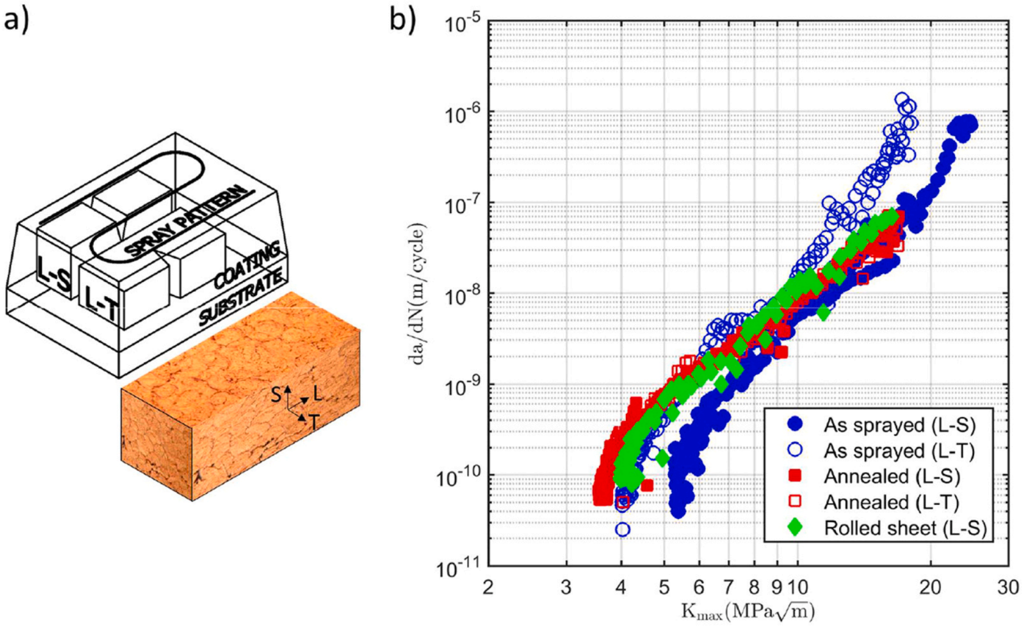

Fig. 37. a) Specimen orientation definition for crack growth in CSAM 316 L deposit using the L, T, and S directions, b) FCGR for as-built and annealed CSAM 316 L tested in the L-S and L-T orientations at R ∼ −1, compared with a cold-rolled 316 L sheet reference [150]. (Reproduced under the Creative Commons CC-BY-NC-ND).

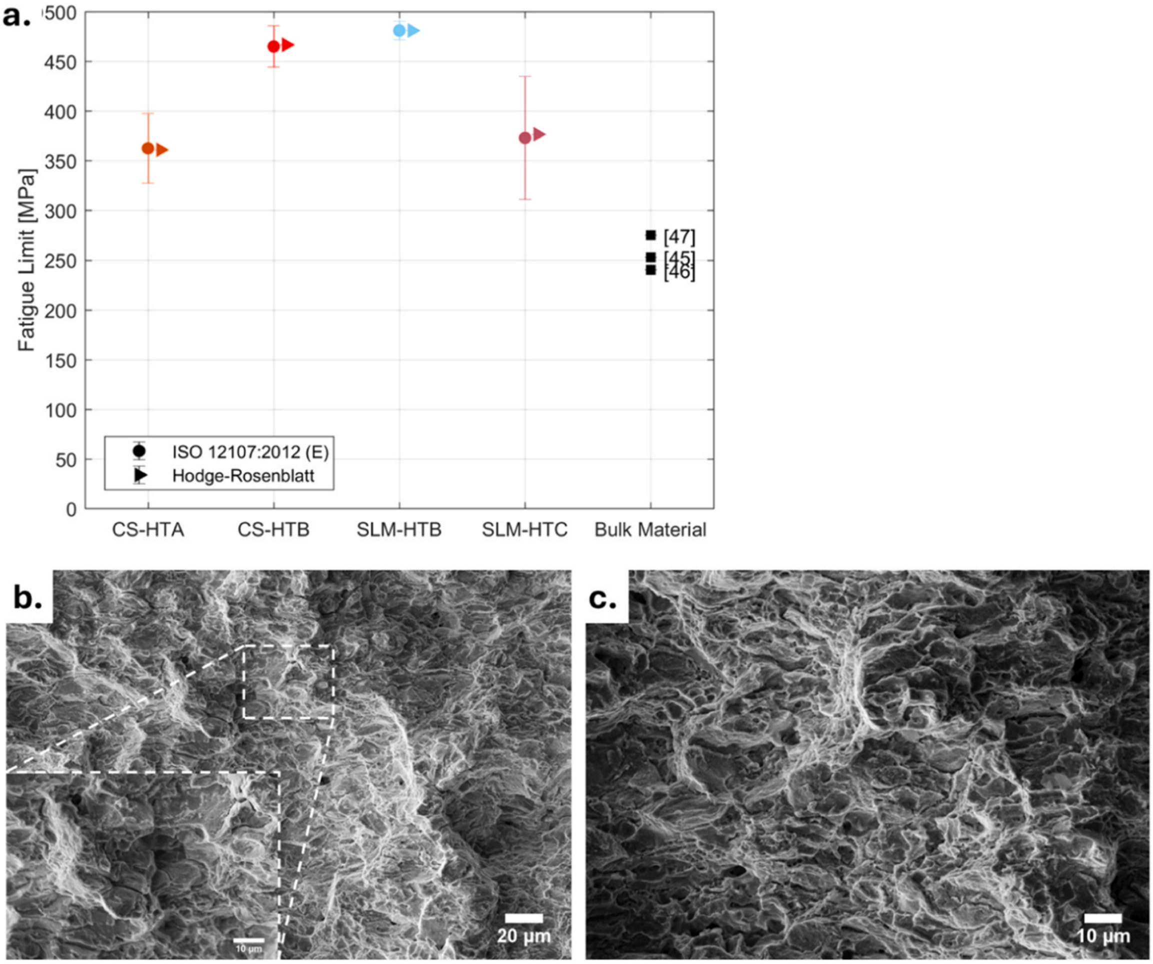

Fig. 38. (a) Fatigue limit of CSAM IN718 after HTA (1050 °C × 3 h) and HTB (1200 °C × 1 h), PBF-LB subject to HTB and HTC (SA-treated); fractography of (b) CS-HTA and (c) CS-HTB samples showing dimples [152]. (Reproduced with permission from Elsevier).

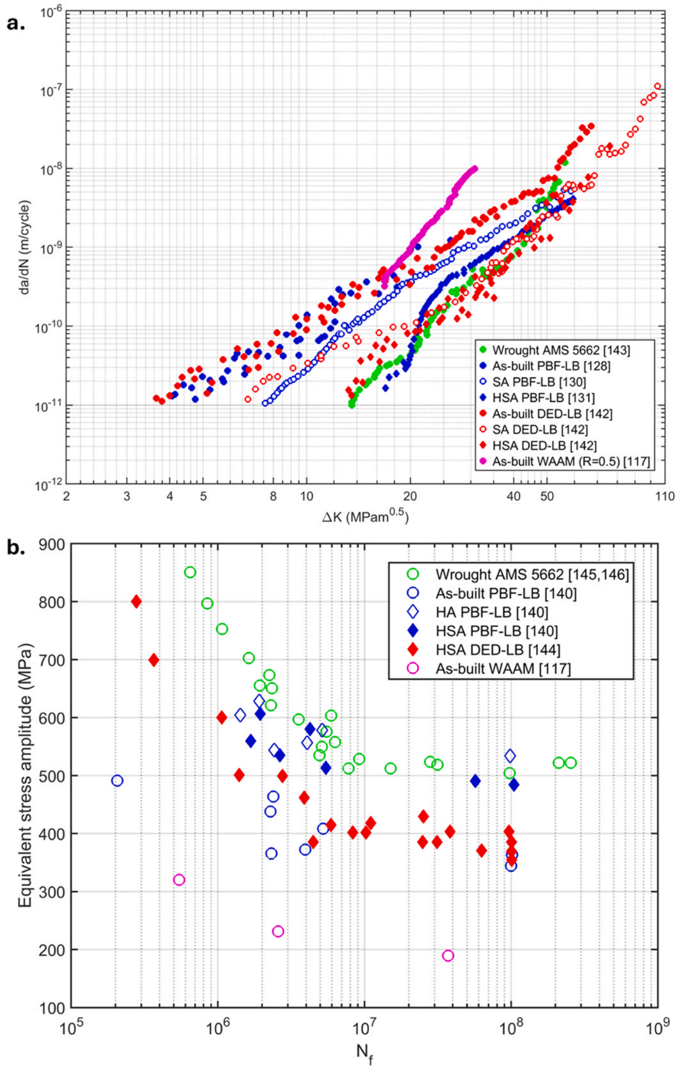

Fig. 39. Compilation of cyclic performance data of additively manufactured IN718: (a) FCGR curves, reported at $R = 0.1$ except for the WAAM dataset, and (b) Goodman-equivalent fully reversed stress amplitude ($R = -1$) plotted against number of cycles to failure (N_f).

randomizes texture, and yields uniform γ'/γ'', placing tensile properties within cast and wrought specifications. Also, the optimized post-heat treatment can raise fracture toughness to values exceeding wrought references. The fatigue strength remains below wrought limits even after heat treatment due to retained bimodal grain distribution and small pores acting as initiation sites, while threshold and crack growth rate match the wrought data band.

WAAM exhibits the coarsest, highly anisotropic microstructure with island-like Laves and millimeter-scale columnar grains. A modified high-temperature homogenization above the δ-solvus, followed by aging, dissolves Laves and suppresses δ, restoring ductility and meeting the cast standard, but it still lags the wrought specifications in tensile strength. Fatigue datasets are sparse and orientation-dependent for as-built samples, underscoring a need for systematic fatigue strength and crack growth studies after optimized heat treatments. Also, fracture resistance remains notch-orientation dependent even after homogenization-based heat treatment, because process-related discontinuities and local inhomogeneities can still provide preferential crack paths when unfavorably aligned.

CSAM deposits consist of work-hardened and imperfectly bonded deformed particles in the as-sprayed state, resulting in poor ductility. Therefore, heat treatment is mandatory. High-temperature solutionizing plus aging enhances metallurgical bonding across the interfaces, recrystallizes the matrix, and enables γ'/γ'' strengthening, resulting in static mechanical properties above the wrought/cast benchmarks. However, the effect of optimized heat treatment on anisotropy has not been systematically established for static properties and for fatigue and fracture behavior. Fatigue strength for CSAM IN718 has been reported only for post-treated annealed conditions, while datasets on fracture toughness and crack growth rate are not available for either as-built or heat-treated samples. In addition, there is limited research on surface post-processing for CSAM IN718 and on the associated residual-stress states, even though these variables are often decisive for fatigue strength and scatter.

Future work should standardize the post-processing heat treatment route for WAAM to achieve the wrought AMS 5662 standard. For CSAM and WAAM, there is an existing research gap in understanding the effect of recommended heat treatments on fatigue strength and crack growth behavior. For CSAM in particular, the combined influence of post-heat treatment and surface finishing on anisotropy, fatigue strength, and fracture resistance should be established to support reliable durability and damage-tolerance allowables. Addressing these will enable qualification pathways and wide industrial adoption of large WAAM structures, CSAM repairs/free-standing components.

CRediT authorship contribution statement

Abhinav Anand: Writing – original draft, Methodology, Investigation, Formal analysis, Conceptualization. **Ondřej Kovářík:** Writing – review & editing, Investigation. **Mario Guagliano:** Writing – review & editing, Supervision, Funding acquisition. **Jan Cizek:** Writing – review & editing, Supervision, Resources, Project administration, Funding acquisition.

Declaration of Competing Interest

The authors declare that they have no known competing financial interests or personal relationships that could have appeared to influence the work reported in this paper.

Acknowledgements

The authors would like to acknowledge Prof. Giuseppe Sala from Politecnico di Milano, Italy, for his feedback on this work. The PhD thesis of Abhinav Anand has been funded by the EU/Horizon/Doctoral Networks/Marie Skłodowska-Curie grant agreement No 101119988.

References

[1] D.V.V. Satyanarayana, N. Eswara Prasad, Nickel-Based Superalloys (Aerospace Materials), in: Eswara Prasad N., R.J.H. Wanhill (Eds.), Aerospace Materials and Material Technologies, 1, Springer Singapore, Singapore, 2017, pp. 199–228, https://doi.org/10.1007/978-981-10-2134-3_9 (Aerospace Materials).

[2] A.P. Mouritz, editor. 12 - Superalloys for gas turbine engines. Introduction to Aerospace Materials, Woodhead Publishing, 2012, pp. 251–267, https://doi.org/10.1533/9780857095152.251.

[3] K. Minet, A. Saharan, A. Loesser, N. Raitanen, 8 - Superalloys, powders, process monitoring in additive manufacturing, in: F. Froes, R. Boyer (Eds.), Additive Manufacturing for the Aerospace Industry, Elsevier, 2019, pp. 163–185, https://doi.org/10.1016/B978-0-12-814062-8.00009-1.

[4] S.R. Sabari, N.T.B.N. Koundinya, S.V.S.N. Murty, B.K. Nagesha, G.D. Janaki Ram, R.S. Kottada, Understanding the role of microstructure on creep anisotropy in additively manufactured IN718, Mater. Charact. 223 (2025) 114935, https://doi.org/10.1016/j.matchar.2025.114935.

[5] M. Bambach, I. Sizova, F. Silze, M. Schnick, Comparison of laser metal deposition of Inconel 718 from powder, hot and cold wire, Procedia CIRP 74 (2018) 206–209, https://doi.org/10.1016/j.procir.2018.08.095.

[6] R. Lawitzki, S. Hassan, L. Karge, J. Wagner, D. Wang, J. von Kobylinski, et al., Differentiation of γ'- and γ''- precipitates in Inconel 718 by a complementary study with small-angle neutron scattering and analytical microscopy, Acta Mater. 163 (2019) 28–39, https://doi.org/10.1016/j.actamat.2018.10.014.

[7] M.P. Haines, V.V. Rielli, S. Primig, N. Haghdadi, Powder bed fusion additive manufacturing of Ni-based superalloys: a review of the main microstructural

constituents and characterization techniques, J. Mater. Sci. 57 (2022) 14135–14187, https://doi.org/10.1007/s10853-022-07501-4.

[8] T. Kaleli Alay, M. Cagirici, M.Y. Yalcin, A. Yagmur, S. Tirkes, E. Aydogan, et al., Tailoring the microstructure and mechanical properties of IN718 alloy via a novel scanning strategy implemented in laser powder bed fusion, Materials Science Engineering A 884 (2023) 145543, https://doi.org/10.1016/j.msea.2023.145543.

[9] A.S. Wilson, Formation and effect of topologically close-packed phases in nickel-base superalloys, Mater. Sci. Technol. 33 (2017) 1108–1118, https://doi.org/10.1080/02670836.2016.1187335.

[10] Y. Li, J. Wu, M. Li, W. Xu, R. Ye, Z. Wang, Improved Inconel 718 superalloy repaired performance on 304 stainless steel shafts via recrystallization and Laves phase suppression in hybrid additive-subtractive manufacturing, J. Mater. Res. Technol. 37 (2025) 3289–3302, https://doi.org/10.1016/j.jmrt.2025.07.011.

[11] G.M. Volpato, U. Tetzlaff, M.C. Fredel, A comprehensive literature review on laser powder bed fusion of Inconel superalloys, Addit. Manuf. 55 (2022), https://doi.org/10.1016/j.addma.2022.102871.

[12] E. Sadeghi, P. Karimi, R. Esmaeilizadeh, F. Berto, S. Shao, J. Moverare, et al., A state-of-the-art review on fatigue performance of powder bed fusion-built alloy 718, Prog. Mater. Sci. 133 (2023) 101066, https://doi.org/10.1016/j.pmatsci.2022.101066.

[13] H.C. Pai, M. Sundararaman, A Comparison of the Precipitation Kinetics of γ'' Particles in Virgin and Re-Solutioned Alloy 625, Proc. Int. Symp Superalloys Var. Deriv. (2005) 487–495, https://doi.org/10.7449/2005/Superalloys_2005_487_495.

[14] G. Sjöberg, Casting Superalloys for Structural Applications, Superalloy 718 Deriv. (2010) 116–130, https://doi.org/10.1002/9781118495223.ch8.

[15] Weber J.H., Khalfalla Y., Benyounis K. Nickel-Based Superalloys: Alloying Methods and Thermomechanical Processing, 2016. https://doi.org/10.1016/B978-0-12-803581-8.03383-X.

[16] A. Lahbari, K. Bouchaala, H. Essoussi, M. Faqir, S. Ettaqi, E.H. Essadiqi, Homogenization heat treatment influence on microstructure evolution and mechanical properties of as-cast Al–Li–Cu–Mg–Zr alloy for lightweight aerospace application, Heliyon 10 (2024) e24426, https://doi.org/10.1016/j.heliyon.2024.e24426.

[17] J.W. Brooks, Forging of superalloys, Mater. Des. 21 (2000) 297–303, https://doi.org/10.1016/S0261-3069(99)00069-2.

[18] A.P. Mouritz, Processing and machining of aerospace metals. Introduction to Aerospace Materials, Woodhead Publishing, 2012, pp. 154–172. A.P.MouritzA.P.Mouritz10.1533/9780857095152.154.

[19] E. Hosseini, V.A. Popovich, A review of mechanical properties of additively manufactured Inconel 718, Addit. Manuf. 30 (2019) 100877, https://doi.org/10.1016/j.addma.2019.100877.

[20] Clare A.T., Woizeschke P., Rankouhi B., Pfefferkorn F.E., Bartels D., Schmidt M., et al. Metal multi-material additive manufacturing: Overcoming barriers to implementation. CIRP Annals 2025;74:869–893. https://doi.org/https://doi.org/10.1016/j.cirp.2025.05.004.

[21] S. Hasanov, S. Alkunte, M. Rajeshirke, A. Gupta, O. Huseynov, I. Fidan, et al., Review on Additive Manufacturing of Multi-Material Parts: Progress and Challenges, J. Manuf. Mater. Process. 6 (2022), https://doi.org/10.3390/jmmp6010004.

[22] A. Vafadar, F. Guzzomi, A. Rassau, K. Hayward, Advances in Metal Additive Manufacturing: A Review of Common Processes, Industrial Applications, and Current Challenges, Appl. Sci. 11 (2021), https://doi.org/10.3390/app11031213.

[23] B. Blakey-Milner, P. Gradl, G. Snedden, M. Brooks, J. Pitot, E. Lopez, et al., Metal additive manufacturing in aerospace: A review, Mater. Des. 209 (2021) 110008, https://doi.org/10.1016/j.matdes.2021.110008.

[24] O. Ibhadode, Z. Zhang, J. Sixt, K.M. Nsiempba, J. Orakwe, A. Martinez-Marchese, et al., Topology optimization for metal additive manufacturing: current trends, challenges, and future outlook, Virtual Phys. Prototyp. 18 (2023) e2181192, https://doi.org/10.1080/17452759.2023.2181192.

[25] A. du Plessis, N. Razavi, M. Benedetti, S. Murchio, M. Leary, M. Watson, et al., Properties and applications of additively manufactured metallic cellular materials: A review, Prog. Mater. Sci. 125 (2022) 100918, https://doi.org/10.1016/j.pmatsci.2021.100918.

[26] L. Cheng, J. Bai, A. To, Functionally graded lattice structure topology optimization for the design of additive manufactured components with stress constraints, Comput. Methods Appl. Mech. Eng. 344 (2018), https://doi.org/10.1016/j.cma.2018.10.010.

[27] A. Anand, D. Nagarajan, M. El Mansori, T. Sivarupan, Integration of Additive Fabrication with High-Pressure Die Casting for Quality Structural Castings of Aluminium Alloys; Optimising Energy Consumption, Trans. Indian Inst. Met. 76 (2023) 347–379, https://doi.org/10.1007/s12666-022-02750-y.

[28] S. Olhan, B. Antil, B.K. Behera, Progress in metal additive manufacturing using innovative solid-state friction stir-based techniques, J. Alloy. Compd. 1010 (2025) 177395, https://doi.org/10.1016/j.jallcom.2024.177395.

[29] N. K. N, P. B. N, R.P. T, A Comprehensive Review of Solid-phase Additive Techniques: Insights into Friction Stir Additive Manufacturing (FSAM) and Additive Friction Stir Deposition (AFSD), Results Eng. 27 (2025) 106604, https://doi.org/10.1016/j.rineng.2025.106604.

[30] S. Goel, E. Zaninelli, T. Gundgire, M. Ahlfors, O. Ojo, U. Klement, et al., Microstructure evolution and mechanical response-based shortening of thermal post-treatment for electron beam melting (EBM) produced Alloy 718, Materials Science Engineering A 820 (2021) 141515, https://doi.org/10.1016/j.msea.2021.141515.

[31] S. Goel, M. Ahlfors, F. Bahbou, S. Joshi, Effect of Different Post-treatments on the Microstructure of EBM-Built Alloy 718, J. Mater. Eng. Perform. 28 (2019) 673–680, https://doi.org/10.1007/s11665-018-3712-0.

[32] D. Deng, J. Moverare, R.L. Peng, H. Söderberg, Microstructure and anisotropic mechanical properties of EBM manufactured Inconel 718 and effects of post heat treatments, Materials Science Engineering A 693 (2017) 151–163, https://doi.org/10.1016/j.msea.2017.03.085.

[33] C.M. Sample, V.K. Champagne, A.T. Nardi, D.A. Lados, Factors governing static properties and fatigue, fatigue crack growth, and fracture mechanisms in cold spray alloys and coatings/repairs: A review, Addit. Manuf. 36 (2020) 101371, https://doi.org/10.1016/j.addma.2020.101371.

[34] P. Sudigdo, V.S. Bhattiprolu, T. Hussain, Cold Spray of Ni-Based Superalloys: A Review on Processing and Residual Stress, J. Therm. Spray. Technol. 34 (2025) 37–74, https://doi.org/10.1007/s11666-024-01916-y.

[35] M.A. Iqbal, K. Skotnicová, A. Shafiq, T.N. Sindhu, Inconel alloys: A comprehensive review of properties and advanced manufacturing techniques, Int. J. Thermofluids 29 (2025) 101394, https://doi.org/10.1016/j.ijft.2025.101394.

[36] M. Shahwaz, P. Nath, I. Sen, Recent advances in additive manufacturing technologies for Ni-Based Inconel superalloys – A comprehensive review, J. Alloy. Compd. 1010 (2025) 177654, https://doi.org/10.1016/j.jallcom.2024.177654.

[37] A.M.S.F. Corrosion, H.R.A. Committee, AMS5662 ALLOY BARS, FORGINGS, AND RINGS, CORROSION AND HEAT RESISTANT Nickel Base - 19Cr - 3.1Mo - 5.1(Cb + Ta) - 0.90Ti - 0.50Al Consumable Electrode or Vacuum Induction Melted, Solut. Treat. (1965), https://doi.org/10.4271/AMS5662.

[38] A.M.S.F. Corrosion, H.R.A. Committee, AMS5383 ALLOY CASTINGS, INVESTMENT, CORROSION AND HEAT RESISTANT Nickel Base - 19Cr - 3.0Mo - 5.1(Cb + Ta) - 0.90Ti - 0.60Al Vacuum Melted, Vac. Cast. (1966), https://doi.org/10.4271/AMS5383.

[39] M. Armstrong, H. Mehrabi, N. Naveed, An overview of modern metal additive manufacturing technology, J. Manuf. Process 84 (2022) 1001–1029, https://doi.org/10.1016/j.jmapro.2022.10.060.

[40] S. Chowdhury, N. Yadaiah, C. Prakash, S. Ramakrishna, S. Dixit, L.R. Gupta, et al., Laser powder bed fusion: a state-of-the-art review of the technology, materials, properties & defects, and numerical modelling, J. Mater. Res. Technol. 20 (2022) 2109–2172, https://doi.org/10.1016/j.jmrt.2022.07.121.

[41] N. Dejene, H. Lemu, Current Status and Challenges of Powder Bed Fusion-Based Metal Additive Manufacturing: Literature Review, Met. (Basel) 13 (2023), https://doi.org/10.3390/met13020424.

[42] J. Bartlett, X. Li, An overview of residual stresses in metal powder bed fusion, Addit. Manuf. 27 (2019) 131–149, https://doi.org/10.1016/j.addma.2019.02.020.

[43] G.M. Volpato, U. Tetzlaff, M.C. Fredel, A comprehensive literature review on laser powder bed fusion of Inconel superalloys, Addit. Manuf. 55 (2022) 102871, https://doi.org/10.1016/j.addma.2022.102871.

[44] H.T. Chowdhury, T.N. Palleda, N. Kakuta, K. Kakehi, Effects of Preheating on Thermal Behavior in Inconel 718 Processed by Additive Manufacturing, Thermo 4 (2024) 48–64, https://doi.org/10.3390/thermo4010005.

[45] A.R. McAndrew, M. Alvarez Rosales, P.A. Colegrove, J.R. Hönnige, A. Ho, R. Fayolle, et al., Interpass rolling of Ti-6Al-4V wire + arc additively manufactured features for microstructural refinement, Addit. Manuf. 21 (2018) 340–349, https://doi.org/10.1016/j.addma.2018.03.006.

[46] D. Svetlizky, M. Das, B. Zheng, A. Vyatskikh, S. Bose, A. Bandyopadhyay, et al., Directed Energy Deposition (DED) Additive Manufacturing: Physical Characteristics, Defects, Challenges and Applications, Mater. Today 49 (2021) 271–295, https://doi.org/10.1016/j.mattod.2021.03.020.

[47] T.R.F. Cavalcante, F.E. Mariani, J.A.A. Diaz, Additive manufacturing of Inconel 718: A review on microstructures and mechanical properties of DED-LB-processed samples, J. Mater. Res (2025), https://doi.org/10.1557/s43578-025-01663-y.

[48] N. Ghanadi, S. Pasebani, A Review on Wire-Laser Directed Energy Deposition: Parameter Control, Process Stability, and Future Research Paths, J. Manuf. Mater. Process. 8 (2024), https://doi.org/10.3390/jmmp8020084.

[49] M. Abuabiah, N.G. Mbodj, B. Shaqour, L. Herzallah, A. Juaidi, R. Abdallah, et al., Advancements in Laser Wire-Feed Metal Additive Manufacturing: A Brief Review, Materials 16 (2023), https://doi.org/10.3390/ma16052030.

[50] S. Yang, A. Speidel, A.T. Clare, C. Bennett, X. Jin, Residual stress prediction in machining of parts fabricated by directed energy deposition, Addit. Manuf. 104 (2025) 104765, https://doi.org/10.1016/j.addma.2025.104765.

[51] F. Mazzucato, D. Forni, A. Valente, E. Cadoni, Laser Metal Deposition of Inconel 718 Alloy and As-built Mechanical Properties Compared to Casting, Materials 14 (2021), https://doi.org/10.3390/ma14020437.

[52] J. Li, M.R. Alkahari, N. Rosli, R. Hasan, M.N. Sudin, F. Ramli, Review of Wire Arc Additive Manufacturing for 3D Metal Printing, Int. J. Autom. Technol. 13 (2019) 346–353, https://doi.org/10.20965/ijat.2019.p0346.

[53] S. Gain, D. Veeman, A review on advances and challenges in wire arc additive manufacturing: Process parameters, microstructural evolution and material performance across alloys, J. Alloy. Compd. 1029 (2025) 180735, https://doi.org/10.1016/j.jallcom.2025.180735.

[54] D. Jafari, T.H.J. Vaneker, I. Gibson, Wire and arc additive manufacturing: Opportunities and challenges to control the quality and accuracy of manufactured parts, Mater. Des. 202 (2021) 109471, https://doi.org/10.1016/j.matdes.2021.109471.

[55] S. Pattanayak, S.K. Sahoo, Gas metal arc welding based additive manufacturing—a review, CIRP J. Manuf. Sci. Technol. 33 (2021) 398–442, https://doi.org/10.1016/j.cirpj.2021.04.010.

[56] C.E. Seow, H.E. Coules, G. Wu, R.H.U. Khan, X. Xu, S. Williams, Wire + Arc Additively Manufactured Inconel 718: Effect of post-deposition heat treatments

on microstructure and tensile properties, Mater. Des. 183 (2019) 108157, https://doi.org/10.1016/j.matdes.2019.108157.

[57] Y. Zou, Cold Spray Additive Manufacturing: Microstructure Evolution and Bonding Features, Acc. Mater. Res 2 (2021) 1071–1081, https://doi.org/10.1021/accountsmr.1c00138.

[58] A. Kafle, S. Lu, R. Silwal, W. Zhu, A Review on Material Dynamics in Cold Spray Additive Manufacturing: Bonding, Stress, and Structural Evolution in Metals, Met. (Basel) 15 (2025), https://doi.org/10.3390/met15020187.

[59] W. Sun, X. Chu, H. Lan, R. Huang, J. Huang, Y. Xie, et al., Current Implementation Status of Cold Spray Technology: A Short Review, J. Therm. Spray. Technol. 31 (2022) 848–865, https://doi.org/10.1007/s11666-022-01382-4.

[60] W. Ma, X. Yingchun, C. Chen, H. Fukanuma, J. Wang, Z. Ren, et al., Microstructural and mechanical properties of high-performance Inconel 718 alloy by cold spraying, J. Alloy. Compd. 792 (2019), https://doi.org/10.1016/j.jallcom.2019.04.045.

[61] A.K. Kushwaha, M. Misra, P.L. Menezes, Smart manufacturing approach to manufacture bulk nanocrystalline aluminum for lightweight applications, Int. J. Adv. Manuf. Technol. 134 (2024) 5175–5190, https://doi.org/10.1007/s00170-024-14473-z.

[62] J. Schmitt, G. Mauer, R. Mücke, J. Fiebig, O. Guillon, R. Vaßen, Modeling and in-flight diagnostics of the IN718 cold spray process using different nozzle geometries, Surf. Coat. Technol. 514 (2025), https://doi.org/10.1016/j.surfcoat.2025.132547.

[63] D.H.L. Seng, Z. Zhang, Z.Q. Zhang, T.L. Meng, S.L. Teo, B.H. Tan, et al., Impact of spray angle and particle velocity in cold sprayed IN718 coatings, Surf. Coat. Technol. 466 (2023), https://doi.org/10.1016/j.surfcoat.2023.129623.

[64] W. Sun, A.W.Y. Tan, A. Bhowmik, I. Marinescu, X. Song, W. Zhai, et al., Deposition characteristics of cold sprayed Inconel 718 particles on Inconel 718 substrates with different surface conditions, Materials Science Engineering A 720 (2018) 75–84, https://doi.org/10.1016/j.msea.2018.02.059.

[65] X.T. Luo, M.L. Yao, N. Ma, M. Takahashi, C.J. Li, Deposition behavior, microstructure and mechanical properties of an in-situ micro-forging assisted cold spray enabled additively manufactured Inconel 718 alloy, Mater. Des. 155 (2018) 384–395, https://doi.org/10.1016/j.matdes.2018.06.024.

[66] M.A. Adaan-Nyiak, A.A. Tiamiyu, Recent advances on bonding mechanism in cold spray process: A review of single-particle impact methods, J. Mater. Res 38 (2023) 69–95, https://doi.org/10.1557/s43578-022-00764-2.

[67] A. Garfias, P. Kindermann, R.F. Vaz, V. Albaladejo-Fuentes, J. Sánchez, I. Ünsal, et al., Repair of Inconel 718 parts by Cold Spray Additive Manufacturing: The effect of substrate preheating on thick coatings properties, J. Alloy. Compd. 1010 (2025) 178182, https://doi.org/10.1016/j.jallcom.2024.178182.

[68] K. Wu, W. Sun, A.W.Y. Tan, S.C. Tan, E. Liu, W. Zhou, High temperature oxidation and oxychlorination behaviors of cold sprayed Inconel 718 deposits at 700 °C, Corros. Sci. 207 (2022), https://doi.org/10.1016/j.corsci.2022.110536.

[69] L.I. Pérez-Andrade, F. Gärtner, M. Villa-Vidaller, T. Klassen, J. Muñoz-Saldaña, J. M. Alvarado-Orozco, Optimization of Inconel 718 thick deposits by cold spray processing and annealing, Surf. Coat. Technol. 378 (2019) 124997, https://doi.org/10.1016/j.surfcoat.2019.124997.

[70] W. Ma, Y. Xie, C. Chen, H. Fukanuma, J. Wang, Z. Ren, et al., Microstructural and mechanical properties of high-performance Inconel 718 alloy by cold spraying, J. Alloy. Compd. 792 (2019) 456–467, https://doi.org/10.1016/j.jallcom.2019.04.045.

[71] Z. Zhang, D.H.L. Seng, M. Lin, S.L. Teo, T.L. Meng, C.J.J. Lee, et al., Cold spray deposition of Inconel 718 in comparison with atmospheric plasma spray deposition, Appl. Surf. Sci. 535 (2021) 147704, https://doi.org/10.1016/j.apsusc.2020.147704.

[72] R. Singh, K.-H. Rauwald, E. Wessel, G. Mauer, S. Schruefer, A. Barth, et al., Effects of substrate roughness and spray-angle on deposition behavior of cold-sprayed Inconel 718, Surf. Coat. Technol. 319 (2017) 249–259, https://doi.org/10.1016/j.surfcoat.2017.03.072.

[73] W. Sun, A. Bhowmik, A.W.-Y. Tan, R. Li, F. Xue, I. Marinescu, et al., Improving microstructural and mechanical characteristics of cold-sprayed Inconel 718 deposits via local induction heat treatment, J. Alloy. Compd. 797 (2019) 1268–1279, https://doi.org/10.1016/j.jallcom.2019.05.099.

[74] A. Bisht, B. Alwin, M. Anantharaman, M. Kamaraj, S.R. Bakshi, Development of IN718 Coating for Repair Applications by High-Pressure Cold Spraying Followed by Heat Treatment, J. Therm. Spray. Technol. 33 (2024) 2242–2261, https://doi.org/10.1007/s11666-024-01832-1.

[75] A. Balasundaram, A. Bisht, M. Anantharaman, S.R. Bakshi, M. Kamaraj, Effect of Double-Aging Heat Treatment on Microstructure and Tribological Behaviour of Cold Sprayed IN718 Coating, Met. Mater. Int. 30 (2024) 483–500, https://doi.org/10.1007/s12540-023-01507-6.

[76] M. Vadani, S. Raj, C. Mondal, W. Sun, S. Chakrabarty, S. Msolli, et al., Unveiling Relationship Between Crack Evolution Through Long-Term Ageing and Mechanical Properties of Cold-Sprayed Ni-Base Superalloys: Experimental Characterization and Evidence Through Finite Element Modeling, Adv. Eng. Mater. (2025), https://doi.org/10.1002/adem.202501848.

[77] S. Bagherifard, G. Roscioli, M. Zuccoli, M. Hadi, G. D'Elia, A.G. Demir, et al., Cold Spray Deposition of Freestanding Inconel Samples and Comparative Analysis with Selective Laser Melting, J. Therm. Spray. Technol. 26 (2017) 1–10, https://doi.org/10.1007/s11666-017-0572-3.

[78] S.Y. Kim, V. Luzin, M.L. Sesso, J. Thornton, S. Gulizia, The Effect of Low Temperature Range Heat Treatment on the Residual Stress of Cold Gas Dynamic Sprayed Inconel 718 Coatings via Neutron Diffraction, J. Therm. Spray. Technol. 29 (2020) 1477–1497, https://doi.org/10.1007/s11666-020-01080-z.

[79] A. Karakaş, A. Ataee, A. Rathi, T.O. Fenercioğlu, C. Erdogan, T. Yalçinkaya, Post heat treatment optimization of cold spray additive manufactured Inconel 718, Sci. Rep. 15 (2025), https://doi.org/10.1038/s41598-025-90723-8.

[80] H. Su, X. Luo, C. Li, Dense and fine grained IN718 superalloy additively manufactured by cold spraying with N2 gas at 10 MPa, Materials Science Engineering A 927 (2025), https://doi.org/10.1016/j.msea.2025.148017.

[81] W. Li, H. Wu, F. Huang, H. Liao, S. Deng, Revolutionizing Repair and Production: An Integrated Modular Cold Spray Additive Manufacturing System, J. Therm. Spray. Technol. 34 (2025) 531–549, https://doi.org/10.1007/s11666-025-01943-3.

[82] H. Afsharnia, J. Butt, Artificial Intelligence and Machine Learning in Cold Spray Additive Manufacturing: A Systematic Literature Review, J. Manuf. Mater. Process. 9 (2025), https://doi.org/10.3390/jmmp9100334.

[83] Steffen Donath, 3D Print. a Rocket Engine (2019). ⟨https://www.etmm-online.com/3d-printing-arocket-engine-a-886960/⟩.

[84] Carl Hauser, Scaling Addit. Manuf. (2025). ⟨https://www.twi-global.com/media-and-events/insights/scaling-up-additive-manufacturing⟩.

[85] I. Waugh, J. Kondas, R. Singh, M. Meinicke, L. Holzgaßner, Beyond Build. Vol. Cold Spray. Addit. Manuf. bimetallic Combust. Chamb. (2022).

[86] S. Ejiri, Multi-Material Axial-Flow Impeller with Inconel 718 Laminated on SST 304 by Wire Arc Additive Manufacturing †, Eng. Proc. 76 (2024) https://doi.org/10.3390/engproc2024076086.

[87] R.F. Vaz, A. Garfias, V. Albaladejo, J. Sanchez, I.G. Cano, A Review of Advances in Cold Spray Additive Manufacturing, Coatings 13 (2023), https://doi.org/10.3390/coatings13020267.

[88] Grand View Research, Cold Spray Technology Market Size, Share & Trends Analysis Report By Material (Nickel, Copper, Aluminum, Titanium), By Service (Cold Spray Additive Manufacturing), 2023 - 2030. By End-use, By Region, And Segment Forecasts, 2023, ⟨https://www.grandviewresearch.com/industry-analysis/cold-spray-technology-market-report⟩, 2023 - 2030.

[89] J.-C. Schmitt, F. Lang, J. Fiebig, T. Sievert, J. Gibmeier, O. Guillon, et al., Effect of Process Parameters on Residual Stresses of Cold Gas Sprayed IN718 Coatings on Large Repair Geometries, J. Therm. Spray. Technol. (2025), https://doi.org/10.1007/s11666-025-02011-6.

[90] S. Rott, A. Ladewig, K. Friedberger, J. Casper, M. Full, J.H. Schleifenbaum, Surface roughness in laser powder bed fusion – Interdependency of surface orientation and laser incidence, Addit. Manuf. 36 (2020) 101437, https://doi.org/10.1016/j.addma.2020.101437.

[91] E. Maleki, B. Salehnasab, M. Paul, S. Shao, N. Shamsaei, Dimensional accuracy of fabricated geometries through powder bed fusion: An overview and a new benchmark artifact proposal, Mater. Des. 257 (2025) 114361, https://doi.org/10.1016/j.matdes.2025.114361.

[92] S.C. Subedi, A. Shahba, M. Thevamaran, D.J. Thoma, K. Suresh, Towards the optimal design of support structures for laser powder bed fusion-based metal additive manufacturing via thermal equivalent static loads, Addit. Manuf. 57 (2022) 102956, https://doi.org/10.1016/j.addma.2022.102956.

[93] N. Khanna, H. Salvi, B. Karaş, I. Fairoz, A. Shokrani, Cost Modelling for Powder Bed Fusion and Directed Energy Deposition Additive Manufacturing, J. Manuf. Mater. Process. 8 (2024), https://doi.org/10.3390/jmmp8040142.

[94] L.J. Kumar, C.G.K. Nair, Laser metal deposition repair applications for Inconel 718 alloy, Mater. Today Proc. 4 (2017) 11068–11077, https://doi.org/10.1016/j.matpr.2017.08.068.

[95] D.R. Feenstra, R. Banerjee, H.L. Fraser, A. Huang, A. Molotnikov, N. Birbilis, Critical review of the state of the art in multi-material fabrication via directed energy deposition, Curr. Opin. Solid State Mater. Sci. 25 (2021) 100924, https://doi.org/10.1016/j.cossms.2021.100924.

[96] A. Queguineur, R. Asadi, M. Ostolaza, E.H. Valente, V.K. Nadimpalli, G. Mohanty, et al., Wire arc additive manufacturing of thin and thick walls made of duplex stainless steel, Int. J. Adv. Manuf. Technol. 127 (2023) 381–400, https://doi.org/10.1007/s00170-023-11560-5.

[97] F.N. Lomo, M.J. Patel, A. Vargas-Uscategui, P.C. King, I.S. Cole, A design and optimisation framework for cold spray additive manufacturing of lightweight aerospace structural components, Addit. Manuf. 78 (2023) 103891, https://doi.org/10.1016/j.addma.2023.103891.

[98] H. Wu, X. Xie, S. Liu, S. Xie, R. Huang, C. Verdy, et al., Bonding behavior of Bi-metal-deposits produced by hybrid cold spray additive manufacturing, J. Mater. Process Technol. 299 (2022) 117375, https://doi.org/10.1016/j.jmatprotec.2021.117375.

[99] D. Kumar, S. Palanisamy, K. Krishnan, M.M. Alam, Life Cycle Assessment of Cold Spray Additive Manufacturing and Conventional Machining of Aluminum Alloy Flange, Met. (Basel) 13 (2023), https://doi.org/10.3390/met13101684.

[100] D. Thomas, S. Gilbert, Costs Cost. Eff. Addit. Manuf. (2014), https://doi.org/10.6028/NIST.SP.1176.

[101] Y. Li, C. Su, J. Zhu, Comprehensive review of wire arc additive manufacturing: Hardware system, physical process, monitoring, property characterization, application and future prospects, Results Eng. 13 (2022) 100330, https://doi.org/10.1016/j.rineng.2021.100330.

[102] Godec, M. Mirzabeigi, N. Donik, D.A. Skobir Balantič, S. Malej, I. Paulin, et al., Influence of laser beam shape and post heat-treatment on the microstructure and mechanical properties of nickel-based alloy IN718 manufactured by laser powder bed fusion, J. Mater. Res. Technol. 37 (2025) 1970–1986, https://doi.org/10.1016/j.jmrt.2025.06.119.

[103] L. Emanuelli, F. Deirmina, M. Pellizzari, Heat treatment behaviour of IN718 superalloy fabricated by laser-powder bed fusion, Mater. Charact. 199 (2023) 112788, https://doi.org/10.1016/j.matchar.2023.112788.

[104] D. Zhang, W. Niu, X. Cao, Z. Liu, Effect of standard heat treatment on the microstructure and mechanical properties of selective laser melting manufactured Inconel 718 superalloy, Materials Science Engineering A 644 (2015) 32–40, https://doi.org/10.1016/j.msea.2015.06.021.

[105] E.M. Fayed, D. Shahriari, M. Saadati, V. Brailovski, M. Jahazi, M. Medraj, Influence of Homogenization and Solution Treatments Time on the Microstructure and Hardness of Inconel 718 Fabricated by Laser Powder Bed Fusion Process, Materials 13 (2020), https://doi.org/10.3390/ma13112574.

[106] M. Seifi, A.A. Salem, D.P. Satko, R. Grylls, J.J. Lewandowski, Effects of post-processing on microstructure and mechanical properties of SLM-processed IN-718 (- June), in: Minerals, Metals and Materials Series, 2018, Springer International Publishing, 2018, pp. 515–526, https://doi.org/10.1007/978-3-319-89480-5_33 (- June).

[107] M.M. Imran, A. Che Idris, L.C. De Silva, Y.-B. Kim, P.E. Abas, Advancements in 3D Printing: Directed Energy Deposition Techniques, Defect Analysis, and Quality Monitoring, Technol. (Basel) 12 (2024), https://doi.org/10.3390/technologies12060086.

[108] A. del Bosque, P. Fernández-Arias, D. Vergara, Advances in the Additive Manufacturing of Superalloys, J. Manuf. Mater. Process. 9 (2025), https://doi.org/10.3390/jmmp9070215.

[109] Ahmad N., Ghiaasiaan R., Gradl P., Shao S., Shamsaei N. Microstructure and Mechanical Properties of Additively Manufactured Haynes 282: A Comparative Analysis between L-PBF and LP-DED Technologies. 2023.

[110] X. Yu, X. Lin, F. Liu, L. Wang, Y. Tang, J. Li, et al., Influence of post-heat-treatment on the microstructure and fracture toughness properties of Inconel 718 fabricated with laser directed energy deposition additive manufacturing, Materials Science Engineering A 798 (2020), https://doi.org/10.1016/j.msea.2020.140092.

[111] J.E. Burke, The formation of annealing twins, JOM 2 (1950) 1324–1328, https://doi.org/10.1007/BF03399157.

[112] F. Zhou, X. Hu, Y. Zhou, Z. Xu, C. Guo, G. Li, et al., Effects of post-heat treatment on anisotropic mechanical properties of laser additively manufactured IN718, Materials Science Engineering A 877 (2023), https://doi.org/10.1016/j.msea.2023.145144.

[113] R.L. Tobler, Low temperature effects on the fracture behaviour of a nickel base superalloy, Cryog. (Guildf.) 16 (1976) 669–674, https://doi.org/10.1016/0011-2275(76)90039-4.

[114] H. Xiao, X. Liu, W. Xiao, J. Yang, C. Li, Y. Li, et al., Influence of molten-pool cooling rate on solidification structure and mechanical property of laser additive manufactured Inconel 718, J. Mater. Res. Technol. 19 (2022) 4404–4416, https://doi.org/10.1016/j.jmrt.2022.06.162.

[115] H. Hamdi, S. Sadatabhari, A. Tajik, A.Z. Hanzaki, A. Hatamiyan, H.R. Abedi, From melt pool to performance: A review of microstructural engineering in the additive manufacturing of nickel-based superalloys, Results Eng. 28 (2025) 107402, https://doi.org/10.1016/j.rineng.2025.107402.

[116] Z. Wu, P. O'Toole, C. Hagenlocher, M. Qian, M. Brandt, J. Watts, Melt pool dynamics on different substrate materials in high-speed laser directed energy deposition process, J. Laser Appl. 35 (2023) 042073, https://doi.org/10.2351/7.0001145.

[117] G. Wu, M. Yang, Z. Yu, S. Zhang, H. Liu, J. Xiong, Experimental Studies on the Anisotropic Fatigue Behaviour of IN718 Fabricated via Wire Arc Additive Manufacturing, Met. (Basel) 14 (2024), https://doi.org/10.3390/met14070770.

[118] G.H. Lee, B. Kim, J.B. Jeon, M. Park, S. Noh, B.J. Kim, Precipitate phase behavior and mechanical properties of Inconel 718 according to aging heat treatment time, Materials Science Engineering A 924 (2025) 147776, https://doi.org/10.1016/j.msea.2024.147776.

[119] C.E. Seow, J. Zhang, H.E. Coules, G. Wu, C. Jones, J. Ding, et al., Effect of crack-like defects on the fracture behaviour of Wire + Arc Additively Manufactured nickel-base Alloy 718, Addit. Manuf. 36 (2020), https://doi.org/10.1016/j.addma.2020.101578.

[120] D.H.L. Seng, Z. Zhang, Z.-Q. Zhang, T.L. Meng, S.L. Teo, B.H. Tan, et al., Impact of spray angle and particle velocity in cold sprayed IN718 coatings, Surf. Coat. Technol. 466 (2023) 129623, https://doi.org/10.1016/j.surfcoat.2023.129623.

[121] P. Poza, M.Á. Garrido-Maneiro, Cold-sprayed coatings: Microstructure, mechanical properties, and wear behaviour, Prog. Mater. Sci. 123 (2022) 100839, https://doi.org/10.1016/j.pmatsci.2021.100839.

[122] M. Shahana, M. Sadhasivam, K.G. Pradeep, S.R. Bakshi, M. Kamaraj, Strain induced microstructural changes in cold sprayed IN718 coating, Scr. Mater. 266 (2025), https://doi.org/10.1016/j.scriptamat.2025.116796.

[123] R. Ortiz-Fernandez, B. Jodoin, Toward Efficient Cold Spraying of Inconel 718: Understanding the Influence of Coating and Particle Impact Temperatures, J. Therm. Spray. Technol. 32 (2023) 188–207, https://doi.org/10.1007/s11666-022-01490-1.

[124] P. Sudigdo, D. Kóti, A. Ağır, C. Bennett, P. McNutt, T. Hussain, Understanding the bonding mechanism of cold sprayed additive manufacturing solution-treated Inconel 718 feedstock through microstructural characterisation, J. Mater. Res. Technol. 39 (2025) 9799–9818, https://doi.org/10.1016/j.jmrt.2025.12.011.

[125] S.E. Julien, A. Nourian-Avval, W. Liang, T. Schwartz, O.C. Ozdemir, S. Müftü, Bulk fracture anisotropy in Cold-Sprayed Al 6061 deposits, Eng. Fract. Mech. 263 (2022), https://doi.org/10.1016/j.engfracmech.2022.108301.

[126] O. Kovarik, J. Siegl, J. Cizek, T. Chraska, J. Kondas, Fracture Toughness of Cold Sprayed Pure Metals, J. Therm. Spray. Technol. 29 (2019) 147–157, https://doi.org/10.1007/s11666-019-00956-z.

[127] M. Prost, A. Köster, D. Missoum-Benziane, S. Dépinoy, L. Ferhat, M. Rambaudon, et al., Anisotropy in cyclic behavior and fatigue crack growth of IN718 processed by laser powder bed fusion, Addit. Manuf. 61 (2023) 103301, https://doi.org/10.1016/j.addma.2022.103301.

[128] R. Konečná, L. Kunz, G. Nicoletto, A. Bača, Long fatigue crack growth in Inconel 718 produced by selective laser melting, Int J. Fatigue 92 (2016) 499–506, https://doi.org/10.1016/j.ijfatigue.2016.03.012.

[129] H. Andersson, C. Persson, In-situ SEM study of fatigue crack growth behaviour in IN718, Int J. Fatigue 26 (2004) 211–219, https://doi.org/10.1016/S0142-1123(03)00172-5.

[130] H. Ostergaard, J. Pribe, M.T. Hasib, A. Paradowska, T. Siegmund, J. Kruzic, Near-threshold fatigue crack growth in laser powder bed fusion produced alloy 718, Int J. Fatigue 163 (2022) 107041, https://doi.org/10.1016/j.ijfatigue.2022.107041.

[131] K. Gruber, P. Szymczyk-Ziółkowska, S. Dziuba, S. Duda, P. Zielonka, S. Seitl, et al., Fatigue crack growth characterization of Inconel 718 after additive manufacturing by laser powder bed fusion and heat treatment, Int J. Fatigue 166 (2023), https://doi.org/10.1016/j.ijfatigue.2022.107287.

[132] F. Uriati, G. Nicoletto, A comparison of Inconel 718 obtained with three L-PBF production systems in terms of process parameters, as-built surface quality, and fatigue performance, Int J. Fatigue 162 (2022) 107004, https://doi.org/10.1016/j.ijfatigue.2022.107004.

[133] G. Nicoletto, Smooth and notch fatigue behavior of selectively laser melted Inconel 718 with as-built surfaces, Int J. Fatigue 128 (2019), https://doi.org/10.1016/j.ijfatigue.2019.105211.

[134] R. Konečná, G. Nicoletto, On the link between as-built surface quality and fatigue behavior of additively manufactured Inconel 718, in: Procedia Structural Integrity, 23, Elsevier B.V, 2019, pp. 384–389, https://doi.org/10.1016/j.prostr.2020.01.117.

[135] G. Macoretta, L. Romanelli, C. Santus, L. Romoli, A.H.A. Lutey, F. Uriati, et al., Modelling of the surface morphology and size effects on fatigue strength of L-PBF Inconel 718 by comparing different testing specimens, Int J. Fatigue 181 (2024), https://doi.org/10.1016/j.ijfatigue.2023.108120.

[136] L. Ednie, R.J. Lancaster, A.A. Antonysamy, F. Zelenka, A. Scarpellini, L. Parimi, et al., The effects of surface finish on the fatigue performance of electron beam melted Ti–6Al–4V, Materials Science Engineering A 857 (2022) 144050, https://doi.org/10.1016/j.msea.2022.144050.

[137] B. Blinn, S. Greco, M. Smaga, M. Zimmermann, H. Hotz, D. Müller, et al., Influence of microstructural defects and the surface topography on the fatigue behavior of "additively-subtractively" manufactured specimens made of AISI 316L, Materwiss Werksttech 52 (2021) 561–577, https://doi.org/10.1002/mawe.202000266.

[138] Idury K.S.N.S., Lu Y., Pavan A.H.V., Chakkravarthy V., Singh N.K., Sekar S., et al. Defect–Fatigue Correlations of Post-processed Laser Powder Bed Fused Metallic Alloys: A Review. Adv Eng Mater n.d.;n/a:e202501266. https://doi.org/https://doi.org/10.1002/adem.202501266.

[139] S. Park, Y. Tanaka, S. Okazaki, Y. Funakoshi, H. Kawashima, H. Matsunaga, Role of grain boundaries and precipitates in small, fatigue crack-growth resistance of additively-manufactured, Ni-based superalloy 718 under torsional cyclic loading (https://doi.org/), Mater. Lett. 350 (2023) 134844, https://doi.org/10.1016/j.matlet.2023.134844.

[140] H.Y. Wan, Z.J. Zhou, C.P. Li, G.F. Chen, G.P. Zhang, Enhancing Fatigue Strength of Selective Laser Melting-Fabricated Inconel 718 by Tailoring Heat Treatment Route, Adv. Eng. Mater. 20 (2018), https://doi.org/10.1002/adem.201800307.

[141] R.O. Ritchie, J.F. Knott, J.R. Rice, On the relationship between critical tensile stress and fracture toughness in mild steel (https://doi.org/), J. Mech. Phys. Solids 21 (1973) 395–410, https://doi.org/10.1016/0022-5096(73)90008-2.

[142] X. Yu, X. Lin, H. Tan, Y. Hu, S. Zhang, F. Liu, et al., Microstructure and fatigue crack growth behavior of Inconel 718 superalloy manufactured by laser directed energy deposition, Int J. Fatigue 143 (2021), https://doi.org/10.1016/j.ijfatigue.2020.106005.

[143] M. Clavel, A. Pineau, Fatigue Behaviour of Two Nickel-base Alloys I: Experimental Results on Low Cycle Fatigue, Fatigue Crack Propagation and Substructures 55 (1982).

[144] X. Yu, X. Lin, Z. Wang, S. Zhang, X. Gao, Y. Zhang, et al., Room and high temperature high-cycle fatigue properties of Inconel 718 superalloy prepared using laser directed energy deposition, Materials Science Engineering A 825 (2021), https://doi.org/10.1016/j.msea.2021.141865.

[145] Kawagoishi, Chen, Nisitani, Fatigue strength of Inconel 718 at elevated temperatures, Fatigue Fract. Eng. Mater. Struct. 23 (2000) 209–216, https://doi.org/10.1046/j.1460-2695.2000.00263.x.

[146] X. Ma, Z. Duan, H. Shi, R. Murai, E. Yanagisawa, Fatigue and fracture behavior of nickel-based superalloy Inconel 718 up to the very high cycle regime, J. Zhejiang Univ. -Sci. A 11 (2010) 727–737, https://doi.org/10.1631/jzus.A1000171.

[147] C.M. Sample, A.G. Spangenberger, V.K. Champagne, D.A. Lados, Mechanical properties and growth mechanisms of long and small fatigue cracks in as-deposited bulk cold spray Al-6061, Int J. Fatigue 181 (2024), https://doi.org/10.1016/j.ijfatigue.2024.108152.

[148] A. Anand, O. Kovářík, P. Ctibor, Z. Arabgol, L. Wiehler, F. Gärtner, et al., Cold spray additively manufactured pure iron for magnetic applications, Addit. Manuf. Lett. 17 (2026), https://doi.org/10.1016/j.addlet.2026.100363.

[149] J. Cizek, O. Kovarik, J. Cupera, J. Kondas, T. Bajer, F. Siska, et al., Measurement of mechanical and fatigue properties using unified, simple-geometry specimens: Cold spray additively manufactured pure metals, Surf. Coat. Technol. 412 (2021) 126929, https://doi.org/10.1016/j.surfcoat.2021.126929.

[150] S. Bagherifard, J. Kondas, S. Monti, J. Cizek, F. Perego, O. Kovarik, et al., Tailoring cold spray additive manufacturing of steel 316 L for static and cyclic load-bearing applications, Mater. Des. 203 (2021), https://doi.org/10.1016/j.matdes.2021.109575.

[151] S. Bagherifard, M. Guagliano, Fatigue performance of cold spray deposits: Coating, repair and additive manufacturing cases, Int J. Fatigue 139 (2020), https://doi.org/10.1016/j.ijfatigue.2020.105744.

[152] S. Bagherifard, S. Monti, M.V. Zuccoli, M. Riccio, J. Kondás, M. Guagliano, Cold spray deposition for additive manufacturing of freeform structural components compared to selective laser melting, Materials Science Engineering A 721 (2018) 339–350, https://doi.org/10.1016/j.msea.2018.02.094.

[153] M.H. Aliabadi, in: Bannantine Julie A., Comer Jess J., Handrock James L. (Eds.), Fundamentals of metal fatigue analysis, 1992, Prentice Hall Publishers, 1990, p. 273.

[154] S.-Y. Park, J. Lee, J.-T. Heo, G.B. Lee, H.H. Kim, B.-H. Choi, Assessment of Fatigue Lifetime and Characterization of Fatigue Crack Behavior of Aluminium Scroll Compressor Using C-Specimen, Appl. Sci. 10 (2020), https://doi.org/10.3390/app10093226.